

NAVAL POSTGRADUATE SCHOOL Monterey, California



THESIS

A CASE STUDY OF HIGH WINDS INDUCED BY
UPPER-LEVEL FRONTOGENESIS AND
TROPOPAUSE FOLDING

by

Sara T. Burke

March, 1997

Thesis Advisor:

Patricia M. Pauley

Approved for public release; distribution is unlimited.

DUDLEY KNOX LIBRARY
NAVAL POSTGRADUATE SCHOOL
MONTEREY CA 93943-5101

DUDLEY KNOX LIBRARY
NAVAL POSTGRADUATE SCHOOL
MONTEREY, CA 93943-5101

REPORT DOCUMENTATION PAGE

Form Approved OMB No. 0704-0188

Public reporting burden for this collection of information is estimated to average 1 hour per response, including the time for reviewing instruction, searching existing data sources, gathering and maintaining the data needed, and completing and reviewing the collection of information. Send comments regarding this burden estimate or any other aspect of this collection of information, including suggestions for reducing this burden, to Washington Headquarters Services, Directorate for Information Operations and Reports, 1215 Jefferson Davis Highway, Suite 1204, Arlington, VA 22202-4302, and to the Office of Management and Budget, Paperwork Reduction Project (0704-0188) Washington DC 20503.

1. AGENCY USE ONLY (Leave blank)	2. REPORT DATE March 1997.	3. REPORT TYPE AND DATES COVERED Master's Thesis	
4. TITLE AND SUBTITLE A CASE STUDY OF HIGH WINDS INDUCED BY UPPER-LEVEL FRONTOGENESIS AND TROPOPAUSE FOLDING		5. FUNDING NUMBERS	
6. AUTHOR Burke, Sara T.			
7. PERFORMING ORGANIZATION NAME(S) AND ADDRESS(ES) Naval Postgraduate School Monterey CA 93943-5000		8. PERFORMING ORGANIZATION REPORT NUMBER	
9. SPONSORING/MONITORING AGENCY NAME(S) AND ADDRESS(ES)		10. SPONSORING/MONITORING AGENCY REPORT NUMBER	
11. SUPPLEMENTARY NOTES The views expressed in this thesis are those of the author and do not reflect the official policy or position of the Department of Defense or the U.S. Government.			
12a. DISTRIBUTION/AVAILABILITY STATEMENT Approved for public release; distribution is unlimited.		12b. DISTRIBUTION CODE	
13. ABSTRACT (maximum 200 words) High surface winds over California and the bordering Pacific Ocean resulted in the death of one man and the loss of power to approximately 50,000 residences across the state. These damaging winds are hypothesized to result from an upper-level front and associated tropopause folding that rapidly intensify as they move south across the region, causing high-momentum air to be transported to the lower troposphere. Once the high-momentum air reaches the top of the planetary boundary layer, the combined effects of destabilization of the planetary boundary layer by cold air advection aloft and shear-induced turbulence at the top of the layer provide the initial mechanism by which the high-momentum air is entrained into the layer and mixed to the surface. After sunrise, convectively-driven turbulence provides an additional source of mixing in the planetary boundary layer. The high surface winds have a strong cross-isobaric component in the direction of the upper-level winds, and the upper-level frontal movement to the south over central California is synchronous with the increase of surface winds over the same region. The winds decrease as the upper-level front moves into the base of the upper-level trough and the high-momentum source in the lower-troposphere disappears.			
14. SUBJECT TERMS upper-level frontogenesis, tropopause folding, jet-streak, cold air advection, shear, convection, planetary boundary layer		15. NUMBER OF PAGES 114	
		16. PRICE CODE	
17. SECURITY CLASSIFICATION OF REPORT Unclassified	18. SECURITY CLASSIFICATION OF THIS PAGE Unclassified	19. SECURITY CLASSIFICATION OF ABSTRACT Unclassified	20. LIMITATION OF ABSTRACT UL

NSN 7540-01-280-5500

Standard Form 298 (Rev. 2-89)

Prescribed by ANSI Std. Z39-18 298-102

Approved for public release; distribution is unlimited.

**A CASE STUDY OF HIGH WINDS INDUCED BY UPPER-LEVEL
FRONTOGENESIS AND TROPOPAUSE FOLDING**

Sara T. Burke
Lieutenant, United States Navy
B.S., United States Naval Academy, 1990

Submitted in partial fulfillment
of the requirements for the degree of

**MASTER OF SCIENCE IN METEOROLOGY AND PHYSICAL
OCEANOGRAPHY**

from the

**NAVAL POSTGRADUATE SCHOOL
March 1997**

NPS Archive

1997.03

Burke, S.

~~1/10/15~~

~~0893615~~

~~C.7~~

ABSTRACT

High surface winds over California and the bordering Pacific Ocean resulted in the death of one man and the loss of power to approximately 50,000 residences across the state. These damaging winds are hypothesized to result from an upper-level front and associated tropopause folding that rapidly intensify as they move south across the region, causing high-momentum air to be transported to the lower troposphere. Once the high-momentum air reaches the top of the planetary boundary layer, the combined effects of destabilization of the planetary boundary layer by cold air advection aloft and shear-induced turbulence at the top of the layer provide the initial mechanism by which the high-momentum air is entrained into the layer and mixed to the surface. After sunrise, convectively-driven turbulence provides an additional source of mixing in the planetary boundary layer.

The winds have a strong cross-isobaric component in the direction of the upper-level winds, and the upper-level frontal movement to the south over central California is synchronous with the increase of surface winds over the same region. The winds decrease as the upper-level front moves into the base of the upper-level trough and the high-momentum source in the lower-troposphere disappears.

TABLE OF CONTENTS

I. INTRODUCTION	1
II. BACKGROUND	3
A. UPPER-LEVEL FRONTS	3
B. BOUNDARY LAYER PROCESSES	7
C. SEA-LEVEL PRESSURE REDUCTION	9
III. DATA AND METHODOLOGY	15
A. DATA	15
B. METHODOLOGY	17
IV. RESULTS	19
A. UPPER-LEVEL SYNOPTIC SITUATION	19
B. SURFACE ANALYSES	30
V. SUMMARY	39
APPENDIX. FIGURES	41
LIST OF REFERENCES	99

INITIAL DISTRIBUTION LIST	103
---------------------------------	-----

ACKNOWLEDGMENT

The author thanks Dr. Edward H. Barker, NRL-Monterey for providing the NORAPS analyses and skew-T code; Mr. Steve Finley, Colorado State University, and Mr. Bryan C. Hahn, Regional Weather Information Center, University of North Dakota, for providing the coded SA's; Mr. Larry Riddle, Climate Research Division, Scripps Institute of Oceanography, University of California, for providing the RAOBs; Mr. David Moellenberndt, California Department of Water Resources, for providing the CIMIS data; Mr. Avi Okin, Bay Area Air Quality Management District, for providing the Bay Area Meteorological Network Data; and LCDR John Powell, USN, for providing the SA decoding program (BUMPS). The author also thanks Prof. Patricia M. Pauley for her support and guidance, and for making the experience fun.

I. INTRODUCTION

On 14 November 1993, the sailing vessel Griffin departed Half Moon Bay, California and headed for San Diego, but “Mother Nature” prevented the vessel from reaching its final destination. High winds in the region whipped the ocean surface resulting in dangerously high seas that the Griffin could not withstand. The vessel began taking on water and to make matters even worse, the engine stalled. Two United States Navy ships, the USS Cimarron and USS Flint, answered the distress call but in the rough water the sailboat was hurled against one of the ships so hard that its mast broke and three of the five people on board were thrown overboard (Jones 1993). A Zodiac raft from the USS Cimarron rescued two of the victims, and the USS Flint sent a swimmer to try to help the third, an unconscious man. A Coast Guard helicopter arrived to airlift the victims to the Monterey Peninsula Airport and while in flight, the third man was declared dead. The Coast Guard received six pleas for help in a three hour period that day.

The high winds that caused this tragedy are hypothesized to be the result of a strong upper-level front and associated strong downward motion in the upper troposphere that transferred high-momentum air from upper-levels to the lower troposphere where it was then mixed to the surface by both convective and shear-driven turbulence in the boundary layer. The objective of this thesis is to document the high wind event and provide observational support for the hypothesized mechanisms that produced these winds. A previous case study of a November 1991 dust storm (Pauley et al. 1996) provided the initial analysis of a meteorological event of this type. This thesis will add support to the proposed hypothesis

and be added to a set of these high wind cases for future evaluation of the NORAPS (Navy Operational Regional Atmospheric Prediction System) mesoscale data assimilation system.

Chapter II provides background meteorological knowledge on upper-level fronts and the boundary layer processes that play a role in this event, as well as a review of sea-level pressure reduction techniques. Chapter III explains the sources and types of data used to document the high winds and also presents the methodology used to produce the analyses. The results are given in Chapter IV and the case is summarized in Chapter V.

II. BACKGROUND

A. UPPER-LEVEL FRONTS

A front is a thin zone (50-200 km wide) of convergence in the atmosphere in which the horizontal gradient of temperature, the absolute vorticity, the vertical wind shear, and the static stability are increased greatly beyond the original background values (Keyser and Shapiro 1986). Since the 1930's, when the introduction of upper-air soundings by radiosonde made data collection in the upper atmosphere practical, meteorologists have known that fronts slope upward from the earth's surface into the upper levels of the troposphere and lower stratosphere. In 1953 Reed and Sanders published the first paper that postulated that it was not correct to apply one frontal model to all systems, but that many surface or low-level fronts are characterized by features that extend no higher than 3 km, while other upper-tropospheric or upper-level fronts have no surface reflection at all (Carlson 1991).

Upper-level fronts are different from those at the surface not only in location, but also in structure. Reed and Danielsen (1959) directly related upper-level frontogenesis and jet streak formation to stratospheric-tropospheric exchange, or tropopause folding, by analyzing potential vorticity. In frictionless, adiabatic flow potential vorticity is conserved, thus potential temperature can be used to identify stratospheric air based on the definition of potential vorticity as

$$P_{\theta} = - \left(\frac{\partial \theta}{\partial p} \right) (\zeta_{\theta} + f) \quad (1)$$

in isentropic coordinates. θ represents potential temperature, p is the pressure, ζ_θ is the relative vorticity on a theta surface, and f is the Coriolis parameter (Carlson 1991). Stratospheric values of potential vorticity are one to three orders of magnitude greater than the tropospheric values because of the high static stability in the stratosphere associated with the combined effects of diabatic heating from ozone in the stratosphere and long-wave radiational cooling in the troposphere (Carlson 1991). The highest values of potential vorticity are observed close to the tropopause above the jet axis.

Mass transport across the tropopause as a result of tropopause folding is most commonly observed in the broad area of descent downstream from an upper-level ridge and, more specifically, it is focused in a region in which very strong upper-level frontogenesis is combined with an intense jet stream maximum (Carlson 1991). The downward vertical motion that produces the frontogenetical tilting also provides the mechanism by which stratospheric air is transported into the troposphere. This stratospheric air delineates the warm side of the frontal zone. Enhanced baroclinicity in the winter and spring cause the most pronounced episodes of tropopause folding, bringing stratospheric air with low water vapor content and high values of ozone, potential vorticity, static stability, and radioactive materials into the middle and lower troposphere (Carlson 1991). Thus, observational evidence indicates that upper-level fronts divide tropospheric and stratospheric air masses as opposed to separating tropical and polar air masses as surface fronts do (Keyser and Shapiro 1986).

Upper-level fronts and jet streaks are associated with transverse ageostrophic motions, which themselves are forced by the advection of temperature and momentum

through regions of confluence and shear in the upper-troposphere and lower stratosphere (Carlson 1991). As the jet stream propagates over the top of a long-wave ridge it moves from a region of pure confluence into an area of northwesterly flow in which the combined effects of confluence and shear are extremely conducive to the development of jet streaks. The addition of shear implies cold air advection which displaces the direct circulation cell of the jet streak entrance region to the warm side so that the downward vertical motion is enhanced directly below the jet axis and to the poleward side. The indirect cell in the exit region is skewed toward the cold side of the jet, also adding to the downward motion beneath the jet streak axis. Figure 1(a) is a depiction of the four-quadrant model of a jet streak, and in Fig. 1(b-d) the effects of confluence and shear are added to the four-quadrant model. Figure 2 is a cross section perpendicular to the jet streak in the entrance region for the combined confluence and shear with cold advection scenario (Fig. 1c) which illustrates the downward motion below the jet axis (Carlson 1991).

The initial development of the upper-level front is theorized to result from the differential vertical motion across the jet streak axis which produces the tilting necessary to rotate the vertical gradient of potential temperature into the horizontal plane, thus forming the frontal zone (Keyser and Shapiro 1986). The tilting term is also responsible for the generation of cyclonic vorticity which in turn increases the horizontal shear and the ageostrophic circulation, ultimately reinforcing the subsidence under the jet axis in a positive feedback loop. As the system propagates past the base of the long-wave trough the tilting term becomes frontolytical, but the effects of horizontal confluence are added to the system. The front therefore may continue to strengthen, such that it reaches its maximum intensity

after it moves through the base of the long-wave trough into the southwesterly flow. Figure 3(a-d) is a time series of the propagation of an upper-level frontal system through a midlatitude long-wave trough (Keyser and Shapiro 1986).

The regions above and below upper-tropospheric fronts and jet streaks are characterized by strong vertical wind shear and are prime locations for clear air turbulence (CAT). The Richardson number,

$$Ri = \frac{\frac{g}{\bar{\theta}_v} \frac{\partial \bar{\theta}_v}{\partial z}}{\left[\left(\frac{\partial \bar{U}}{\partial z} \right)^2 + \left(\frac{\partial \bar{V}}{\partial z} \right)^2 \right]} \quad (2)$$

is a ratio of the buoyant production/consumption of turbulent kinetic energy to the mechanical production. $\bar{\theta}_v$ is the mean virtual potential temperature, g is the acceleration due to gravity, z is the height relative to the horizontal surface at local sea-level, \bar{U} is the east-west component of the mean wind, and \bar{V} is the north-south component of the mean wind. The Richardson number provides an indication of the dynamic instability of the flow such that laminar flow is expected to become turbulent when Ri is small (< 0.25) and turbulent flow becomes laminar when Ri is large (> 1.0). The value of 0.25 is derived from estimated values of the local temperature gradient and wind shear (Stull 1988). Figure 4 is an illustration of an upper-level front with associated regions of turbulence (Keyser and Shapiro 1986). The strongest downward flux of potential temperature occurs in areas of CAT, thus there is a region of warming above the jet axis and cooling below.

Shapiro (1976) conducted three case studies of upper-level fronts and noted that a maximum in the values of isentropic potential vorticity existed in each case at the top of the frontal zone, specifically in the cyclonic wind shear zone at the level of the jet. This non-conservation of potential vorticity is attributed to a change in the vertical distribution of diabatic heating as a result of mixing of potential temperature in regions of clear-air turbulence. Potential vorticity remains a valid method for tracing the location of stratospheric air, despite the mesoscale high center in values, because of the initially large difference between the stratospheric and tropospheric values (Shapiro 1976). The creation of potential vorticity facilitates mass exchange between tropospheric and stratospheric air masses (Keyser and Shapiro 1986) and this process may be a means of strengthening upper-level frontal zones (Carlson 1991).

Upper-level fronts have been associated with rapid cyclogenesis (Uccellini et al. 1985), the development of low-level jets (Uccellini et al. 1987), and the generation of rainbands (Martin et al. 1992). In this case study, the process which initiated the high surface winds is proposed to be the intense downward motion in the upper troposphere that generated an upper-level front and transported high momentum air of stratospheric origin into the troposphere.

B. BOUNDARY LAYER PROCESSES

Once the high momentum air has been brought to the lower troposphere by the strong downward forcing associated with the upper-level front, it is mixed to the surface in the boundary layer by turbulence that is generated by either shear or buoyancy, or by a

combination of the two processes. The boundary layer (also known as the planetary boundary layer or atmospheric boundary layer) is defined as the lowest 1-2 km of the troposphere. The planetary boundary layer responds to external forcing on a time scale of an hour (Stull 1988).

At night the boundary layer is often called the nocturnal boundary layer and, assuming there is no cold air advection, is characterized by stable stratification caused by radiational cooling at the earth's surface. Depending on the strength of the stratification and the amount of shear-driven mechanical turbulence (forced convection), the stable boundary layer may be either weakly turbulent or completely lacking turbulence (Stull 1988). Wind shear at the top of the inversion also creates mechanical turbulence which enhances the entrainment of warm, high momentum air into the top of the boundary layer, thus causing the layer to grow vertically (Gerber et al. 1989). Stull (1988) explains that in a non-turbulent boundary layer the wind shear increases until it can overcome the opposing buoyant damping effect. At that point a "burst" of turbulence is generated that vertically mixes momentum and heat, thereby weakening the wind shear and thus starting the building process again until another "burst" takes place. As discussed previously, the Richardson number is commonly used to determine whether or not turbulence is present, although it does not give a measure of the intensity of the turbulence. Wind shear is generated at the surface by frictional drag from surface roughness elements and in the upper levels of the layer by changes in the geostrophic wind speed and direction with height or air flow over sloping topography at the top of a cold drainage flow. At the bottom of the stable layer (the lowest 2-10 m) the wind direction is dependent upon the local topography and the wind speed is a function of

buoyancy, wind shear, and roughness height, while the winds above the layer are affected by both synoptic and mesoscale forcing in addition to buoyancy and shear (Stull 1988).

As the sun rises and begins to heat the earth, convective turbulence (free convection) takes over as the dominant mechanism by which mixing in the layer is increased as buoyant plumes rise to the top of the layer or even break through to the free atmosphere. Figure 5 is a depiction of the boundary layer structure as it evolves over a 24 hr period (Stull 1988). Shear and convective turbulence erode the inversion that is created by nocturnal cooling and allow entrainment of air from the layer above into the boundary layer. The boundary layer is thoroughly mixed and warmed by a combination of heat flux into the layer from the inversion layer and upward from the earth's surface (Stull 1973).

Transient processes such as cold air moving into a region behind an upper-level front can have a large effect on the planetary boundary layer. At any time of the day, when cold air aloft is advected over a region with higher temperatures in the lower boundary layer levels it causes the top of the layer to sink to the bottom, destroying the original boundary layer structure. A new balanced boundary layer will form within about an hour and will have colder temperatures and higher windspeeds than the original as a result of the air mass from above being mixed into the boundary layer (Stull 1988).

C. SEA-LEVEL PRESSURE REDUCTION

The topography of California ranges from the highest mountain in the continental United States, Mount Whitney at 4391.2 m, to the opposite extreme of 85.5 m below sea level in Death Valley. The distance between these two points is less than 128 km and the

terrain gradients are equally as steep on the western side of the Sierra Nevada range where there is a change of more than 4242.2 m over 64 km. The deviation between surface pressures in this region is primarily a result of these drastic variations in elevation, thus, surface pressures must be reduced to sea level to enable meteorologists to analyze the pressure changes that are caused by weather disturbances (Wallace and Hobbs 1977). In this case study the sea-level pressure analyses will also provide a means by which to assess the degree of cross-isobar ageostrophic flow.

The surface pressure at a station can be reduced to sea-level by using the hypsometric equation, which is given as

$$p_0 = p_g \exp \left(\frac{g_0 Z_g}{R_d \bar{T}_v} \right) \quad (3)$$

when solved for sea-level pressure. Z_g is the surface elevation, p_0 is the sea-level pressure, p_g is the surface pressure, g_0 is the acceleration due to gravity globally averaged at the earth's surface (9.8 ms^{-2}), R_d is the gas constant for 1 kg of dry air ($287 \text{ J deg}^{-1} \text{ kg}^{-1}$), and \bar{T}_v is the mean virtual air temperature of the column between the ground and mean sea level (Wallace and Hobbs 1977). Because there is no way of measuring the mean virtual air temperature of the below-ground column, the root of the problem lies in finding an appropriate estimate of that value.

The most common equation used to calculate the mean virtual temperature is

$$\bar{T}_v = T_g + \frac{\bar{\gamma} Z_g}{2} + C \quad (4)$$

where T_g is the surface temperature, $\bar{\gamma}$ is the mean lapse rate of the column, and C is a water vapor correction applied to adjust for the change in vapor pressure in the below-ground column (U. S. Weather Bureau 1963). The resulting value is substituted into the hypsometric equation (3) to get the sea-level pressure. By assuming a constant atmospheric lapse rate between the surface height at a given station and the sea surface, values for sea-level pressure can be computed from the measured surface temperature and pressure. However, when the station is in a region of elevated or sloping terrain, this formula results in sea-level pressure gradients that are unrepresentative due to the localized irregularities in pressure and surface temperature (Danard 1989). For example, if cold dense air sinks into an isolated valley while the surrounding higher stations have warmer surface temperatures, the valley station will compute the reduced sea-level pressure using a lower temperature and the end result will be a sea-level pressure that is too high (Byers 1974).

Conventional surface hourly observations are required to report altimeter setting, since these stations are located at airports. An altimeter is an aneroid barometer that is marked in height units rather than pressure units and is one way that aircraft measure altitude. The height to pressure relationship is determined by assuming that the column below the station or aircraft meets the criteria for the U. S. Standard Atmosphere. The values for the U. S. Standard Atmosphere are defined such that sea-level temperature, T_0 , is 15°C , sea-level pressure, p_0 , is 1013.25 hPa, and the lapse rate, Γ , is $6.50^{\circ}\text{C km}^{-1}$ (Wallace and Hobbs 1977). The altimeter setting is the value that is read from the instrument when it is calibrated so that sea level equals an altitude of zero. The measured altimeter setting can be substituted for p_0 into the hypsometric equation (3) to obtain the actual surface pressure.

The one-to-one correspondence between altimeter setting and surface pressure results from the assumption of Standard Atmosphere temperature and lapse rate in (4). Altimeter setting represents the simplest approximation of sea-level pressure and, as previously discussed regarding the assumption of a constant lapse rate, is subject to errors if the actual lapse rate or temperature is greater or less than the U. S. Standard Atmosphere. Due to the dependence on surface elevation in the hypsometric equation (3), the error is greater at higher elevation stations.

The National Weather Service uses the hypsometric equation (3) to reduce the surface pressure to sea level for stations that are at elevations under 300 m by assuming that the average of the current surface temperature and the temperature measured 12 h before equals the surface temperature T_g in (4). The surface temperature is averaged in an effort to correct for the change in sea-level pressure caused by the diurnal surface temperature variation (Saucier 1955). The Standard Atmospheric lapse rate is assumed because the station is reasonably close to sea level. This procedure improves the final estimate of sea-level pressure but does not completely solve the problem since it increases the difficulty of forecasting fast-moving mesoscale events by reducing the pressure gradient signal (Weaver and Toth 1990) and induces a semidiurnal variation at most stations (Mass et al. 1991).

For stations above 300 m empirical corrections are applied to get an appropriate value for sea-level pressure (Saucier 1955). The mean virtual air temperature is then determined by

$$\overline{T}_v = \left(\frac{T_{g0} + T_{g12}}{2} \right) + \frac{\gamma Z_g}{2} + C + F \quad (5)$$

where T_{g0} is the current station temperature, T_{g12} is the temperature from 12 h ago, γ is an assumed lapse rate for the surface to sea-level layer that varies with the 12 h average surface temperature and the station location, and F is the Plateau correction (U. S. Weather Bureau 1963). The Plateau correction was developed to adjust the reduced sea-level pressure so that the difference between the annual mean sea-level pressure and the computed value is the same regardless of station elevation (List 1951) and is based on the annual normal value of the mean temperature at a given station (Saucier 1955). The overall effect of this method is an improvement over the assumption of a constant lapse rate, but Sangster (1987) notes that there is a 10 ms^{-1} northerly geostrophic wind component at sea level over the Great Plains in summer and a corresponding southerly component in winter as a result of the Plateau correction.

A number of other reduction methods have been proposed to correct for topographic effects, many of which are based on adjusting the station altimeter setting to correct for a non-standard air mass. This procedure is especially beneficial to this case study since many automated weather stations only report altimeter setting while other stations report sea-level pressure only at synoptic times, but continue to report altimeter setting in reports of special observations. Pielke and Cram (1987) suggest using a derived flat pressure field to calculate a streamfunction-like pressure field. Sangster (1987) uses a similar method to obtain streamfunctions and potential fields of the surface geostrophic wind. Weaver and Toth (1990) introduce a modification to the Sangster reduction in order to apply it to a specific region of interest. Rather than reducing the altimeter setting to sea level, these methods use a reference surface to lessen the height of the column through which the mean virtual

temperature must be assumed. Sangster developed a smooth terrain based on station elevations instead of the existing topography and Weaver and Toth use a pressure height that is similar to the average pressure height in the region of concern. While these methods seem promising, neither Pielke and Cram or Sangster give the desired output of sea-level pressure. In addition, the Weaver and Toth adjustments do not apply well to this case study because one of the main concerns is the ageostrophy of the winds offshore, making reduction to sea level a necessity. Benjamin and Miller (1990) recommend a reduction method that uses the 700 hPa temperature to approximate an “effective” surface temperature in order to eliminate the diurnal errors that result from using surface temperature directly. In this case, in which there is an upper-level front affecting the 700 hPa temperatures, the resulting sea-level pressure field would be biased. Danard (1989) proposes two methods to calculate the surface horizontal pressure gradient but does not reduce the pressure to sea-level at each station. None of the methods described would be effective in this case in which an upper-level front is moving southward across the greatly varying terrain of the state of California.

Fujita (1989) generated a mesoanalysis that reduces the effects of air mass temperatures that are skewed from the standard atmosphere by comparing the mean sea-level pressure with the mean altimeter setting and then applying a correction factor to get the reduced sea-level pressure. This method of reduction of pressures to sea-level is explored further in the next chapter.

III. DATA AND METHODOLOGY

A. DATA

In order to provide complete documentation of the high wind incident, surface data from a variety of sources is presented. Surface Airways (SA) observations provide the greatest areal coverage but the reports are taken at airports, thus they tend to be located near regions of large populations. For California that means that there are many stations near San Francisco and Los Angeles, others strung out along California Highway 99 either close to the center of the San Joaquin Valley or to the east side, and the rest spread across a vast region (Pauley et al. 1996).

Observations from several other state agencies are also included in the analyses in order to provide additional evidence of high winds in the data sparse regions. The California Department of Water Resources takes automated observations at approximately 85 California Irrigation Management Information System (CIMIS) stations that are situated in agricultural regions across the state (Pauley et al. 1996). The observed parameters are not the same as those recorded by SA data because the goal of the system is to give the farming industry information on irrigation timing. CIMIS sites provide hourly averages of solar radiation, soil temperature, air temperature, relative humidity, 2 m wind speed and direction, and precipitation. In the San Francisco Bay area data from the Bay Area Meteorological Network, operated by the San Francisco Air Quality Board, is designed to assist in forecasting the location of pollutants in the atmosphere. It is comprised of 47 sites around the San Francisco Bay that make hourly observations of the wind speed and direction,

surface temperature, and the change in temperature over the past 24 h. Offshore buoys record air and water temperature, significant wave height, wind speed and direction, and sea-level pressure.

All of the observations used are converted to meter, kilogram, second units. The CIMIS winds are extrapolated to the standard anemometer height by multiplying the value at 2 m by 1.38 based on the equation

$$u_{10} = u_2 \frac{\ln \left(\frac{10}{z_0} \right)}{\ln \left(\frac{2}{z_0} \right)} \quad (6)$$

in which u_{10} is the wind speed at 10 m, u_2 is the wind speed at 2 m, and z_0 is the roughness length. The roughness length for cut grass, approximately .03 m, is used in this equation (Stull 1988) and a logarithmic wind profile is assumed (as expected in a neutral surface layer condition).

A research version of the NORAPS (Navy Operational Regional Atmospheric Prediction System) mesoscale data assimilation system is used to generate the upper air analyses presented in this case study (Hodur 1987, Barker 1992, Liou et al. 1994). The data added into the initialization step of the model includes upper air observations, both rawinsonde and pibal, satellite-derived cloud-tracked winds, temperature soundings, conventional aircraft reports, and surface wind speed gathered from the Navy's operational database (Baker 1992). Observations taken by aircraft using ACARS [ARINC (Aeronautical Radio, Inc.) Communications, Addressing, and Reporting System] provide wind direction

and speed automatically every 7.5 min starting at takeoff and continuing through the entire flight and are also included in the NORAPS analyses (Benjamin et al. 1991). The data assimilation system run is performed with 60 km resolution, 6 h updates, 36 sigma levels and an optimum interpolation analysis calculated at standard pressure levels. The end result is a set of analyses that has higher resolution and less smoothing than the corresponding LFM (Limited-area Fine Mesh) analyses done by the National Meteorological Center (now the National Centers for Environmental Prediction).

B. METHODOLOGY

Hand-plotted analyses for a region including California, Nevada, and Oregon are presented in the next chapter in order to provide a more detailed depiction of the surface meteorological situation than is available from the National Centers for Environmental Prediction (NCEP) operational analyses. In order to fill in the gaps in the observed data, altimeter settings are converted to sea-level pressure for those stations below 300 m that do not report sea-level pressure. 300 m is chosen because below that level the National Weather Service does not apply the plateau correction, thus making the correction consistent for all nearby stations (Saucier 1955). As explained previously, the hypsometric equation can be used to convert the altimeter setting to sea-level pressure.

For stations that are higher than 300 m, the sea-level pressure reduction technique developed by Fujita (1989) (see discussion in Chapter 2) is investigated to determine its possible usefulness in filling in the high altitude data sparse regions. For a time period throughout which high surface winds persisted, 1200 through 2300 UTC 14 November, the

average sea-level pressure and average altimeter setting are computed for a 3°latitude by 7°longitude region in which key high altitude reports were missing. These values are then plotted and analyzed (not shown) as well as the difference between the sea-level pressure and altimeter setting (Fig. 6) in order to determine whether there is an altitude relationship from which a correction factor can be extracted. In the vicinity of the primary stations of interest, TRK (Truckee) and TVL (South Lake Tahoe), the relationship is poor and suggested no obvious solution. The possibility of a temporal relationship is explored by plotting the values of sea-level pressure minus altimeter setting for stations in the region that reported both values (Fig. 7) for the same time period as in Fig. 6. When compared to the same graph generated for stations that are at altitudes very close to sea level (Fig. 8) it is apparent that for the high elevation stations the change in time is too large to apply a constant correction factor to the altimeter reports. Thus, for this case study it is determined that there is not an appropriate correction that can be applied to the altimeter setting that will result in an accurate sea-level pressure value for the high altitude stations.

IV. RESULTS

The sailing vessel Griffin radioed a distress call before dawn on November 14th (Jones 1993) and more than 50,000 residences in California lost electrical power for up to several hours between 0600 UTC 14 November (2200 PST 13 November) and 2000 UTC 14 November (1200 PST 14 November) as a result of fallen power lines and trees due to high winds (Storm Data 1993). A discussion of the synoptic situation at upper and lower levels of the troposphere and observational evidence to support the hypothesized cause of the damaging surface winds are presented in the following sections. The association between the events in the upper and lower levels of the troposphere is explained in order to clarify the connection between the intense downward motion at upper levels and the boundary layer processes that then mixed the high momentum air to the surface.

A. UPPER-LEVEL SYNOPTIC SITUATION

In this section the upper-level synoptic situation will be explained using the NORAPS analyses in order to provide evidence of the upper-level frontal system and associated tropopause folding which initiated the transfer of high momentum air to the lower troposphere. The 0000 UTC 14 November analyses of height and wind speed for 300, 500, 700, and 850 hPa are shown in Fig. 9(a-d) while Fig. 10(a-d) depicts the height, temperature, and potential temperature gradient for the same valid time and levels. The same parameters are presented at 0600 UTC 14 November in Figs. 11(a-d) and 12(a-d), at 1200 UTC 14 November in Figs. 14(a-d) and 15(a-d), at 1800 UTC 14 November in Figs. 19(a-d) and

20(a-d), at 0000 UTC 15 November in Figs. 21(a-d) and 22(a-d), and at 0600 UTC 15 November in Figs. 24(a-d) and 25(a-d).

At 0000 UTC 14 November, an upper-level ridge is located over the East Pacific and a long-wave trough extends south across the western United States producing meridional flow over the coast (NCEP analysis, not shown). A jet streak and associated short-wave trough have moved over the top of the ridge and begun to dig south and strengthen such that by this time they are located over Washington at 300 hPa with a 65–70 m s^{-1} wind maximum (Fig. 9a). At 500 and 700 hPa (Figs. 9b and c) the highest winds, 50–55 m s^{-1} and 35 m s^{-1} respectively, are shown to be over Oregon and northern California at both levels with the maximum winds at 700 hPa located to the west of the 500-hPa wind maximum. At 850 hPa (Fig. 9d) the highest winds are offshore from northern California at 20–25 m s^{-1} .

The winds at all levels are supported by reports from the rawinsonde network, although the station at Medford, Oregon failed to report winds at both 300 and 500 hPa and the 300-hPa winds are missing at Salem, Oregon (Figs. 9a and b), a data void which is not uncommon in the vicinity of a strong jet streak. A Canadian rawinsonde at Castlegar (YCG) reports 65 m s^{-1} winds at 300 hPa but the analysis did not extend the 65–70 m s^{-1} contour to include the report, which may mean that the observation was erroneously rejected by the quality control system and that the region of the highest winds at 300 hPa should be larger. The strong gradient in wind speed on the cyclonic side of the jet streak at 300 hPa is verified by the ACARS reports of a flight over Washington (Fig. 9a), but there are no reports that specifically support the maximum winds at 500 hPa (Fig. 9b). Overall, the continuity

between the winds at 300 and 500 hPa seems reasonable but below 500 hPa, where fewer observations are available, vertical continuity is not as good.

The 300-hPa potential temperature gradient (Fig. 10a) is strongest on the cyclonic side of the jet streak and has warm air to the east and cold to the west, which indicates that the level of maximum winds is below 300 hPa due to the thermal wind relationship

$$\frac{\partial \mathbf{V}_g}{\partial \ln p} = - \frac{R}{f} \mathbf{k} \times \nabla_p T \quad (7)$$

where \mathbf{V}_g is the geostrophic wind, R is the radius of curvature, f is the Coriolis parameter, p is the pressure, and T is the temperature (Holton 1992). At 500 and 700 hPa (Figs. 10b and c) the warm and cold regions are reversed, thus the level of maximum winds must be between 300 and 500 hPa. The strongest temperature gradients at 300 and 500 hPa are nearly vertically stacked and have equal magnitudes although the width of the region affected by the strong gradient is greater at 500 hPa. Between 500 and 700 hPa (Figs. 10b and c) there is a corresponding region of tight gradient over northern California that strengthens from the northeast, at 500 hPa, to the southwest, at 700 hPa. The location of this area of strong gradient at 700 hPa appears to be directly below the right-front exit region of the jet and thus is surmised to be supported by the downward motion and consequent warming of the air as it descends from the level of maximum winds.

The charts presented for the 0000 UTC 14 November valid time [Figs. 9(a-d) and 10(a-d)] clearly highlight the presence of an intensifying upper-level front and jet streak. At all levels there is cold advection over southern Washington and northern Oregon which

contributes to the downward transport of high momentum air by increasing the downward motion. As discussed in Chapter 2, cold air advection skews the direct and indirect cells in the jet streak entrance and exit regions respectively so that downward motion is strongest directly below the level of maximum winds, adding to the frontogenetical effect of confluence.

At 0600 UTC 14 November, the time that marked the start of the wind induced power outages in California, the strongest winds at 300 hPa (Fig. 11a) are still located over Washington and remain 65-70 m s^{-1} . The wind maximum at 500 hPa (Fig. 11b) remains 50-55 m s^{-1} though it does move south into central California. At 700 hPa the contour surrounding the 35-40 m s^{-1} wind maximum increases in area significantly and digs south over the northern San Joaquin Valley (Fig. 11c), directly above the region affected by strong surface winds and simultaneous with the timing of the reports. The 850-hPa winds (Fig. 11d) have increased to 25-30 m s^{-1} along the southern Oregon and northern California coast, a location which is north of the maximum winds at 0000 UTC (Fig. 9d).

The fact that there are no rawinsonde observations at this time indicates that the analyses for this valid time depend heavily on the model first guess, which is the 6 h forecast from the previous run. For that reason, and because of the lack of coherence between the ACARS reports and the analyses, the winds at this time are not as reliable as those given by the previous set of analyses [Fig. 9(a-d)]. Three ACARS observations taken over central California all report 60 m s^{-1} winds at 300 hPa, but the analysis (Fig. 11a) only has a 50-55 m s^{-1} contour drawn around the region. At 500 hPa (Fig. 11b), an ACARS report of 50 m s^{-1} is located over central California, to the west of the 50-55 m s^{-1} contour. The ACARS

winds at both 300 and 500 hPa suggest that a more accurate location for the maximum winds is slightly to the west of the analyzed position, although due to the fact that the ACARS reports included in the analyses may be within ± 3 hours of the analysis valid time and ± 25 hPa of the given pressure level, it is impossible to say for sure. The ACARS reports over central Nevada do indicate a closed circulation, thus supporting the analyzed position of the low height center at 300 hPa (Fig. 11a).

The 300-hPa temperature gradient (Fig. 12a) is not as well organized as it was in the previous 6 h, indicating a weakening of the front at this level, but the 300-hPa low height center that had been located over central Idaho drops south to central Nevada, thus tightening the height gradient between the ridge over the eastern Pacific and the west coast trough. This also causes the flow to shift to a more northerly direction over northern California. Both the 500-hPa and 700-hPa temperature gradients (Figs. 12b and c) have strengthened on the cyclonic side of the jet streak, to maxima of $6^{\circ}\text{K} (100\text{km})^{-1}$ and $9^{\circ}\text{K} (100\text{km})^{-1}$, respectively, such that the gradient continues to be most intense at 700 hPa. The orientation of the isotherms still indicates that cold air advection is taking place in association with the intensifying upper-level front at these levels, but this is also much stronger at 700 hPa.

The 500-hPa omega (Fig. 13) has increased in the past 6 h with a maximum located to the west of the analyzed 300-hPa wind maximum (Fig. 11a), corresponding to the location of the right-front exit region of the highest 300-hPa winds, which is consistent with the expected location of convergence and descent as a result of the ageostrophic wind component flowing towards higher heights in the exit region of the jet (Keyser and Shapiro

1986). The tilting term is frontogenetical and the upper-level front is thus enhanced as a result of the downward vertical motion being located on the warm side of the front. The omega maximum is also directly above the highest 700-hPa winds (Fig. 11c), an additional indicator of downward transport of high momentum air to the lower levels of the troposphere.

At 1200 UTC 14 November the rawinsonde stations are once again reporting, and the analysis indicates that the 300-hPa jet streak maximum has increased to 70-75 m s⁻¹ and moved south to the border between central California and Nevada (Fig. 14a), although it still lags the short-wave trough as in the previous 6 h. The wind maxima at 500, 700, and 850 hPa (Figs. 14b, c, and d) have moved south, as the short-wave trough and associated low height center shift south over south-central California and southern Nevada, and have maintained constant maximum wind speeds of 55-60 m s⁻¹, 35-40 m s⁻¹, and 25-30 m s⁻¹ respectively. The wind maximum at 850 hPa is located completely over the open water west of the San Francisco Bay, while at 700 hPa the maximum is located slightly further south, extending along the coast from San Francisco to Vandenberg Air Force Base (VBG).

The analyzed low height center at 500 hPa (Fig. 14b) is to the west of a northerly wind reported by a rawinsonde station at Mercury, Nevada (DRA) which may be interpreted to mean that the low height center should actually be stacked more from the north to the south than from the northeast to southwest as shown. The wind maxima from 300 hPa down to 700 hPa are sloped from northeast to southwest and seem to show good correlation between the levels, and any slight change in the orientation of the height contours would

most likely not have a significant effect on the location and intensity of the analyzed wind maxima.

The temperature gradient intensifies at 850 hPa (Fig. 15d) over northern California while the gradient at 700 hPa (Fig. 15c) maintains intensity, but the size of the $3^{\circ}\text{K} (100 \text{ km})^{-1}$ contour shrinks. At both 300 and 500 hPa the size of the strong gradient region increases (Figs. 15a and b) and is still strongest to the cyclonic side of the peak winds at 500 hPa, but at 300 hPa the strongest gradient extends from the right-front quadrant of the jet exit region into the base of the short-wave trough.

There are two significant 500-hPa omega maxima over California (Fig. 16) by 1200 UTC 14 November. The first is the same region, the right-front quadrant of the jet, and at the same intensity, at least $20 \mu\text{b s}^{-1}$, as the strong downward motion that was present 6 h before (Fig. 13). This omega maximum now coincides with the 500-hPa wind maximum (Fig. 14b), is to the east of the highest 700-hPa winds (Fig. 14c), and is directly above the maximum temperature gradient at 700 hPa (Fig. 15c). This change equates to a reduction in the intensity of the momentum that is being transported downward from 700 hPa although the strength of the downward transport itself remains strong. The second 500-hPa omega maximum (Fig. 16), also with a $20 \mu\text{b s}^{-1}$ contour, is positioned to the right of the highest 300-hPa winds (Fig. 14a) and directly behind the 500-hPa maximum winds (Fig. 14b), a location in which downward vertical motion may be expected based on the direct circulation cell shifting to the anticyclonic side of the jet due to cold air advection as discussed previously. A second cell of strong downward vertical motion was also analyzed in the 1991 dust storm case (Pauley et al. 1996), but in the present case the analyzed location appears to

be directly above the Sierra Nevada mountains instead of on the leeward side. This second region of strong downward motion may be a combination of the effects of topography and the cold air advection aloft.

A cross-section along a line extending through the axis of the short-wave trough and the 500-hPa wind maximum (line D-D' in Fig. 14b) and at the front of the 300-hPa jet streak exit region depicts both the 1.6×10^{-6} and $3.0 \times 10^{-6} \text{ K m}^2 \text{ kg}^{-1} \text{ s}^{-1}$ (1.6 and 3.0 PVU) potential vorticity surfaces (Fig. 17). Both values have been used to define the level of the tropopause (WMO 1986 and Spaete et al. 1994). Here, the 1.6 PVU surface portrays tropopause folding extending just below the 700-hPa level at 1200 UTC 14 November. The cross section also reveals the level of maximum winds to be between 350 and 475 hPa as indicated by the cold air at 300 hPa on top of warm air at all levels below 500 hPa on the west side of the axis of maximum winds. The strongest winds are located directly above the upper-level front, depicted by the region of most tightly packed isentropes, and it is easily seen that the front does not extend to the surface. Soundings taken at Mercury, Nevada (DRA) depict the lowering of the tropopause with time from 275 hPa at 0000 UTC 14 November to 375 hPa by 1200 UTC the same day (Fig. 18). Mercury is located to the west of the upper-level frontal zone through the period and, although the 1200 UTC cross-section is taken slightly north of DRA, by extrapolation it is approximately 1000 km from the eastern point of the cross-section (Fig. 17). A comparison between the stability of the DRA sounding with the stability at the corresponding point in the cross-section shows excellent continuity in the height of the tropopause between the two locations, which provides concrete evidence of the

lowering of the tropopause as a result of the evolution of the upper-level front and associated tropopause fold.

1800 UTC 14 November is not a synoptic observation time, and thus there are no rawinsonde reports. The analyses presented are predominantly from the first guess fields, as discussed previously with respect to 0600 UTC 14 November. The 300-hPa low height center (Fig. 19a) has moved slightly south over the past 6 h and is now encircled by a closed isoheight line and is becoming cut-off from the support of the polar front jet. The maximum winds at 300 hPa have weakened to 55-60 m s^{-1} (Fig. 19a), although ACARS reports over Nevada indicate that the velocity gradient on the cyclonic side of the jet streak should be stronger and that the maximum winds should be at least 60-65 m s^{-1} . The winds at 500 and 700 hPa (Figs. 19b and c) show no change in intensity as they move south with the short-wave trough and upper-level “closed low”, but there are no reports in the vicinity of the maximum winds by which to verify the analyses. The 850-hPa winds have decreased to 20-25 m s^{-1} (Fig. 19d) and this is reflected at the surface in the decrease of the winds at the buoy offshore of VBG from 16 to 13 m s^{-1} .

Weak warm air advection ahead of the wind maxima increases at all levels as the upper-level front and jet streak start to move through the base of the short-wave trough. The temperature gradient at 500 hPa (Fig. 20b) continues to strengthen as the 700 hPa gradient (Fig. 20c) weakens so that the gradient is now stronger at the upper level, signifying a reduction in the strength of the tropopause fold and the associated upper-level front. 500-hPa omega (not shown) has weakened but the two separate maxima are still apparent with the region to the south still corresponding to the right-front quadrant of the 300-hPa wind

maximum, while the second is now located near the axis of the 300-hPa wind maximum (Fig. 19a). The southerly maximum is centered on the axis of maximum winds at 500 hPa (Fig. 19b) as in the previous 6 h. The position and intensity of the downward motion thus further highlights a decrease in the transport of high momentum air to the lower troposphere, and a weakening of the upper-level front.

By 0000 UTC 15 November the 300-hPa winds (Fig. 21a) have shifted south with a single $55\text{--}60\text{ m s}^{-1}$ maximum extending southwest from central Nevada to the coast of California, just east of VBG. ACARS reports in the vicinity of the entrance region of the jet streak indicate that the maximum winds should be positioned further to the west and that the maximum winds over Nevada and central California are most likely not as strong as depicted by the analysis. At 500 hPa the $50\text{--}55\text{ m s}^{-1}$ wind maximum has shrunk and moved over the water south of VBG (Fig. 21b). The winds at 700 hPa (Fig. 21c) have decreased dramatically so that there is only a small region of winds greater than 30 m s^{-1} , and the winds at 850 hPa have also weakened to $15\text{--}20\text{ m s}^{-1}$ (Fig. 21d). There are no reports over the water which can be used to verify the model wind speeds at 500, 700, and 850 hPa, but the decrease at 700 hPa by 0000 UTC 15 November coincides with the cessation of reports of strong, damaging surface winds by land-based stations and buoys.

The temperature gradients show little change over the previous 6 h, with the strongest gradient still at 500 hPa (Fig. 22b), although it is now located southeast of the highest 500-hPa winds rather than directly to the east. Cold air advection into the back side of the trough persists, but the wind maxima have decreased such that there is no significant momentum to be transferred to lower levels. A cross-section that extends southwest to northeast across

southern California (Fig. 23) through the maximum 500-hPa temperature gradient (Fig. 22b) clearly depicts a weakened tropopause fold, with the 1.6 PVU surface only extending down to 475 hPa, and a dissipating upper-level front, with the number of tightly packed isentropes that define the frontal zone having decreased since 1200 UTC 14 November (Fig. 17).

By 0600 UTC 15 November, the low center is vertically stacked, the system is completely cut-off from the support of the polar jet, and the 300-hPa winds have decreased to a 50-55 m s^{-1} maximum (Fig. 24a). The winds at 500 hPa are also 50-55 m s^{-1} (Fig. 24b), but the temperature gradient has weakened and the orientation of the isentropes to the isoheights indicates that cold air advection at 500 hPa has decreased (Fig. 25b), and thus the corresponding downward vertical motion (not shown) is losing support. The 700-hPa winds have decreased to less than 30 m s^{-1} (Fig. 24c) and the temperature gradient has continued to weaken with little cold air advection (Fig. 25c). The 500-hPa omega (not shown) is still depicting downward motion associated with the weak cold air advection, but now it is located to the east of the highest 500-hPa winds, which indicates that the strength of the upper-level front is decreasing.

The data presented in these analyses depict a strong upper-level front that tracks southward across California with associated strong downward vertical motion that is sufficient to transport high momentum to the top of the planetary boundary layer. Figure 26(a-d) presents the soundings taken at VBG at 0000 UTC 14 November, 1200 UTC 14 November, 0000 UTC 15 November and 1200 UTC 15 November and distinctly shows the location of the upper-level front located in the dry 750-650 hPa layer (Fig. 26b) at 1200 UTC 14 November, the same period in time when the 700-hPa wind maximum was beginning to

move south over VBG (Fig. 14c). A comparison of the winds in Figs. 26a and b also indicates that high momentum air is being brought down into the lower troposphere. By 0000 UTC 15 November (Fig. 26c) the location of the front extends down to only 625 hPa and by 1200 UTC 15 November (Fig. 26d) there is no longer an indication of the frontal zone over VBG.

The adiabatic layer extending from the frontal zone to the surface by 0000 UTC 15 November (Fig. 26c) indicates that the nocturnal boundary layer (Fig. 26b) was destroyed by mixing between 1200 UTC 14 November and 0000 UTC 15 November, which would allow entrainment of high momentum air from the lower troposphere into the planetary boundary layer where it could then be mixed to the surface. Unfortunately, no surface observations were taken at VBG during this time period, but observations taken nearby at Point Arguello (Station PTGC1) do show strong surface winds (15 m s^{-1}) beginning at 1200 UTC 14 November, which verify that the high momentum air was mixed to the surface (Fig. 27). The process by which the boundary layer mixing takes place is examined in detail in the next section.

B. SURFACE ANALYSES

In this section, the planetary boundary layer structure and the mechanism by which the high momentum air is mixed to the surface will be examined, and observations from surface airways, CIMIS, and Bay Area Meteorological Network stations, as well as buoy reports, will be presented as supporting evidence. Figs. 28-33 are the sea-level pressure analyses beginning with the 0000 UTC 14 November chart and continuing every 6 hours

until 0600 UTC 15 November. Due to the limited size of the surface chart, not all of the high wind reports are shown.

In Fig. 28 the tightest pressure gradient is over northern California as high pressure ridging southeastward over northern California and Nevada interacts with low pressure troughing northwest over the Sierra Nevada mountains. The weak pressure gradient over central California is under the influence of high pressure ridging east over the San Joaquin Valley, and the tight gradient over southern California is a result of that same high pressure interacting with a second trough of low pressure extending west-southwest from southern Nevada and northern Arizona towards the Los Angeles Basin.

The strong pressure gradient and high winds over northern California at 0000 UTC 14 November (Fig. 28) weaken as the upper-level front passes to the south. Consequently, the gradient over central California and western Nevada tightens by 0600 UTC 14 November (Fig. 29) as the high pressure builds over both northern and central California while the troughing over the Sierra Nevada mountains persists, low pressure over southeast California deepens, and a 1005-hPa low center forms just south of Death Valley. By 1200 UTC 14 November (Fig. 30) the high pressure ridges farther south along the coast, causing the pressure gradient to tighten over the central San Joaquin Valley and central California coast and by 1500 UTC 14 November (not shown) the gradient over the Los Angeles Basin has strengthened slightly.

The pressure gradient along the border between California and Nevada continues to strengthen until 1800 UTC 14 November (Fig. 31) as the high pressure to the north continues to build. By 0000 UTC 15 November (Fig. 32) the gradient along the coast has also started

to weaken as the Sierra Nevada trough begins to fill and shift west and at the same time the ridging over Nevada moves east and weakens slightly, allowing the gradient along the state border to relax slightly. The low pressure center over southern California drops slowly south through the period and fills to a trough by 0000 UTC 15 November, although the gradient over southern California remains fairly strong through 0600 UTC 15 November (Fig. 33).

The winds at coastal northern California stations, Crescent City (CEC) and Arcata (ACV), and offshore at buoy 46027 increase to 7 - 10 m s⁻¹ by 1800 UTC 13 November (not shown) and have a strong ageostrophic component in the direction of the upper-level winds. The winds are strongest at buoy 46027, most likely a function of reduced friction over the ocean, and peak at 0100 UTC with northwesterly winds of 14 m s⁻¹ gusting to 17 m s⁻¹ (Fig. 34). The significant wave height recorded at buoy 46027 increases to 3.1 m by 0200 UTC 14 November in response to the high winds. The winds at all three stations decrease to less than 10 m s⁻¹ by 0500 UTC concurrent with a shift in wind from the northwest to a more northerly direction. The timing of the highest winds coincides with the passage of the maximum winds at 500 and 700 hPa (Figs. 11b and c) and illustrates the propagating nature of the tropopause fold-induced high winds. There is no change in surface temperature evident in the buoy report (Fig. 34) and the surface stations indicate a gradual decrease in temperature (not shown), which is expected at this time of the day as a result of diurnal cooling.

The surface wind speeds increase progressively later at stations to the south of CEC and ACV, in conjunction with the southward propagation of the upper-level front. The efforts to rescue the passengers onboard the sailing vessel Griffin took place 100 km to the

west of Point Sur near the time of sunrise (approximately 1500 UTC) (Jones 1993) and a meteorogram for buoy 46028 (Fig. 35) located near San Martin and to the south of Point Sur indicates that the seas had increased to 5 m by 1200 UTC 14 November as a result of the high winds. The most prolonged high winds are recorded at stations in the northern San Joaquin Valley and San Francisco Bay region, with peak wind speeds during the high wind event reaching close to 20 m s^{-1} at Travis Air Force Base (SUU) (Fig. 36). In association with the increasing surface winds, the observations at many stations show that the surface temperature increases while the dew point temperature and relative humidity decreases.

CIMIS stations in Tehama and Glenn counties, located in the northern San Joaquin Valley, as well as SA stations in the same area report temperature rises between 0200 and 0400 UTC (1800 and 2000 PST) 14 November of as much as 6°C , and sudden drying with associated relative humidity drops of as much as 26% in a hour. The winds increase at the same time, jumping from $4 - 13 \text{ m s}^{-1}$ between 0300 and 0400 UTC at the Tehama county stations. The winds at SUU increase from 3 m s^{-1} at 0500 UTC to 14 m s^{-1} gusting to 17 m s^{-1} at 0600 UTC and, concurrent with the jump in wind speed, the surface temperature warms by 4.5°C (8°F), in opposition to the trend of nocturnal cooling that is evident beginning at 0000 UTC (1600 PDT) 14 November (Fig. 36). SUU reports skies clearing from light scattered cirrus cloud cover to clear during this period.

SFO winds jump from 4 m s^{-1} at 0550 UTC to 9 m s^{-1} gusting to 16 m s^{-1} only 7 min later and reports at many San Francisco Bay Area Meteorological Network sites also indicate a sudden increase in wind speed at 0600 UTC (2200 PDT 13 November). The drying trend is depicted in the meteorogram for San Francisco (SFO) by the drop in dew point

temperature (Fig. 37). The observed wind direction is northerly, approximately a 90° angle to the surface isobars, but the same as the upper-level wind direction. Buoy reports show that the sea surface temperatures are nearly constant (Fig. 34) and surface stations report clear or light scattered cirrus clouds indicating that there is no source of heating near the surface.

These reports indicate that the dry high-momentum air being transported downward from 500 hPa and 700 hPa is reaching the surface, and the fact that the winds are increasing progressively to the south with time, concurrent with the propagation of the upper-level frontal system to the south lends additional support to the proposed hypothesis. The surface temperatures at these stations likewise show increases at this time which is contrary to what normally happens with nocturnal cooling, but consistent with what would be expected from a tropopause fold event in which adiabatically-warmed stratospheric air is mixed to the surface.

The daytime heating-induced convective turbulence that was important in mixing the high winds to the surface in the 1991 dust storm case (Pauley et al. 1996) is obviously not the initial driving mechanism for bringing the high momentum air to the surface in this event, since the sun goes down as the upper-level front travels south across California and the highest surface winds over the San Joaquin Valley and San Francisco Bay start after approximately 0300 UTC (2000 PST) and for the most part remain high throughout the night. Upper-level cold advection does play a role in destabilizing the boundary layer in this event. Figures 38 and 39 depict the 0000 UTC and 1200 UTC 14 November soundings for Oakland respectively, and a decrease in temperature throughout surface to 500-hPa layer by

1200 UTC is clearly evident. In addition to the cold air advection, the wind shear at the top of the planetary boundary layer increases significantly between 0000 UTC and 1200 UTC. Therefore, the initial process by which the high momentum air is mixed to the surface is deduced to be the combined effects of destabilization of the layer by cold air advection aloft and shear generated turbulence at the top of the planetary boundary layer that enables entrainment from the layers above to take place.

The trend towards increasing temperature is reversed at most of the sites by 0900 UTC (0100 PST) 14 November as nocturnal cooling returns to dominate until sunrise. Figure 36 depicts the sudden rise and consequent fall of temperatures throughout the rest of the night at SUU. The effects of the sudden warming last throughout the night however, causing the temperatures at many sites to be 10-23°F higher than those recorded in the previous 24 hours. Wind speeds at many stations, most commonly those at lower elevations, decrease slightly during this period of cooling, between 1100 and 1700 UTC (0300 and 0900 PST) 14 November, which is consistent with Stull's (1988) theory on bursts of turbulence and high momentum breaking through the nocturnal boundary layer and then decreasing as the layer is mixed. The decrease in wind velocity for a few hours at stations that are closer to sea level may also be a reflection of the decrease in turbulence mixing as the nocturnal cooling is reestablished and stability increases in the lower levels of the boundary layer.

The cooling is not strong enough to completely overcome the high momentum that is now present in the lower troposphere and as the sun rises, the effects of daytime heating combine with the shear-induced turbulence at the top of the layer to enhance the mixing process and further increase the surface wind speed so that the highest reported winds over

the period of interest are between 1800-2300 UTC (1000-1500 PST) for many Bay Area and San Joaquin Valley stations (Figs. 31 and 36). At some Bay Area Network stations the wind direction shifts from north-northwest to northeasterly, coincident with the increase in winds after sunrise and the daytime heating, which is more in line with the gradient flow than the upper-level flow, but the shift is not consistent across the region and thus suggests the influence of local topography. There is no apparent shift in the observed wind directions at the stations in the San Joaquin Valley, with observed winds consistently from the north-northwest throughout the period. The high winds over central California and along the coast during the day are thus surmised to be a continuing result of the high momentum air being mixed to the surface.

The propagation of the high winds to the south at the surface extends to the Los Angeles Basin. Winds at stations near Los Angeles increase to 15 m s^{-1} by 1800 UTC 14 November (Fig. 31) and then weaken through the end of the period (0600 15 November UTC, Fig. 33). The wind direction is either from the north (cross-isobaric) or northeast at most southern California stations, suggesting that both upper-level forcing of high momentum air to the surface and the pressure gradient at the surface played a role in the high winds over southern California. Figure 40 is the meteorogram for Los Angeles (LAX).

The winds at most locations across the San Joaquin Valley, San Francisco Bay, and Los Angeles Basin decrease concurrently with the onset of nocturnal cooling (Figs. 36, 37, and 40) and the formation of a stable boundary layer, which decouples the near-surface layer from the free atmosphere, consistent with the process by which the winds in the 1991 dust storm case decrease (Pauley et al. 1996). This may be a coincidence of timing however, as

the surface pressures begin to decrease at the same time and the gradient begins to weaken (Fig. 32) as the upper-level front moves southward over the open water and weakens. The meteorogram for San Francisco (Fig. 37) clearly indicates that the winds start to decrease before the onset of nocturnal cooling, but at the same time as the upper-level front moves out of the region, thus lending further support to the proposed hypothesis of strong surface winds caused by mixing of high momentum air from aloft to the surface.

V. SUMMARY

Documentation has been presented in the previous chapters that provides strong supporting evidence in favor of the theory that the high surface winds over California on 14 November 1993 are the result of intense upper-level frontogenesis and associated tropopause folding that brought high-momentum stratospheric air to the top of the planetary boundary layer where it was then mixed to the surface. The upper-level charts depict a strong frontal zone moving southward across California, and it is apparent from the cross-sections shown that the front never extends all the way to the surface. The downward vertical motion associated with the upper-level front and jet streak is sufficiently strong to transport high momentum air to the top of the planetary boundary layer.

Once there, the high momentum air is entrained into the boundary layer and mixed to the surface. In this particular case the initial mechanism for entrainment and boundary layer mixing is a combination of cold air advection aloft and shear-induced entrainment at the top of the boundary layer that destabilizes the layer and brings high-momentum air into the boundary layer. This is supported by the lack of any indication of a surface front in the reports and by the timing of the event, which made the initial mixing by surface heating an impossibility.

After sunrise, between 1500 and 1600 UTC 14 November, the effects of surface heating are added to the mixing process. The high winds persist through the day on 14 November and appear to dissipate in response to a combination of the development of the nocturnal boundary layer beginning at sunset and the southward propagation and weakening

of the upper-level front and jet streak. The location, timing, and direction of the highest surface winds coincides with the location, timing, and direction of the upper-level front and jet streak at their maximum intensities and this, plus the support provided in the previous chapter, provides conclusive evidence that the damaging surface winds experienced on 13 and 14 November are a direct result of tropopause folding and upper-level frontogenesis.

APPENDIX. FIGURES

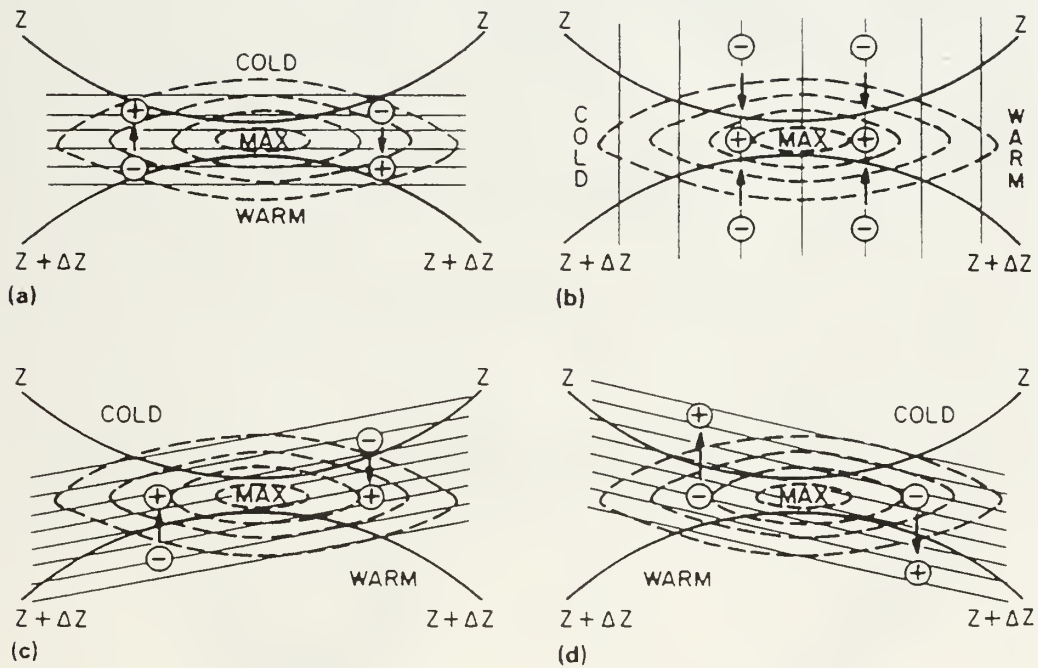


Figure 1. Four-quadrant model of a jet streak shown with the added effects of confluence and shear. Thick solid curves are geopotential height contours (Z), thin solid curves are isentropes, broken curves are isotachs, and arrows depict the direction of the ageostrophic circulation in the thermally direct (northerly arrows) and indirect (southerly arrows) sense. The plus and minus signs represent downward and upward vertical motion respectively. (a) Pure confluence and diffluence without thermal advection; (b) pure horizontal shear (cold advection); (c) confluence and shear (cold advection); (d) confluence and shear (warm advection). From Carlson (1991).

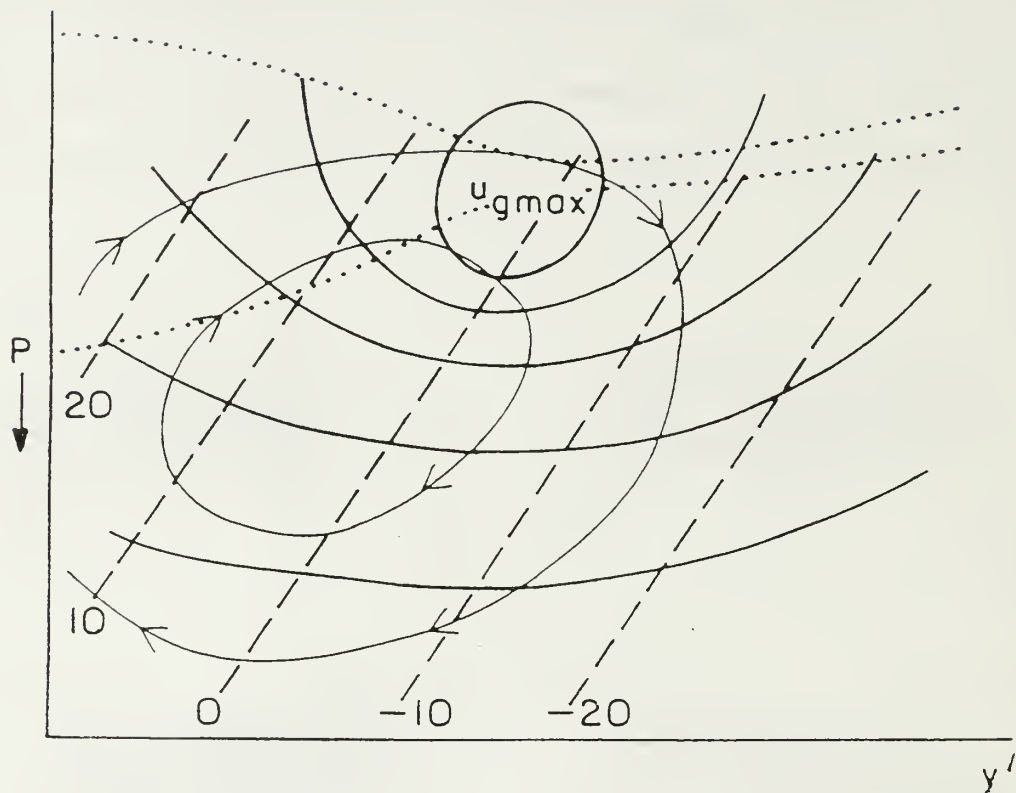


Figure 2. Cross section perpendicular to the jet streak in the entrance region for case of confluence and shear (cold advection) as shown in Fig. 2(c). Thick solid curves are isotachs of the u component of the geostrophic wind (u_g) and broken curves are the v component (v_g), which are tilted in response to the cold advection. Dotted curves are two isentropes and thin solid curves are streamlines of the transverse/vertical circulation, skewed to the anticyclonic side of the jet axis which supports frontogenesis. From Carlson (1991).

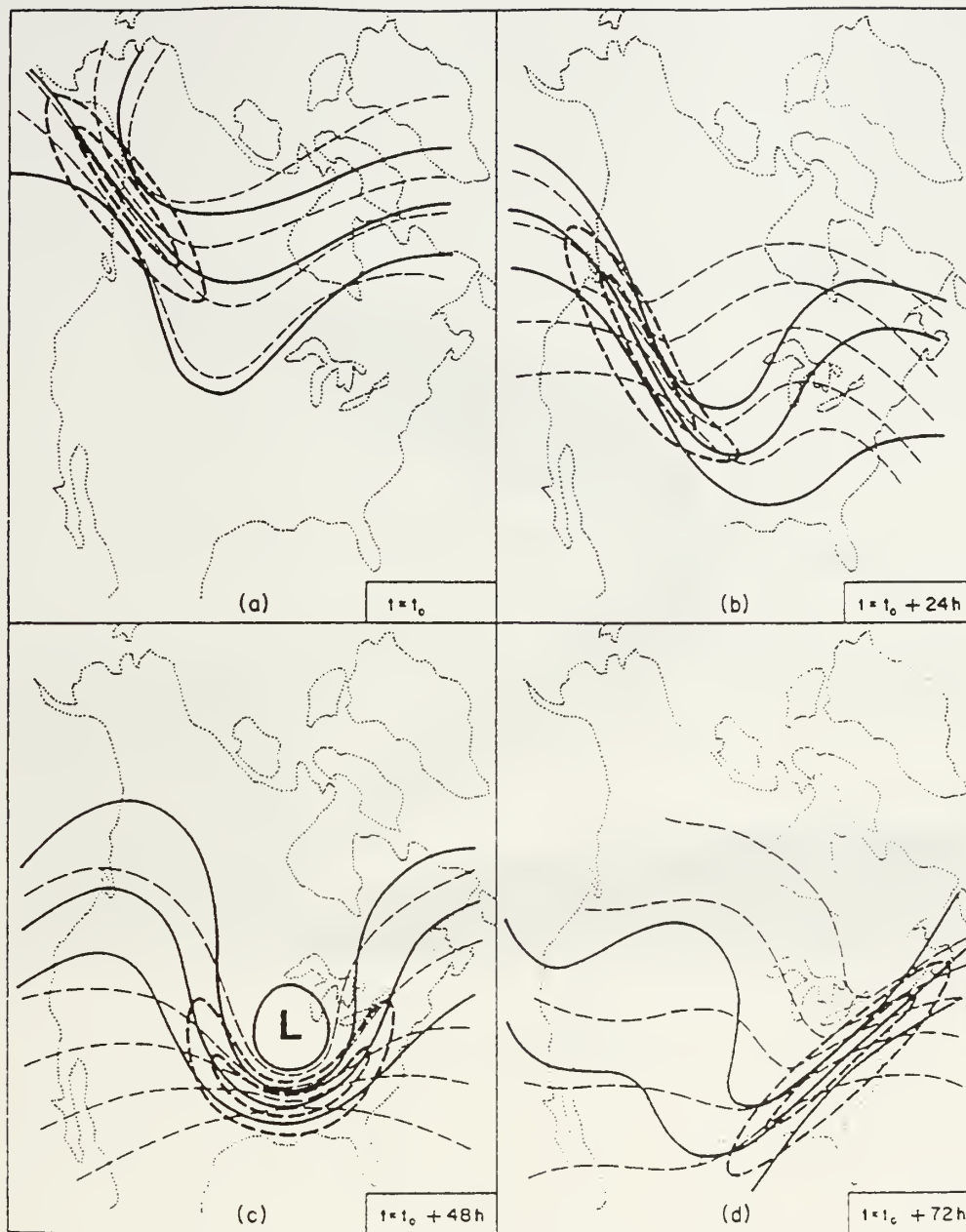


Figure 3. An idealized illustration of the propagation of an upper-level front and jet streak through a mid-latitude long-wave trough over a 72 h period. (a) Upper-level frontogenesis in the confluent region between the mid-latitude ridge and high-latitude trough; (b) jet streak and upper-level front in the northwest flow of an amplifying midlatitude baroclinic wave; (c) system in the base of the fully developed wave; (d) system in the southwest flow of a damping wave. Thick solid curves are geopotential height contours, thin broken curves are isentropes or isotherms, and thick broken curves are isotachs. From Keyser and Shapiro (1986).

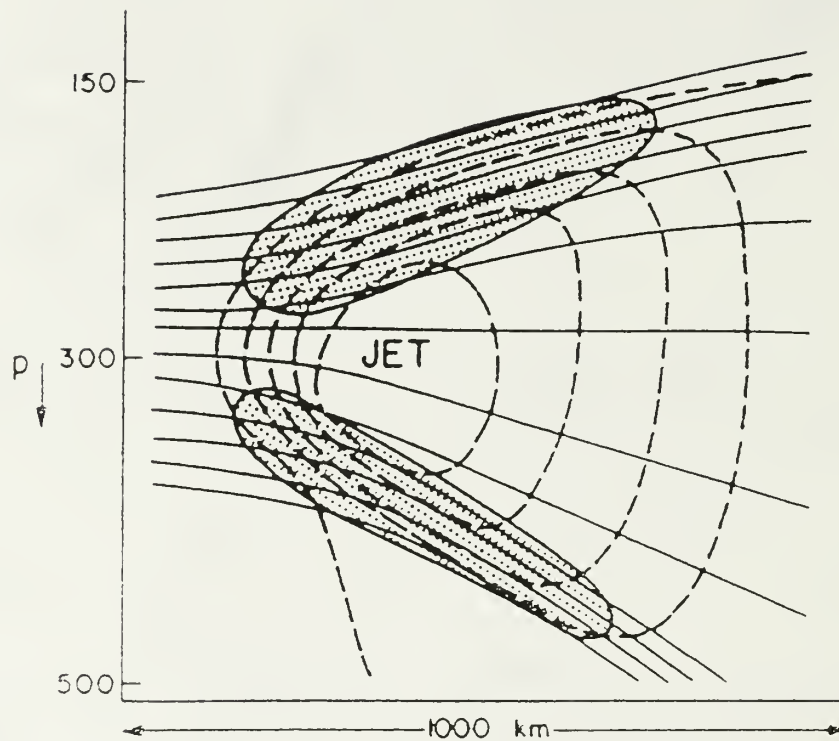


Figure 4. Upper-level front and jet streak with associated regions of clear air turbulence indicated by the stippled shading. Solid curves are potential temperature and broken curves are isotachs. From Keyser and Shapiro (1986).

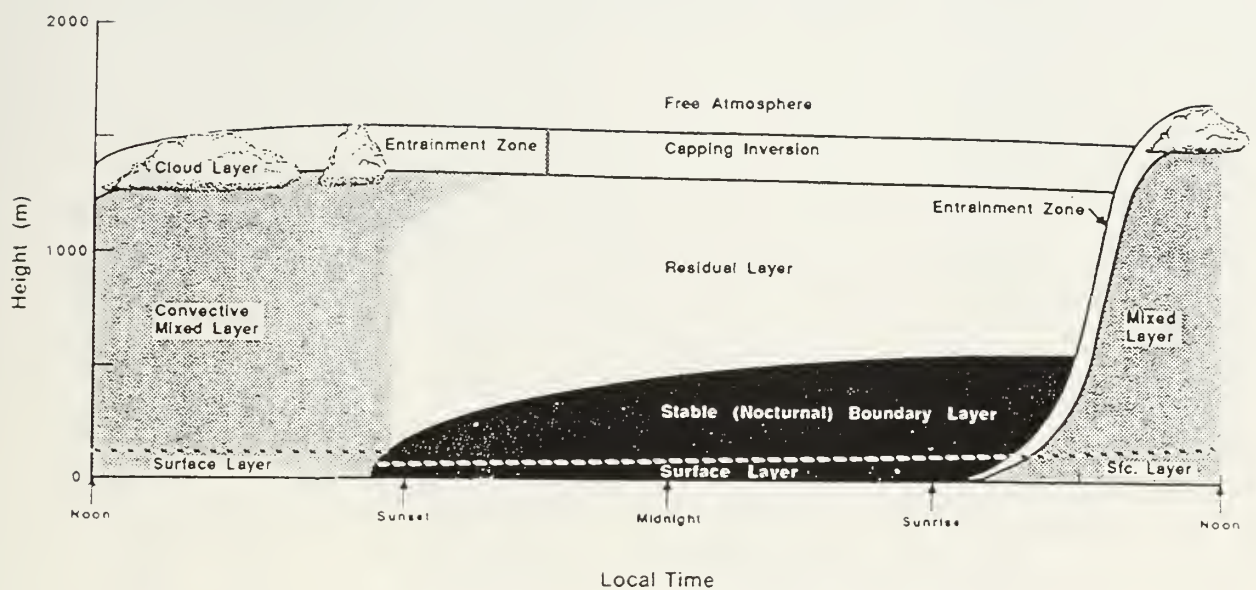


Figure 5. Evolution of the planetary boundary layer over a 24 h period for a region over land dominated by high pressure. The mixed layer is very turbulent, the residual layer contains air that was in the mixed layer, but which is less turbulent, and the nocturnal stable boundary layer is characterized by sporadic turbulence. After Stull (1988).

NORTHERN CA, 12-23Z 14 NOV 93

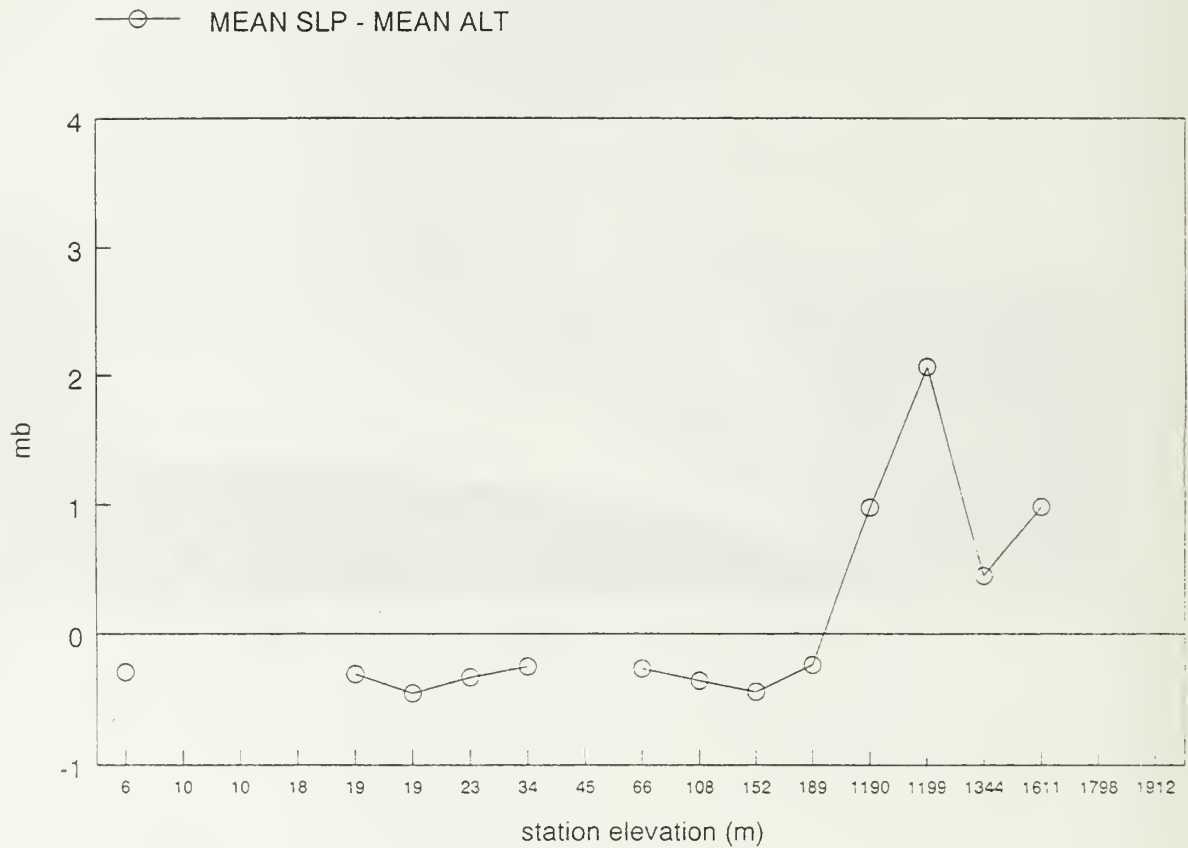


Figure 6. The difference between mean sea-level pressure and mean altimeter setting versus station elevation. For high elevation stations (above 300 m) there is no direct correlation.

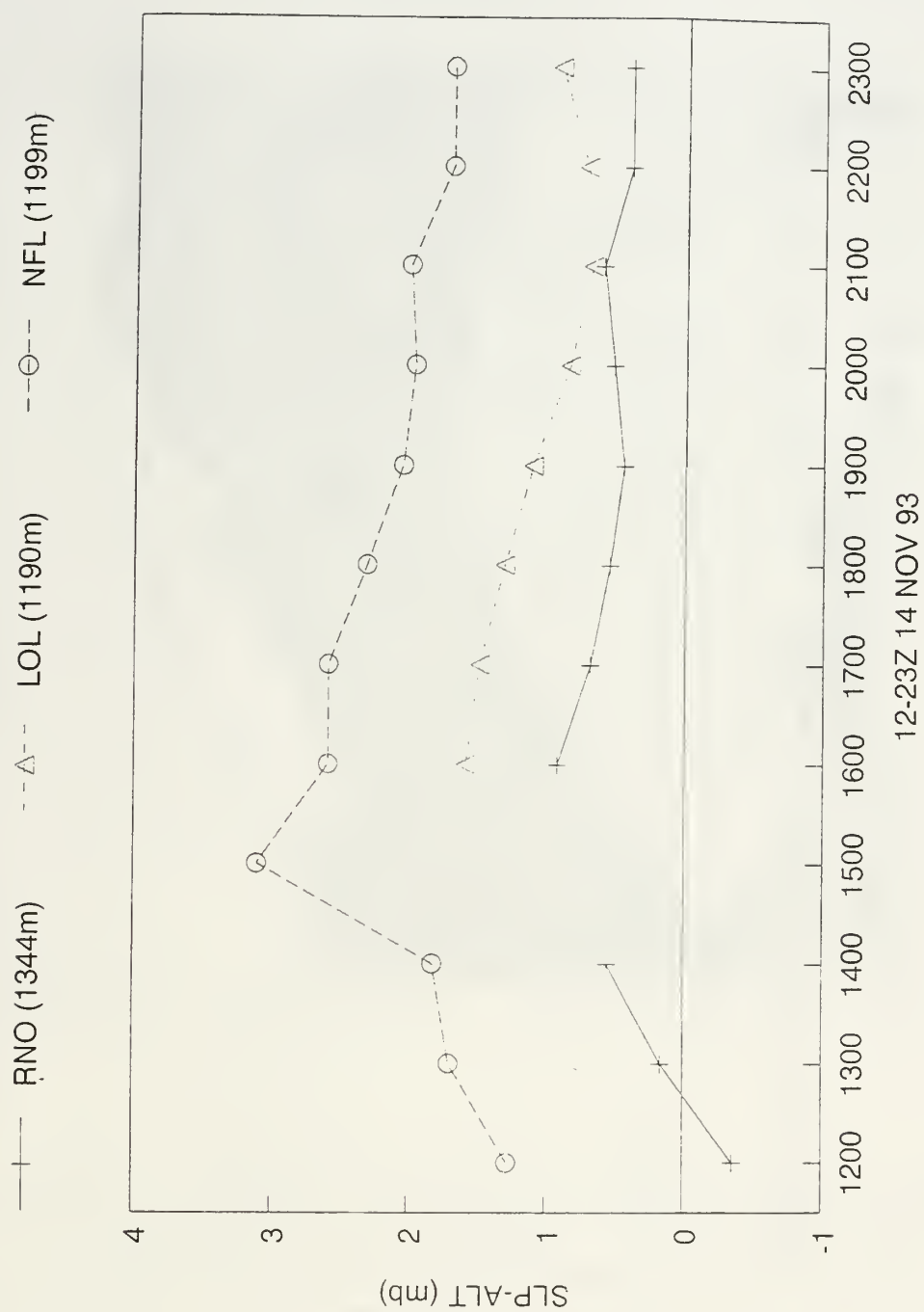


Figure 7. Sea-level pressure minus altimeter setting versus time. For these high altitude stations the change over time is too large to be able to apply a single correction factor. RNO is Reno, Nevada, LOL is Lovelock, Nevada, and NFL is Fallon, Nevada.

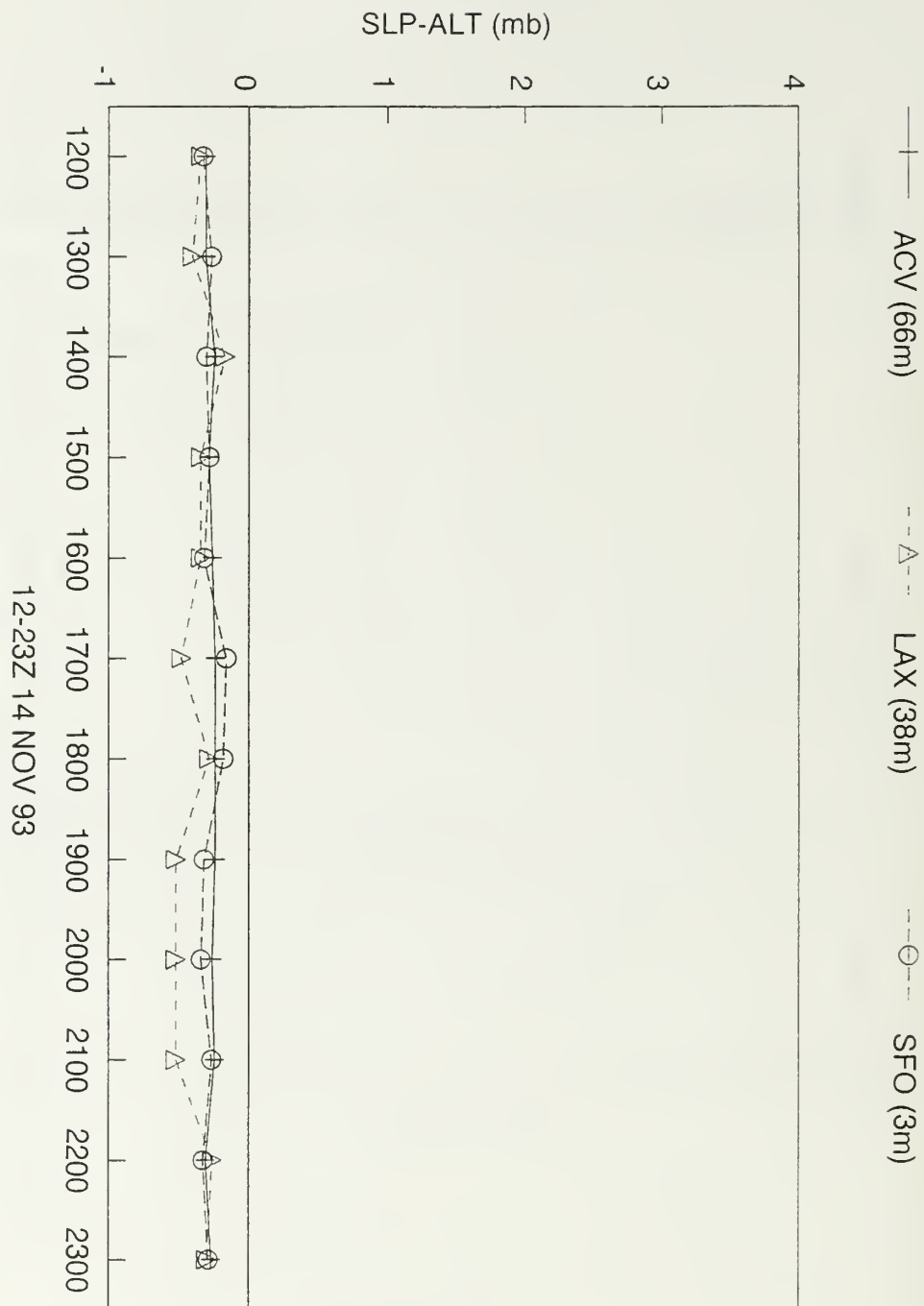


Figure 8. Same as Fig. 7 except that the stations are at altitudes close to sea level. ACV is Arcata, California, LAX, is Los Angeles, California, and SFO is San Francisco, California. A comparison between Fig. 8 and Fig. 7 clearly depicts the problems associated with applying a single correction factor to the high altitude stations.



Figure 9. NORAPS analyses valid at 0000 UTC 14 November 1993. Solid curves are geopotential height (m) and shading is windspeed for (a) 300 hPa, (b) 500 hPa, (c) 700 hPa, and (d) 850 hPa. The contour interval of the isoheights is 120 m at 300 hPa, 60 m at 500 hPa, and 30 m at 700 hPa and 850 hPa. Isotachs are shaded at an interval of every 5 m s^{-1} beginning at 30 m s^{-1} for all levels except 850 hPa which begins at 15 m s^{-1} . On the plotted observations, a flag represents 25 m s^{-1} (48.5 kt) winds, full barbs are 5 m s^{-1} (9.7 kt), and half barbs are 2.5 m s^{-1} (4.9 kt). Letters inside the report circle identify the observation type; R for rawinsonde observation (RAOB), A for ACARS, and F for other aircraft observations. The ACARS and other aircraft observations are valid within 3 h of the analysis time and within 25 hPa of the given pressure level.

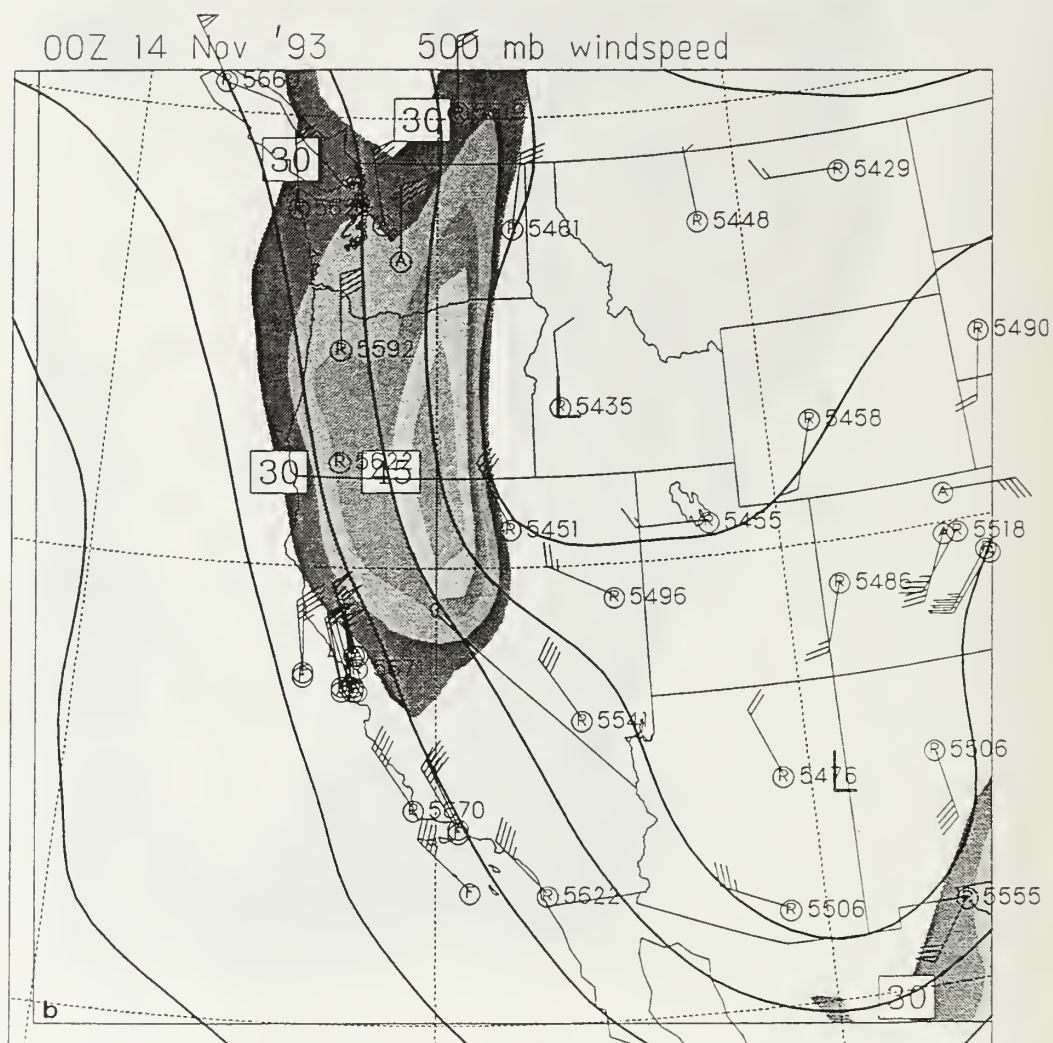


Figure 9. Continued.

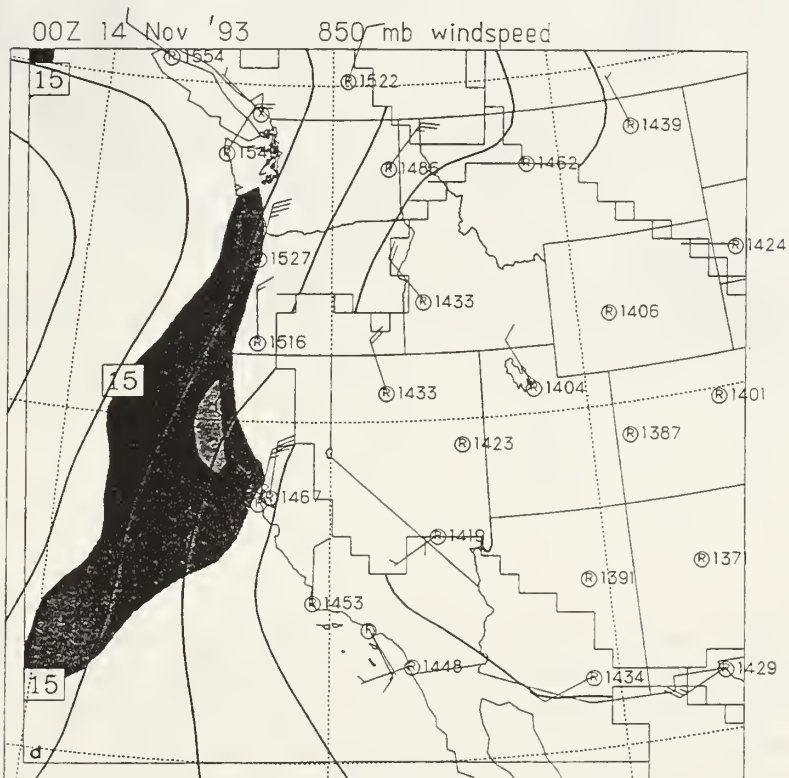
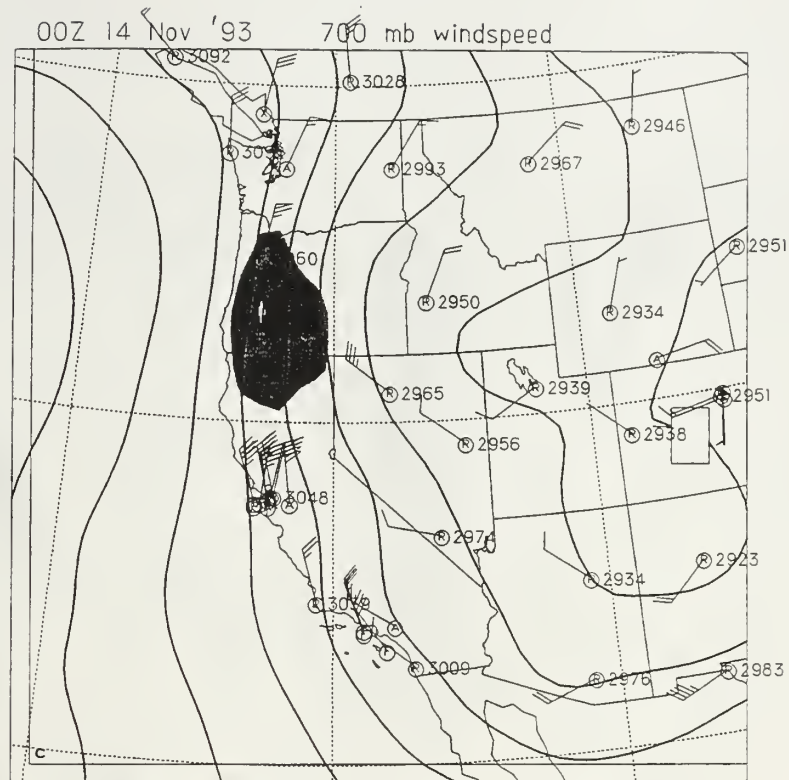


Figure 9. Continued.

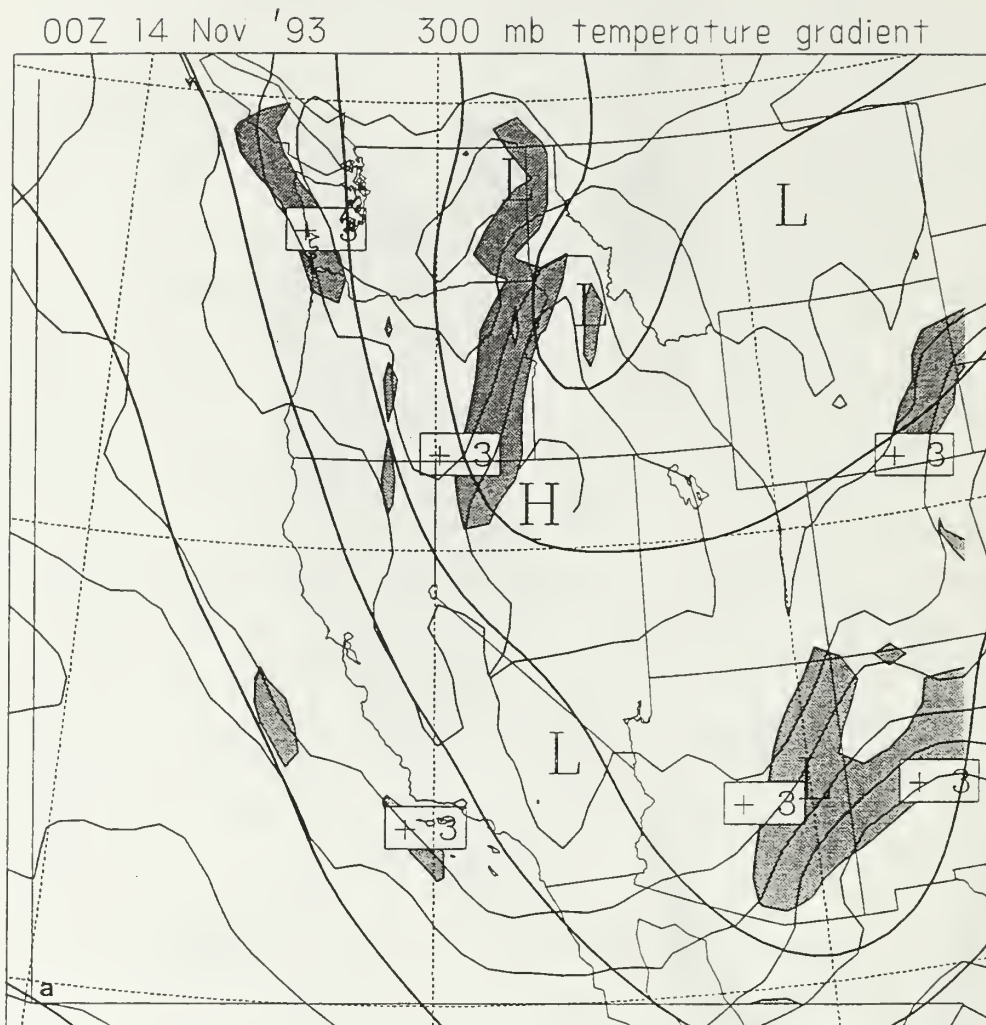


Figure 10. NORAPS analyses valid at 0000 UTC 14 November 1993. Thick solid curves are geopotential height (m), thin solid curves are temperature ($^{\circ}\text{C}$), and shading is the magnitude of the potential temperature gradient [$^{\circ}\text{K} (100\text{km})^{-1}$] for (a) 300 hPa, (b) 500 hPa, (c) 700 hPa, and (d) 850 hPa. The contour interval of the isoheights is as in Fig. 9, the contour interval of the isotherms is 2°C , and the temperature gradient is shaded at a contour interval of $+3^{\circ}\text{K} (100\text{km})^{-1}$ starting with $+3^{\circ}\text{C} (100\text{km})^{-1}$.

00Z 14 Nov '93 500 mb temperature gradient

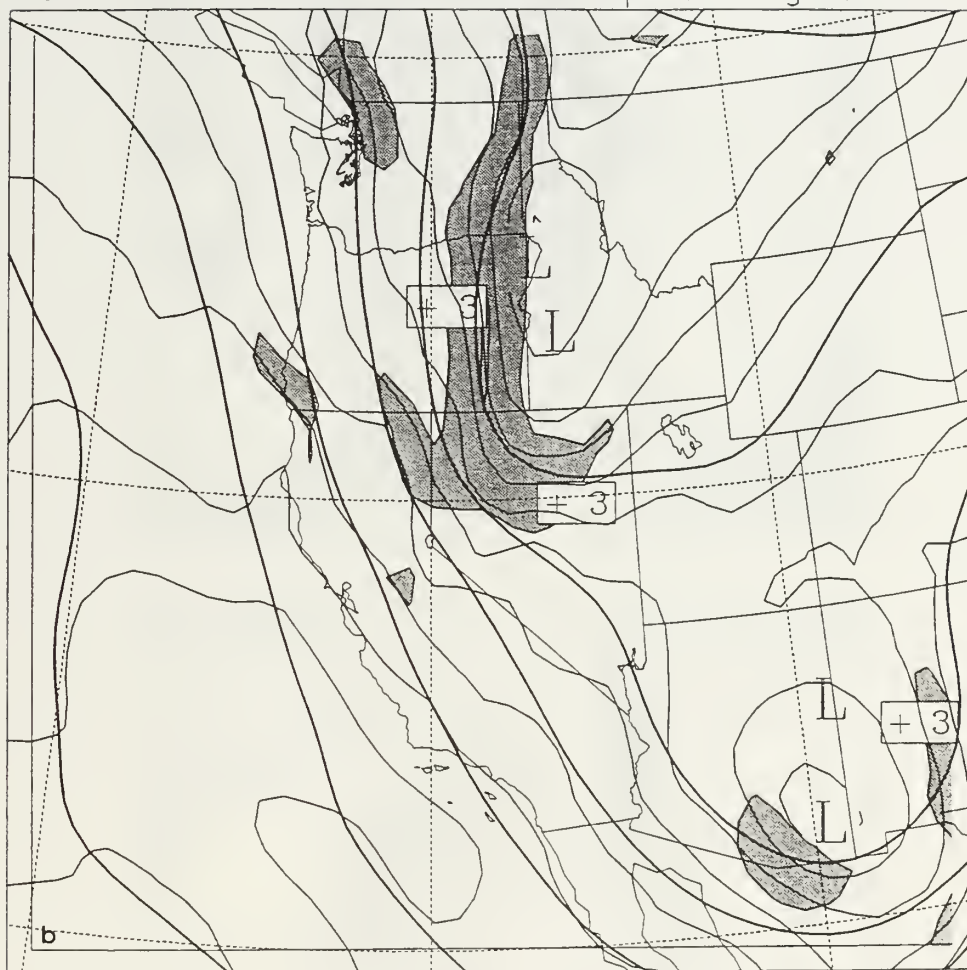


Figure 10. Continued.

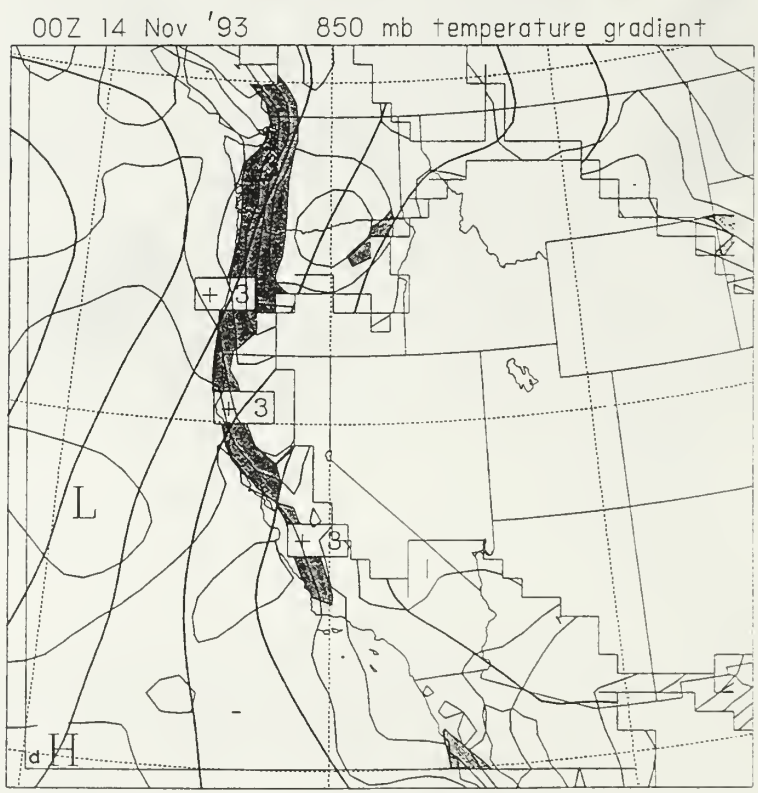
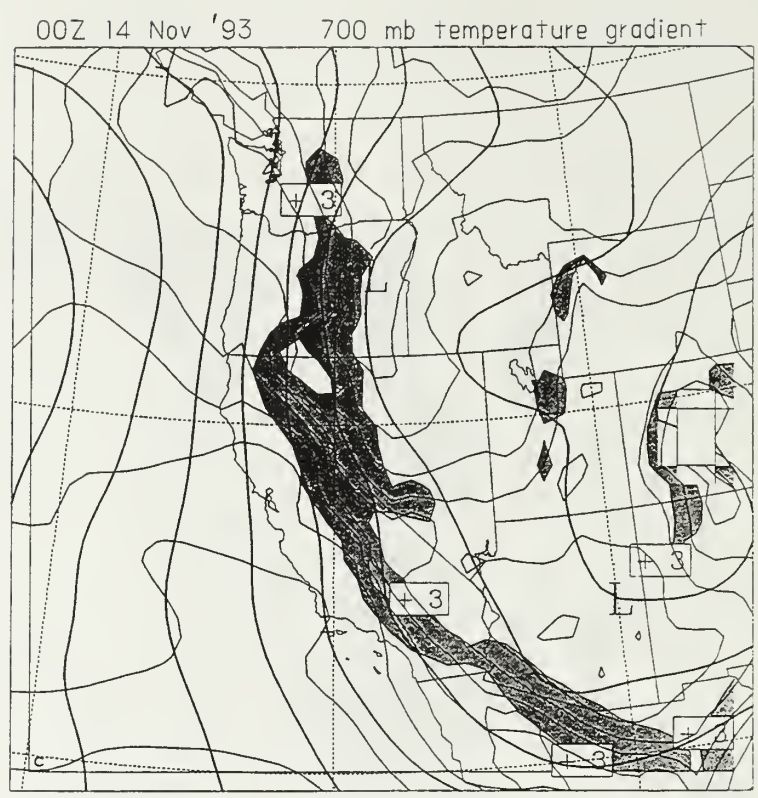


Figure 10. Continued.



Figure 11. Same as Fig. 9 except for 0600 UTC 14 November 1993.

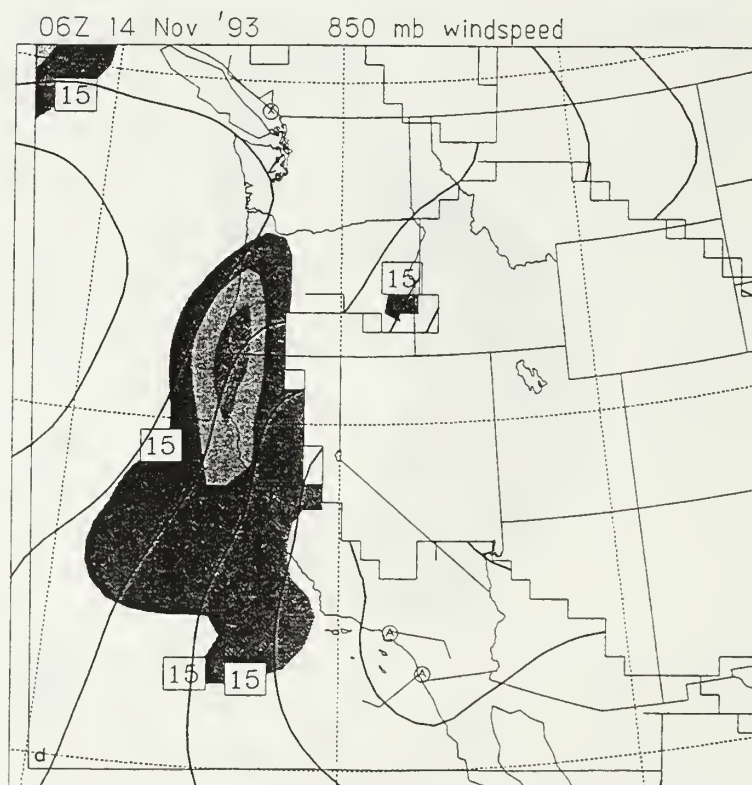
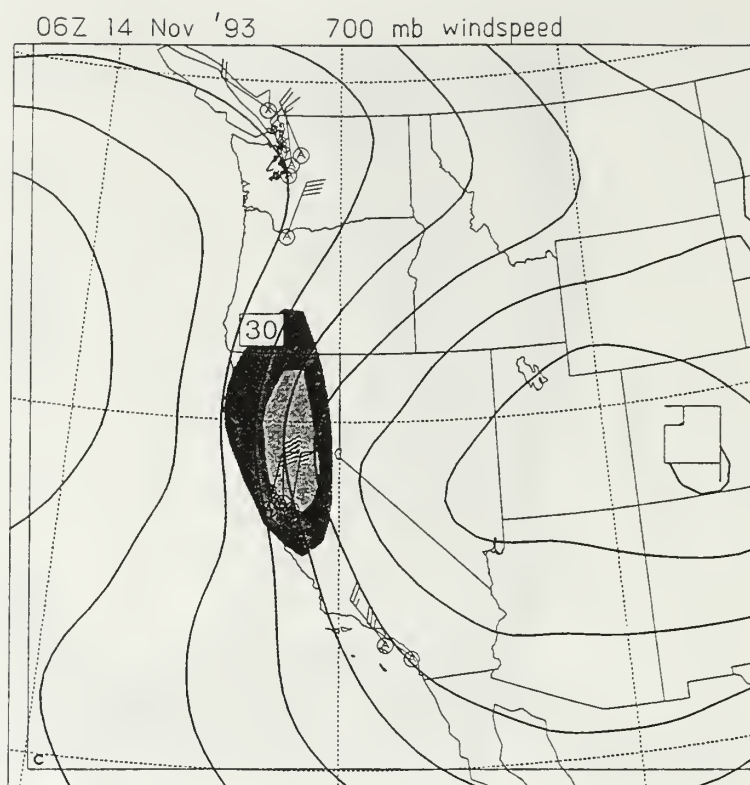


Figure 11. Continued.

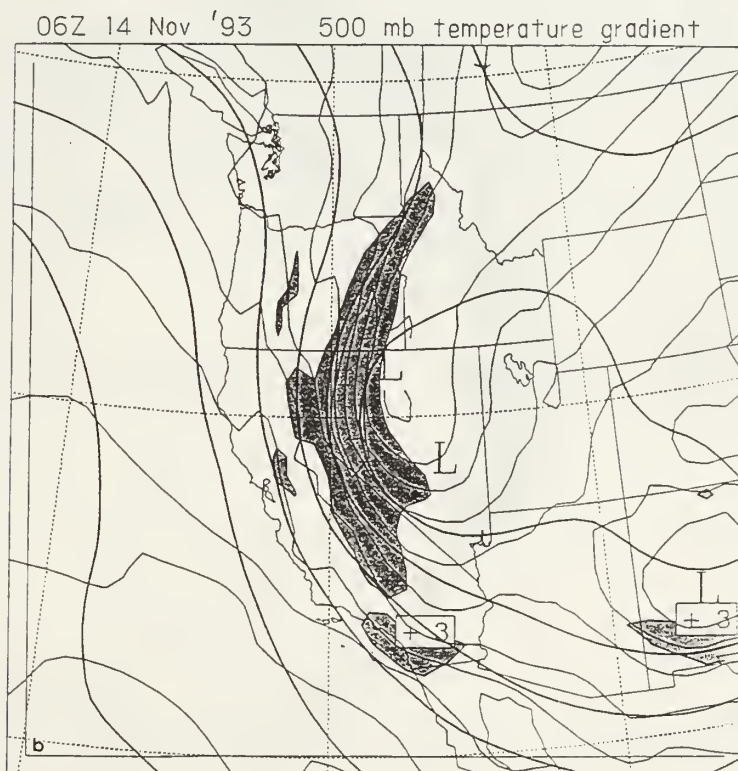
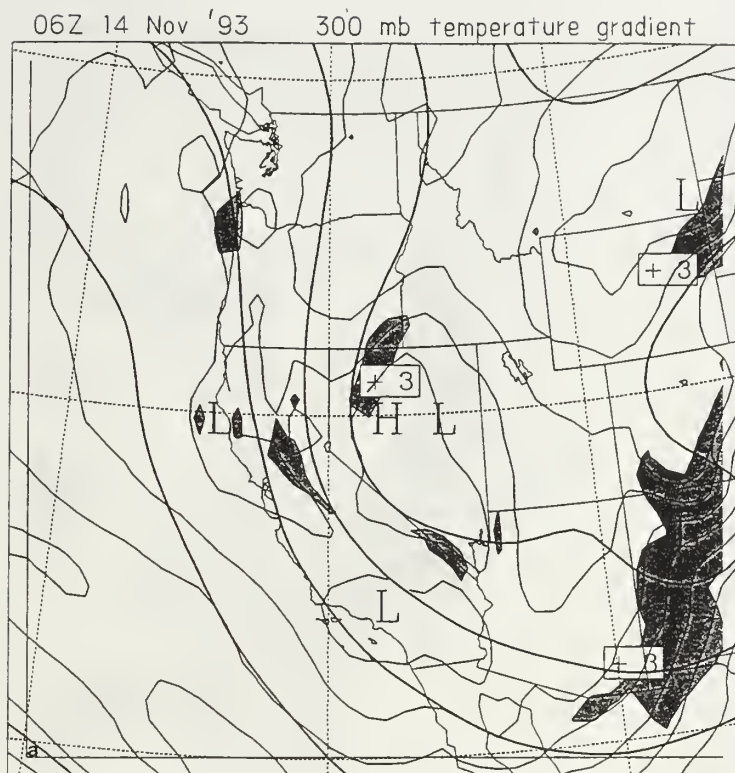


Figure 12. Same as Fig. 10 except for 0600 UTC 14 November 1993.

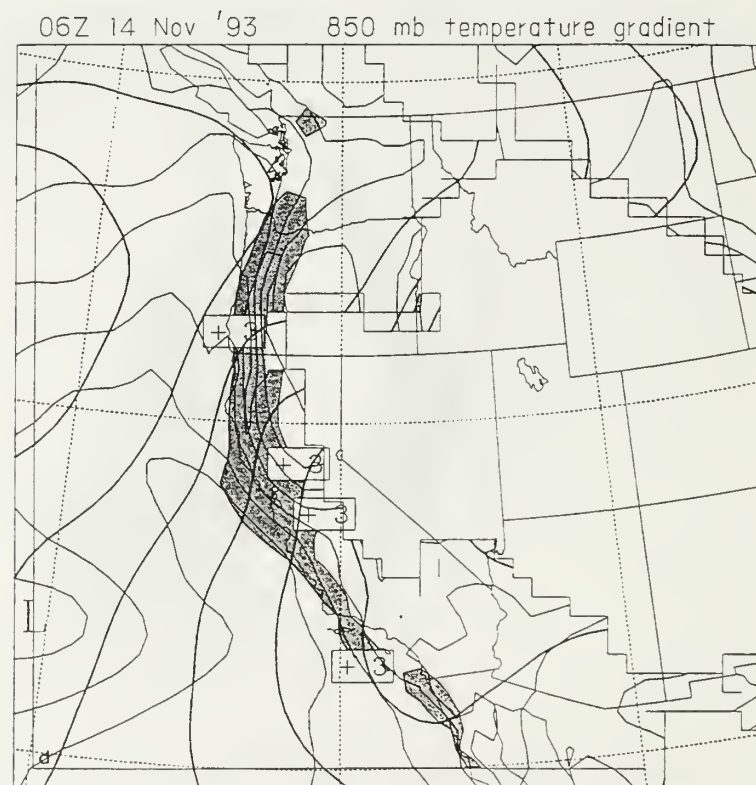
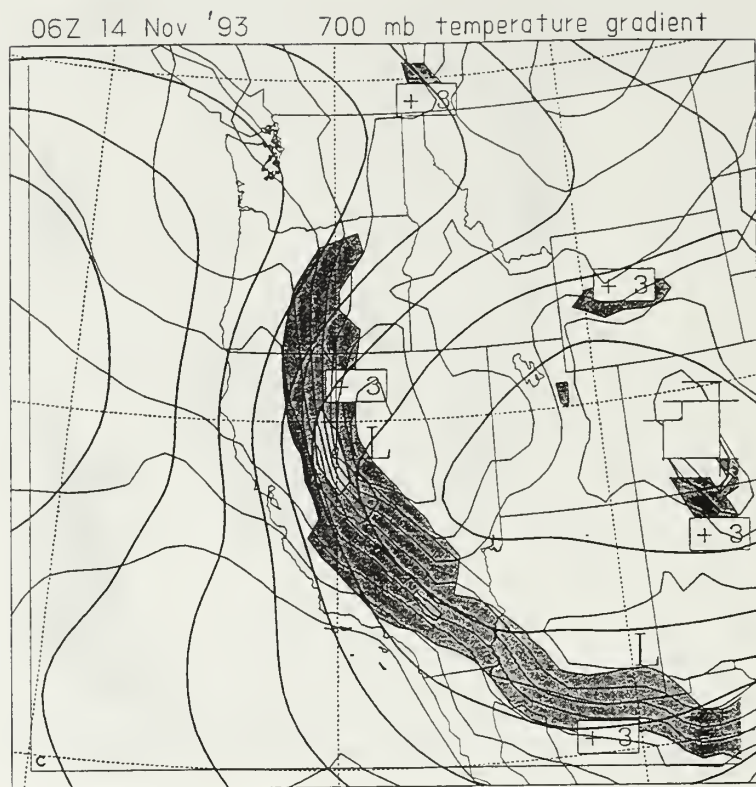


Figure 12. Continued.

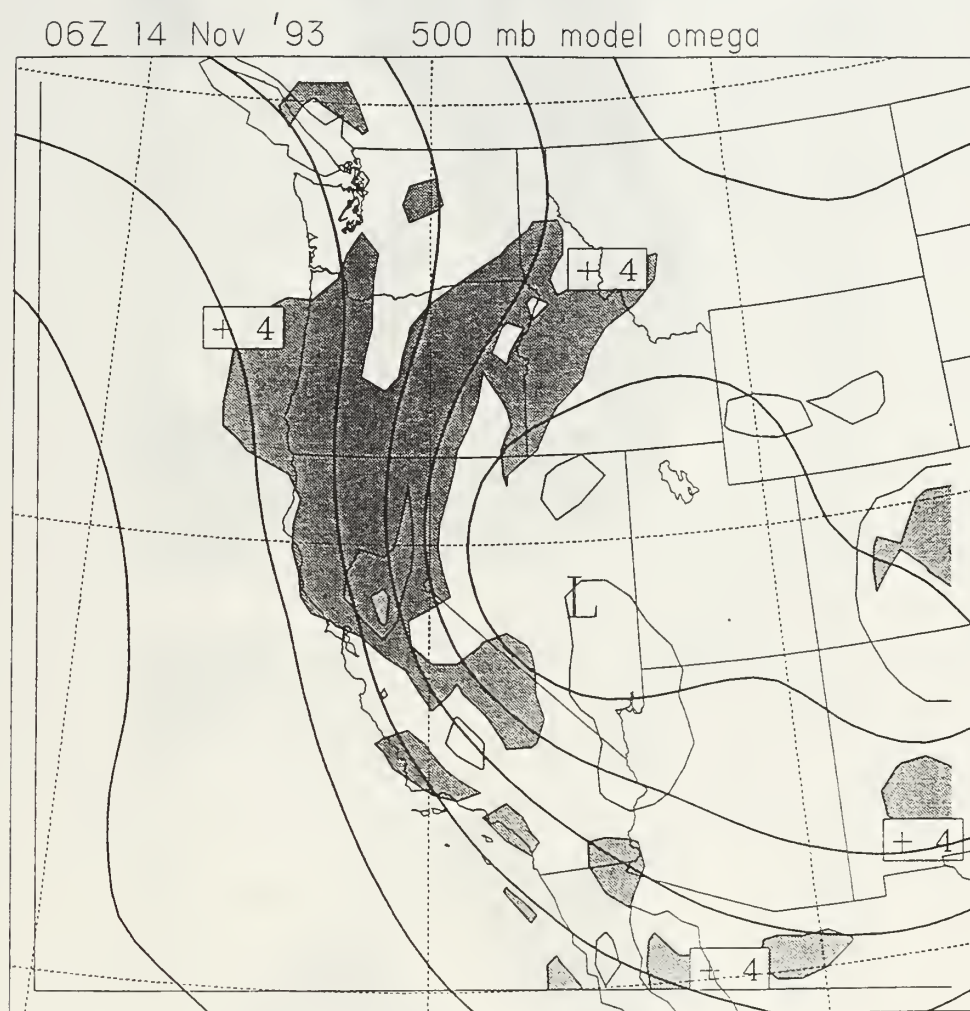


Figure 13. NORAPS analysis valid 0600 UTC 14 November. Thick solid lines are isoheights (m), thin solid lines represent vertical motion, or omega, ($\mu\text{b s}^{-1}$). The contour interval of the isoheights is as in Fig. 9. Shading begins at $\pm 4 \mu\text{b s}^{-1}$ with a contour interval of $8 \mu\text{b s}^{-1}$.

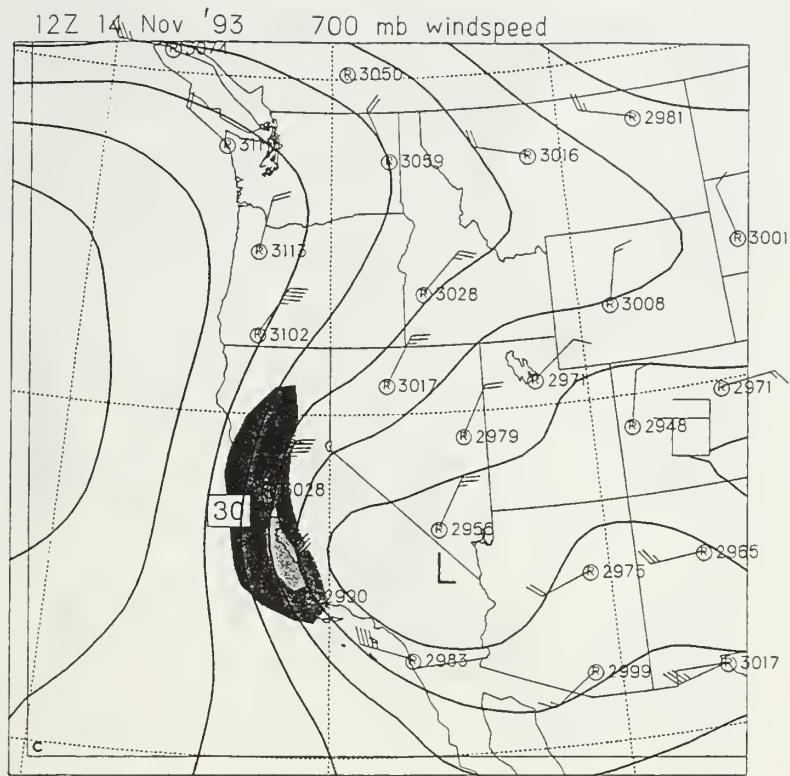


Figure 14. Continued.

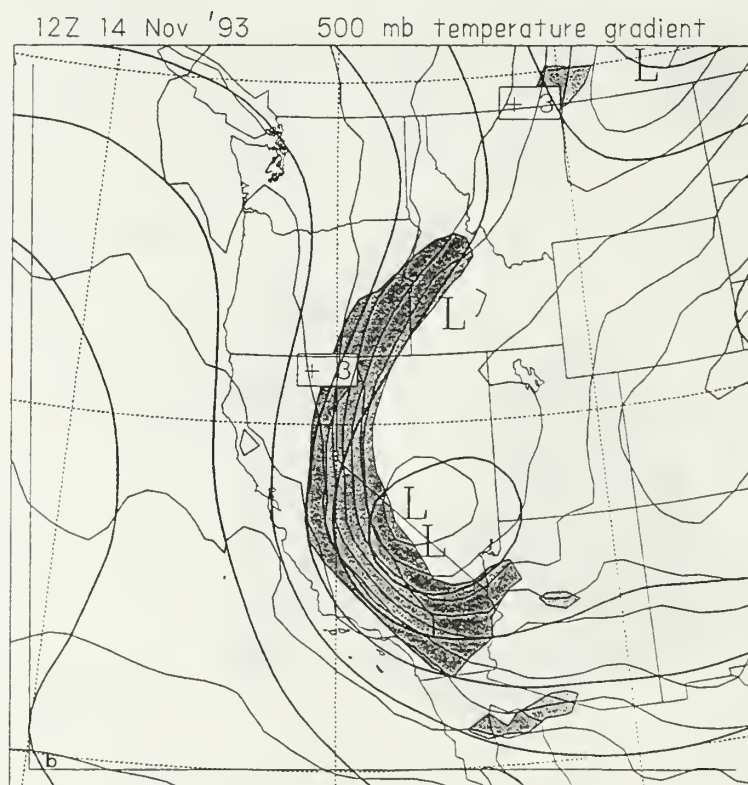
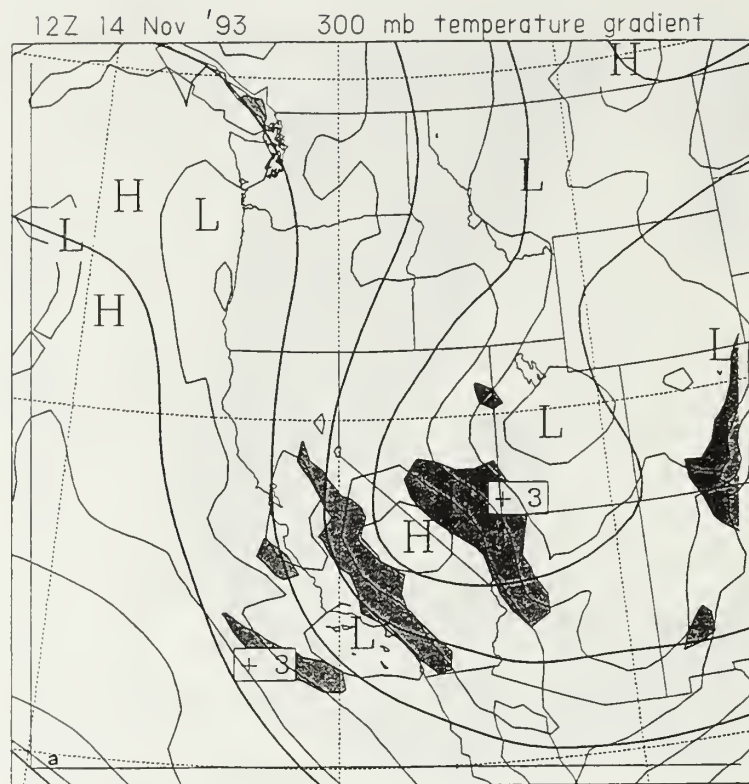


Figure 15. Same as Fig. 10 except for 1200 UTC 14 November 1993.

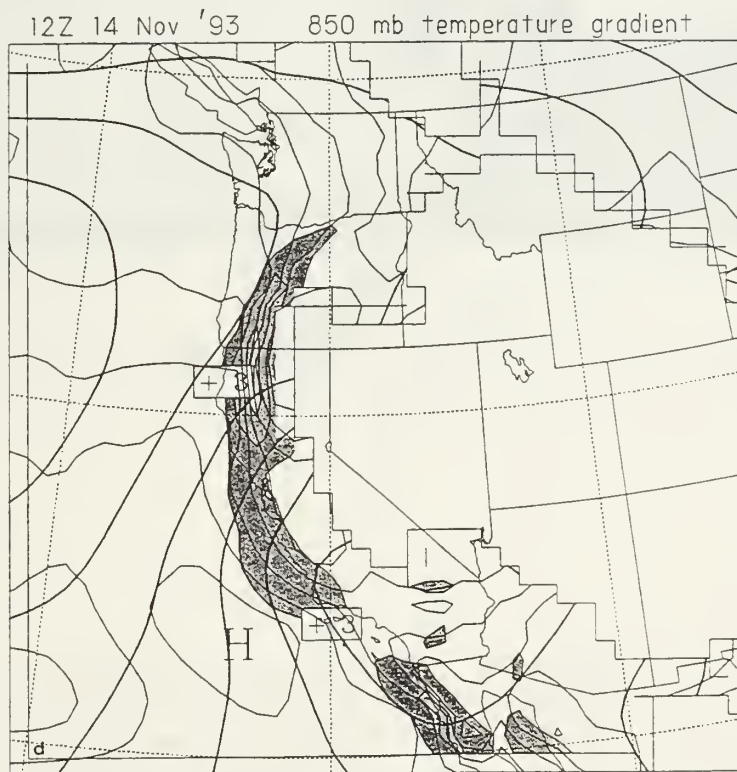
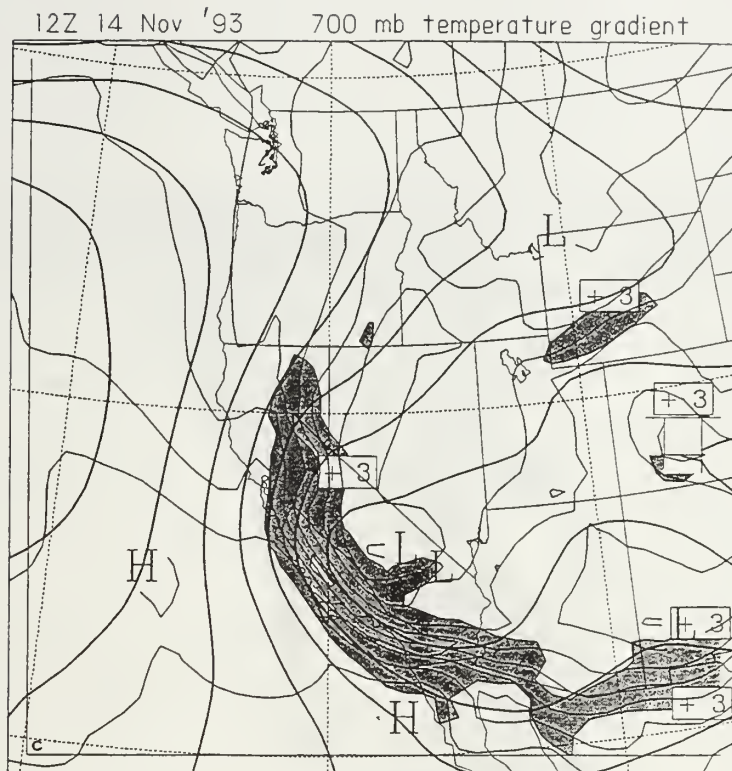


Figure 15. Continued.



Figure 16. Same as Fig. 13 except for 1200 UTC 14 November 1993.

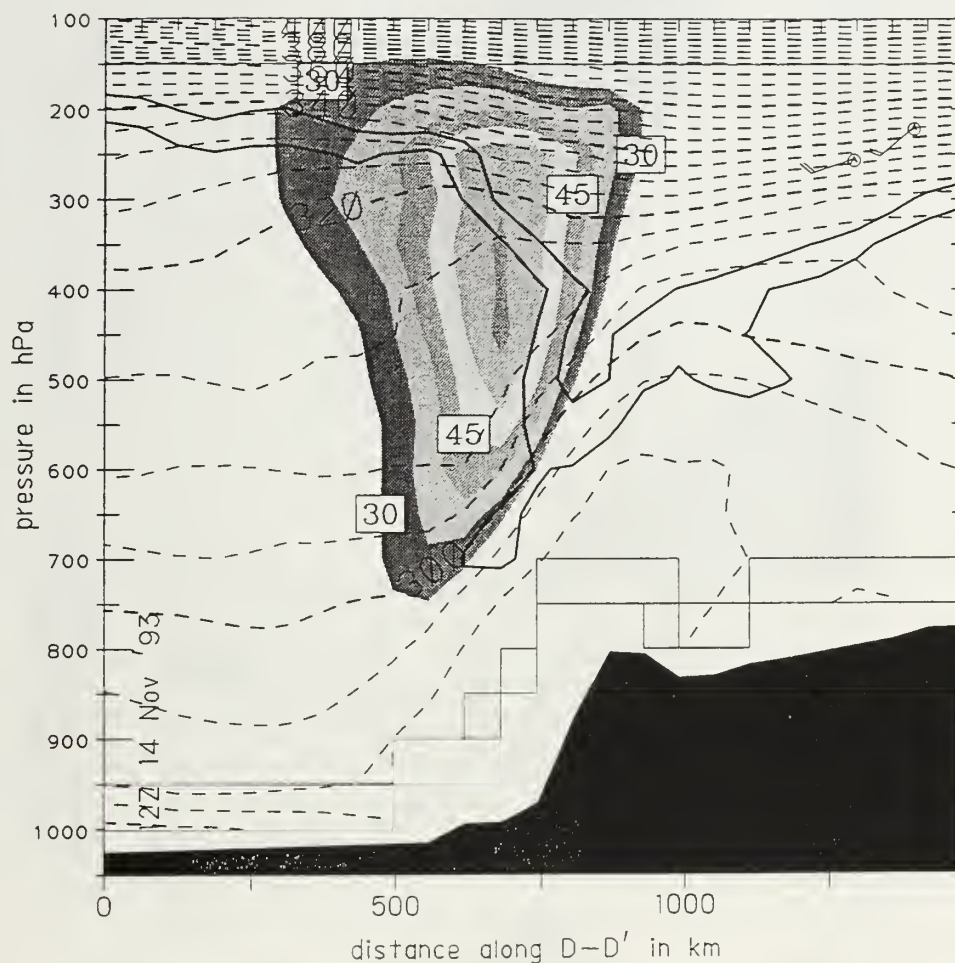


Figure 17. Cross-section valid at 1200 UTC 14 November 1993. Broken curves are potential temperature at a 5°K interval, shading is wind speed at a 5 m s^{-1} interval beginning with 30 m s^{-1} , and solid curves are potential vorticity. The upper solid curve is 3.0 PVU and the lower is 1.6 PVU . The cross-section starts at point D at the left edge and extends northeast to point D' at the right edge (Fig. 14). Winds are plotted as described in Fig. 9.

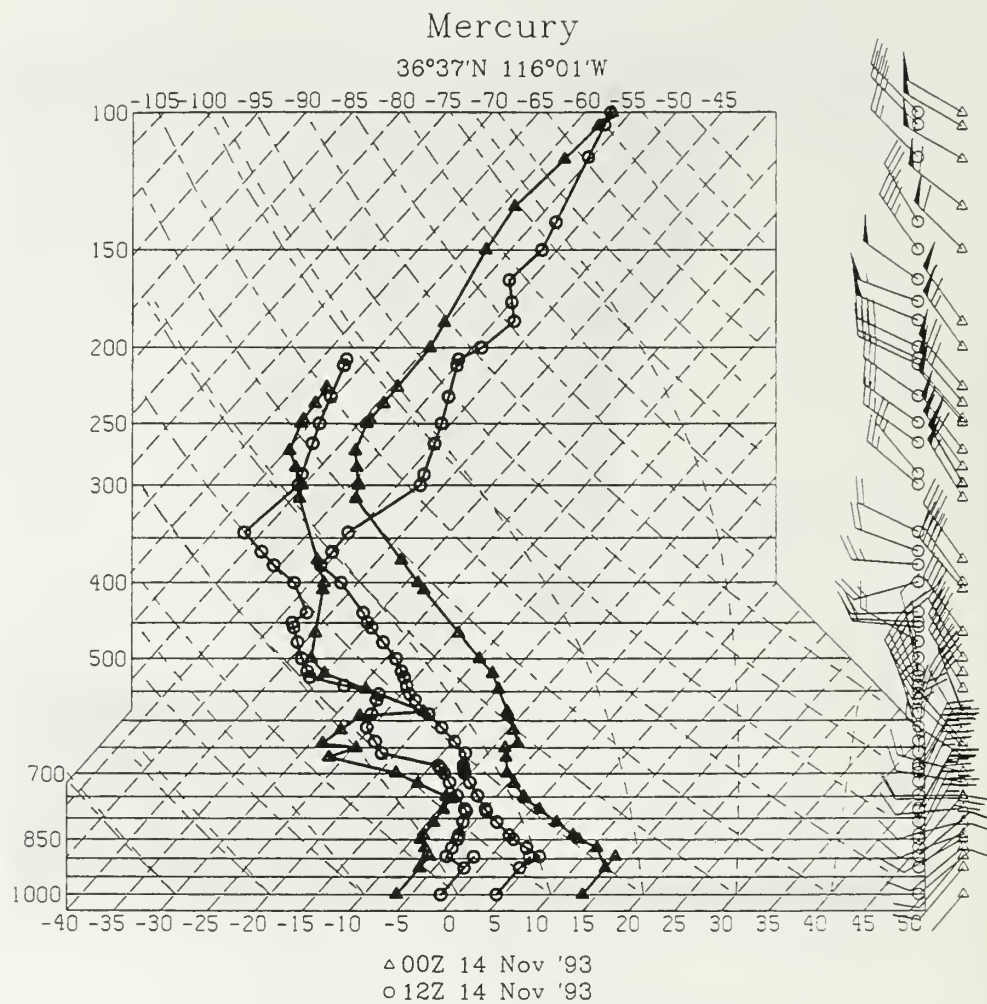


Figure 18. Sounding plotted on skew T diagram for Mercury (DRA). Triangles indicate 0000 UTC 14 November 1993 data and circles indicate 1200 UTC 14 November 1993 data.

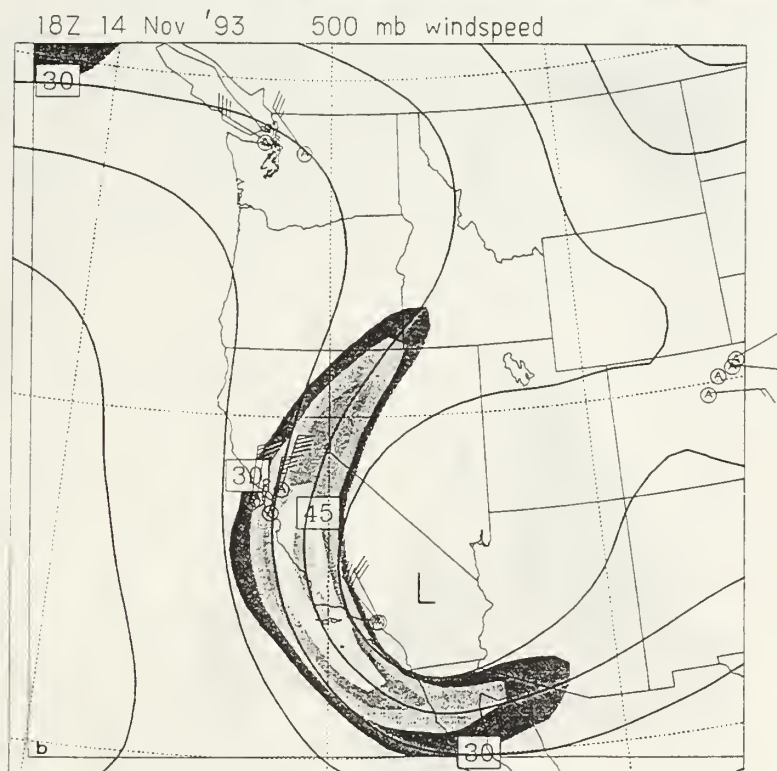


Figure 19. Same as Fig. 9 except for 1800 UTC 14 November 1993.

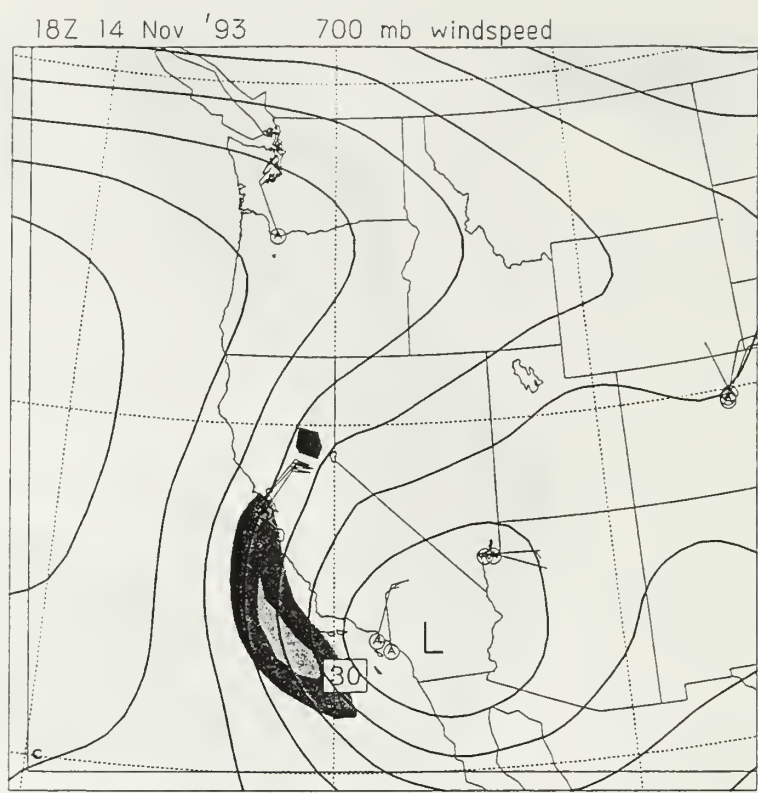


Figure 19. Continued.

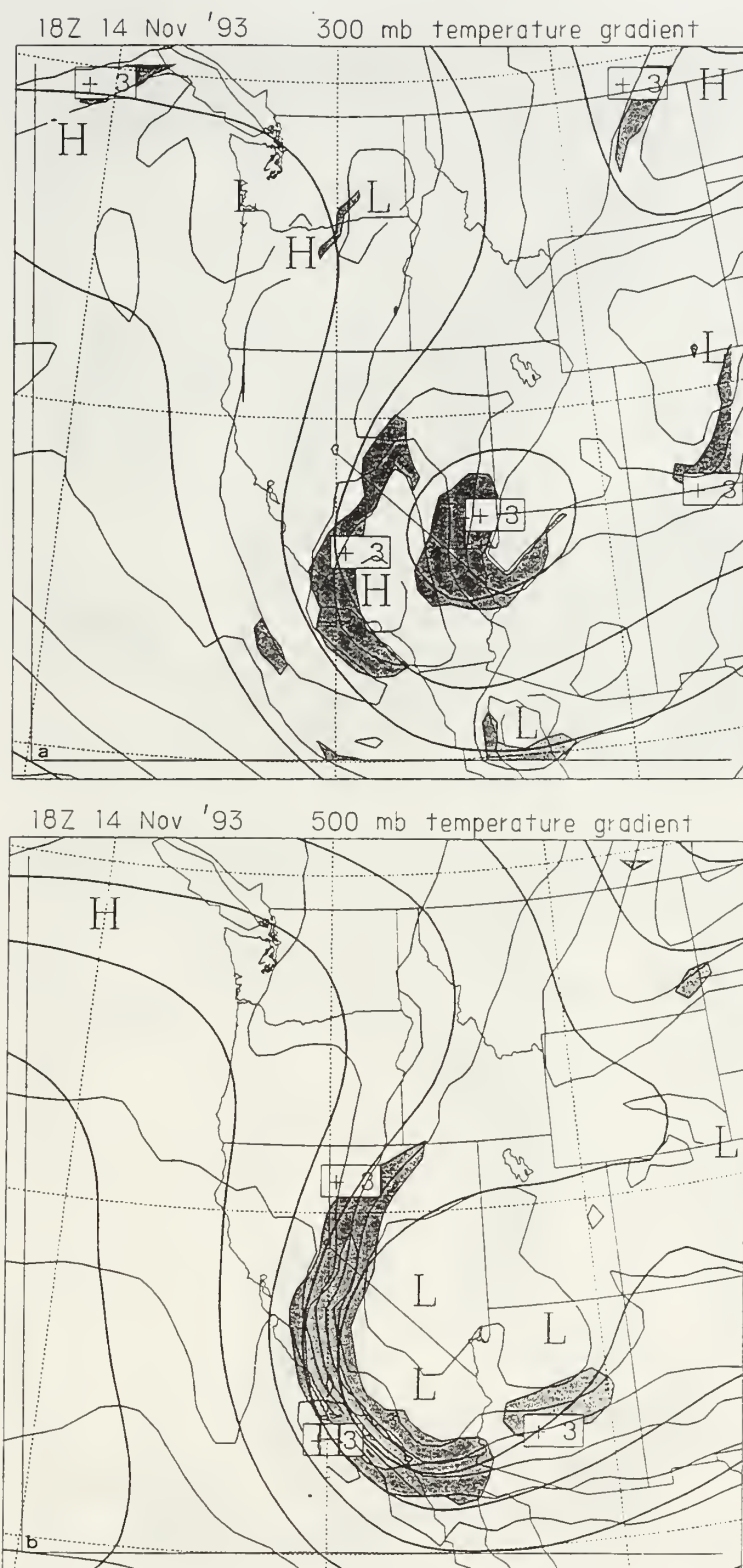


Figure 20. Same as Fig. 10 except for 1800 UTC 14 November 1993.

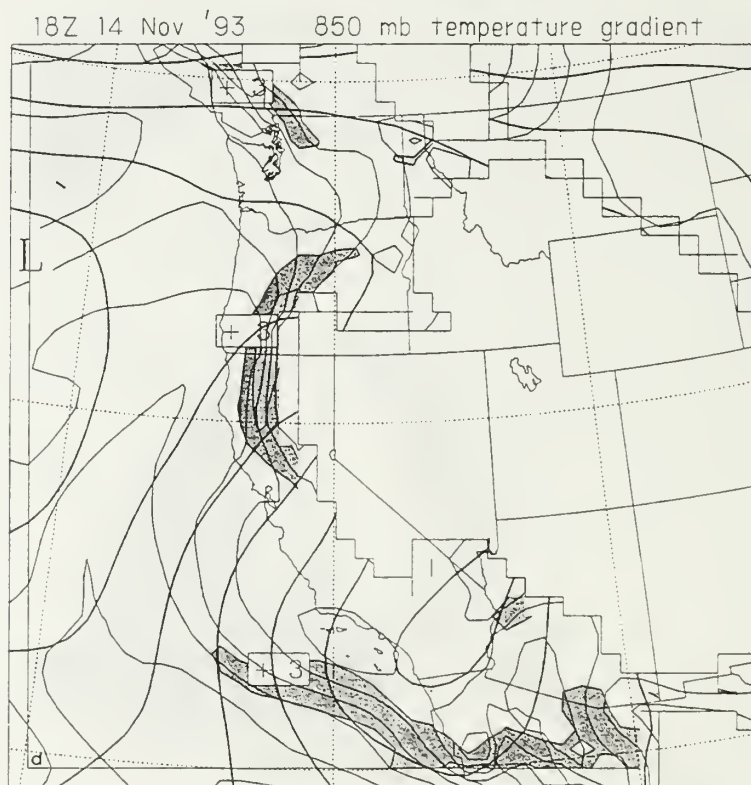
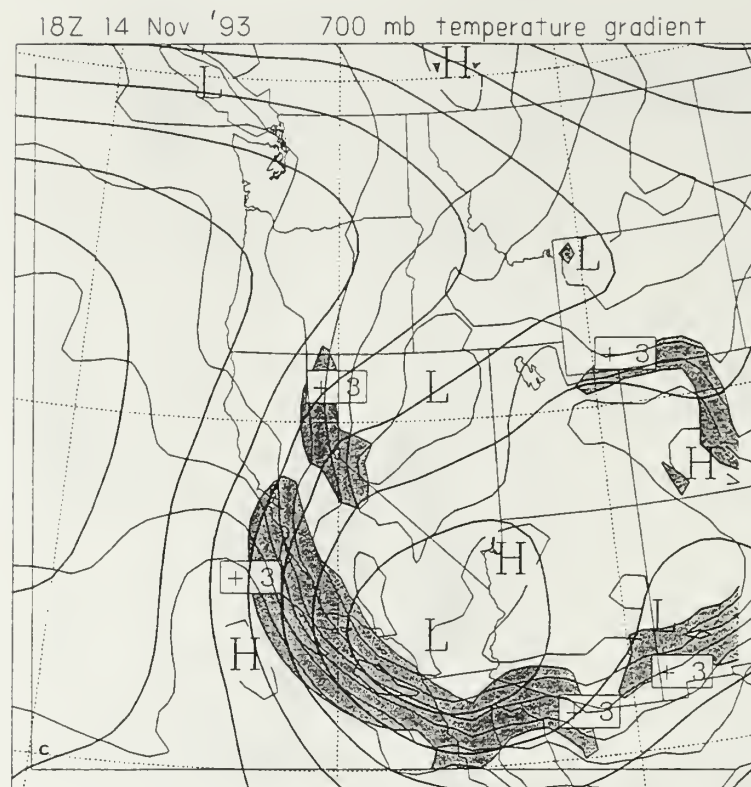


Figure 20. Continued.

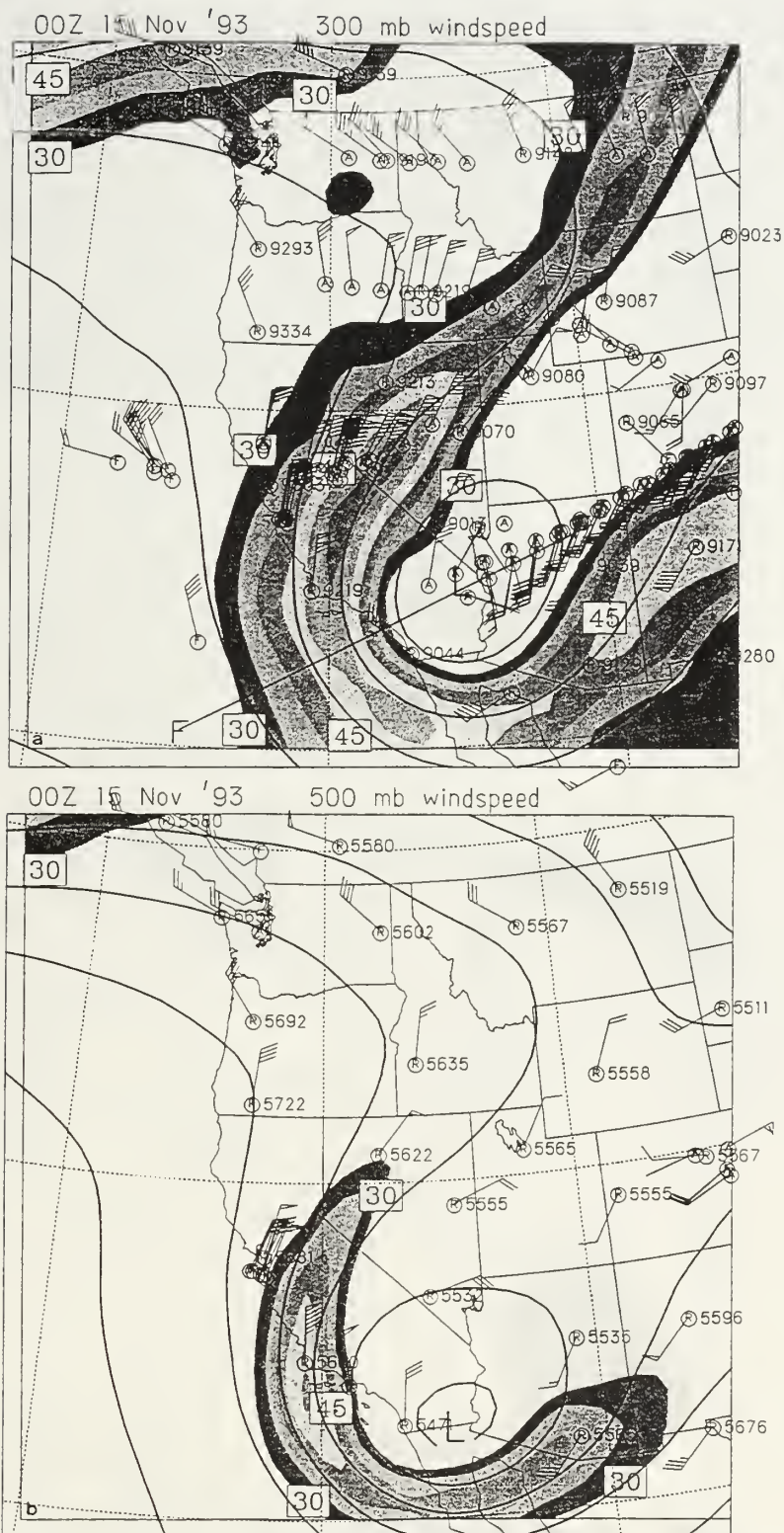


Figure 21. Same as Fig. 9 except for 0000 UTC 15 November 1993. Line F-F' indicates the location of the cross-section in Fig. 23.

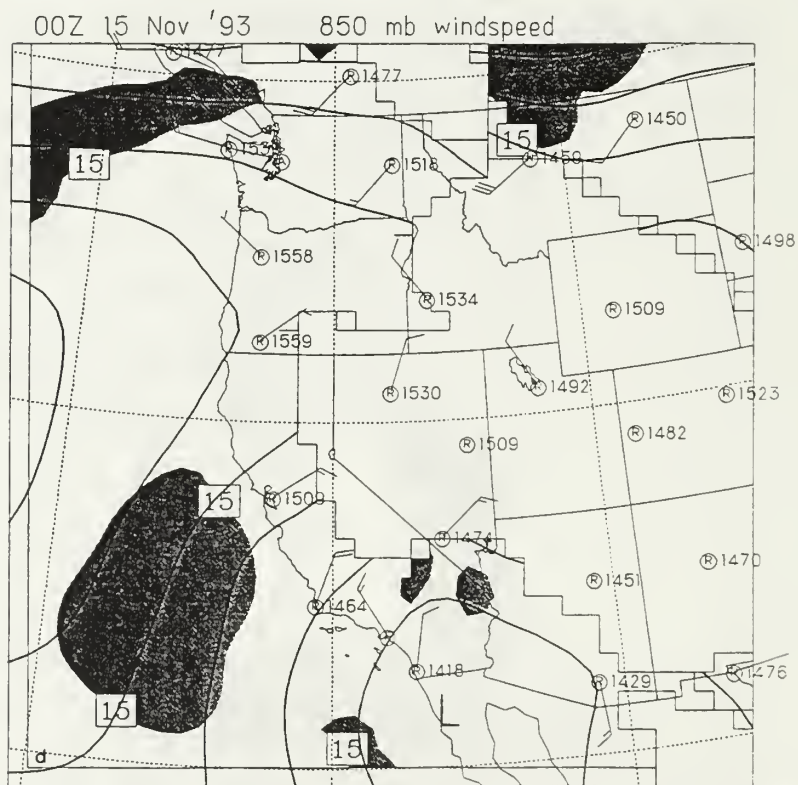
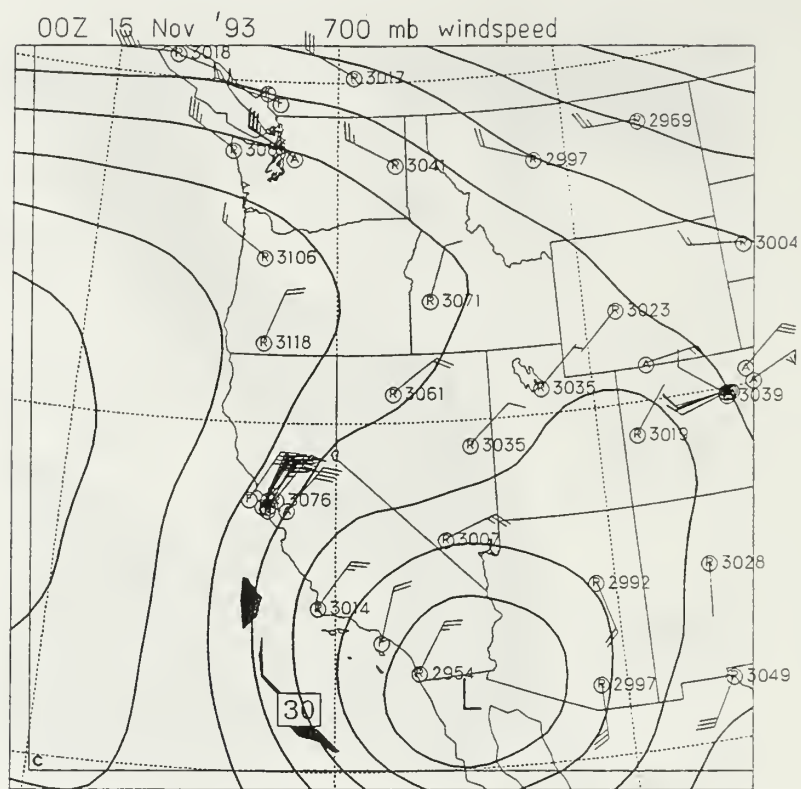


Figure 21. Continued.

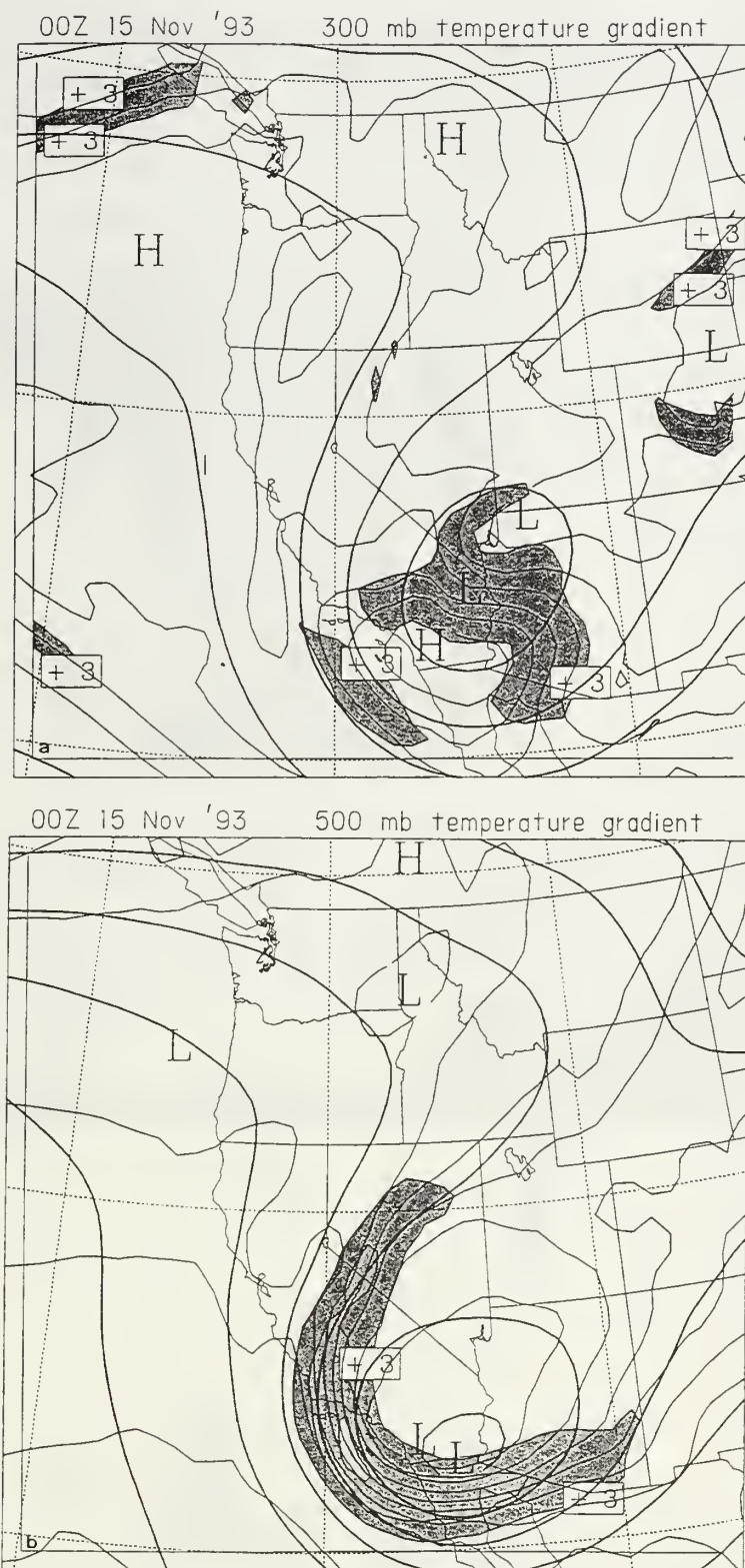


Figure 22. Same as Fig. 10 except for 0000 UTC 15 November 1993.

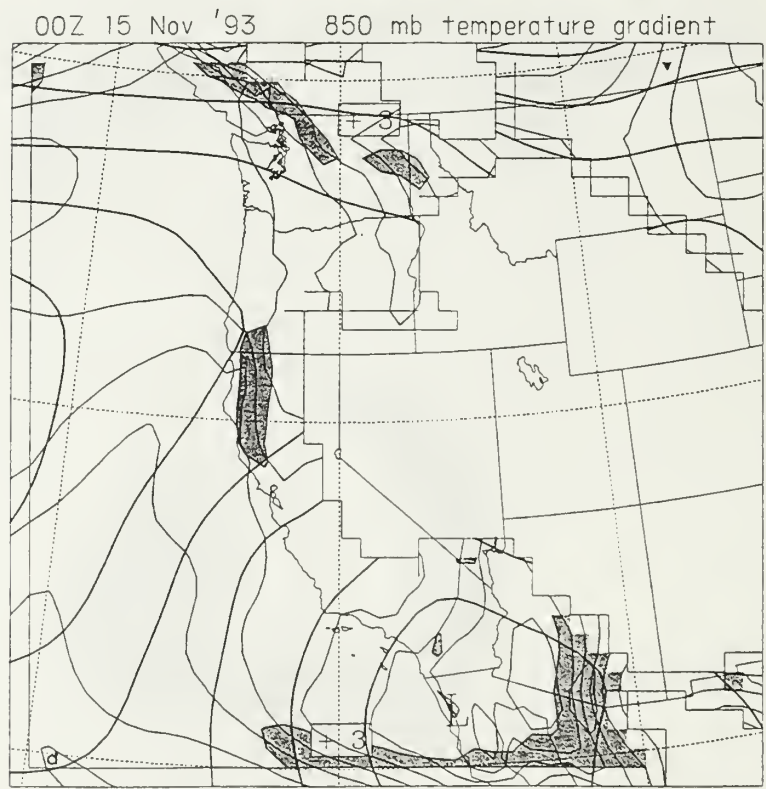
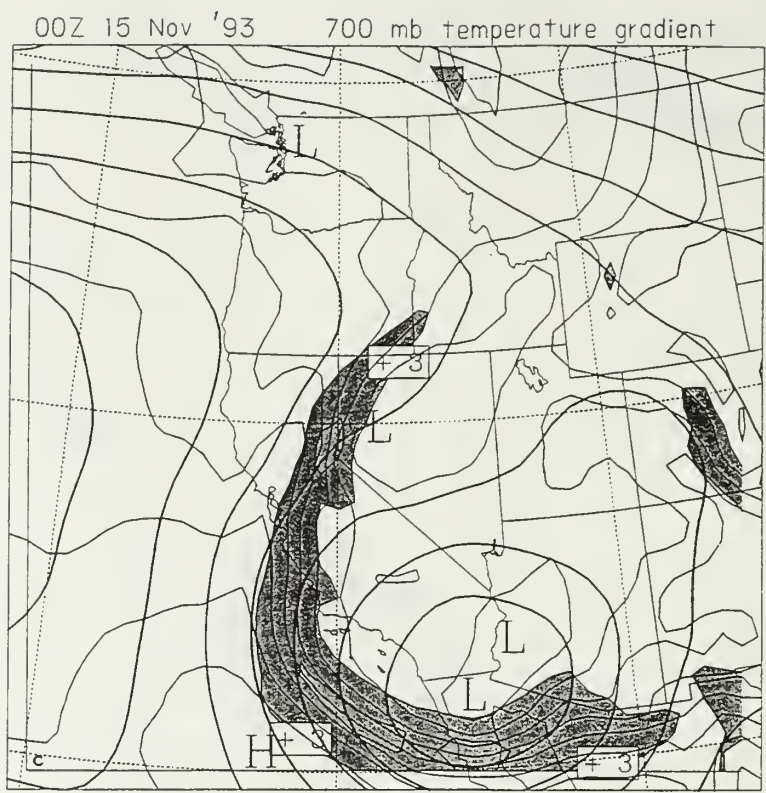


Figure 22. Continued.

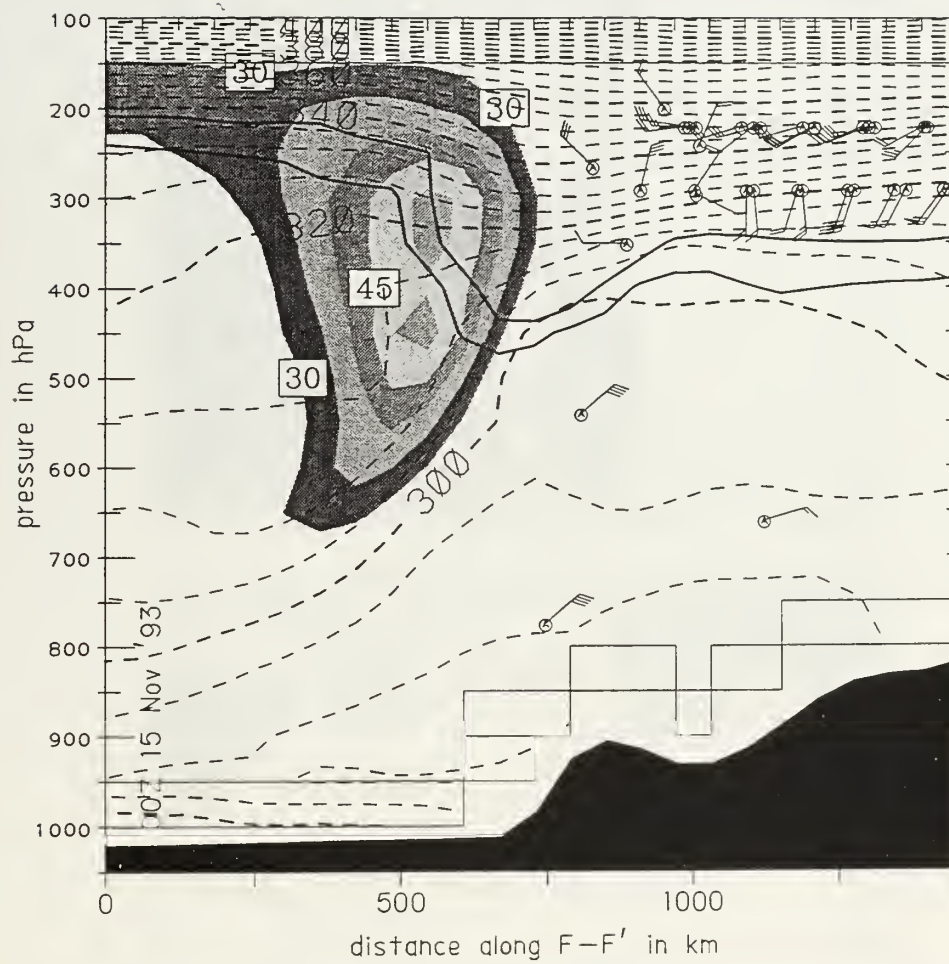


Figure 23. Same as Fig. 17 except for line F-F'(see Fig. 21) valid at 0000 UTC 15 November 1993.

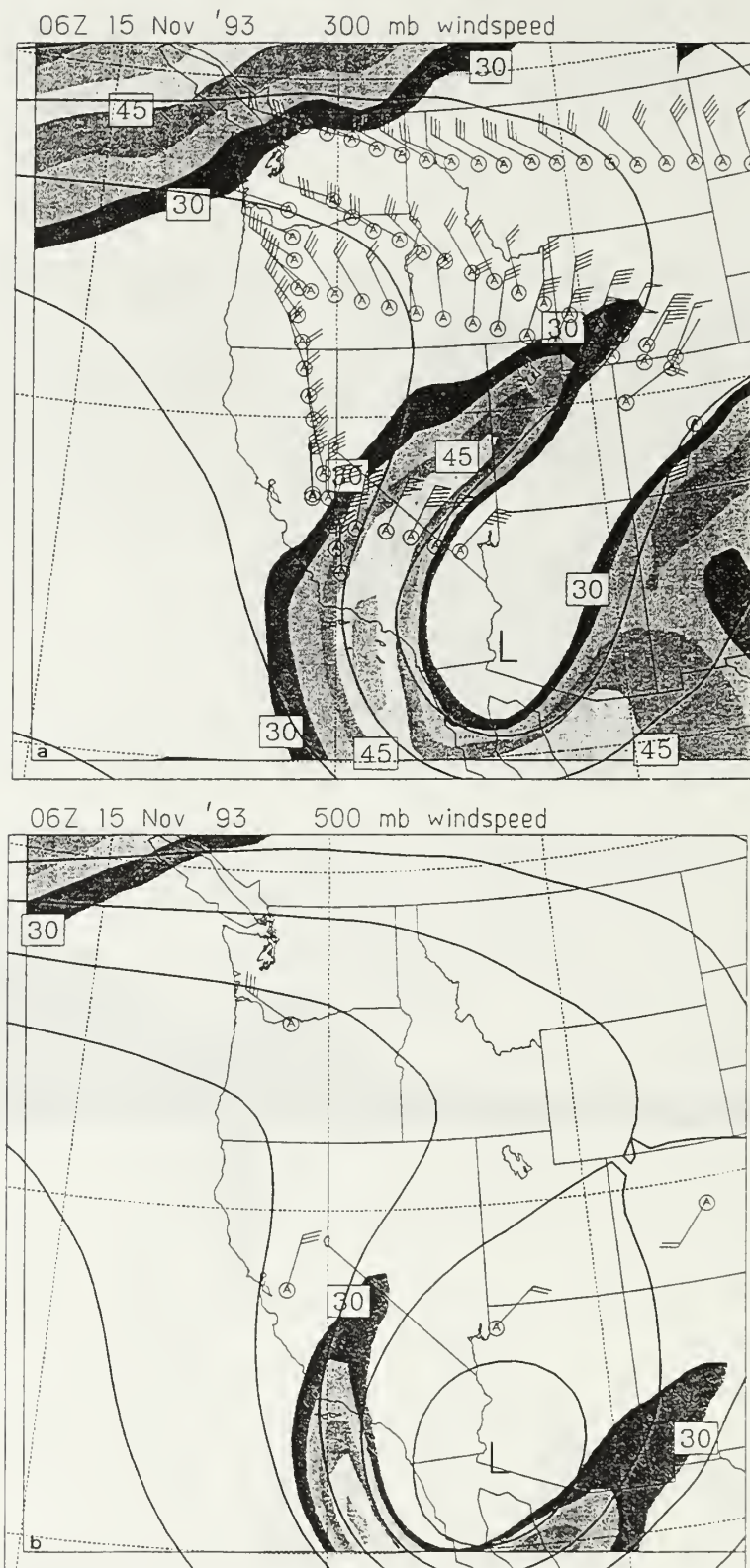


Figure 24. Same as Fig. 9 except for 0600 UTC 15 November 1993.

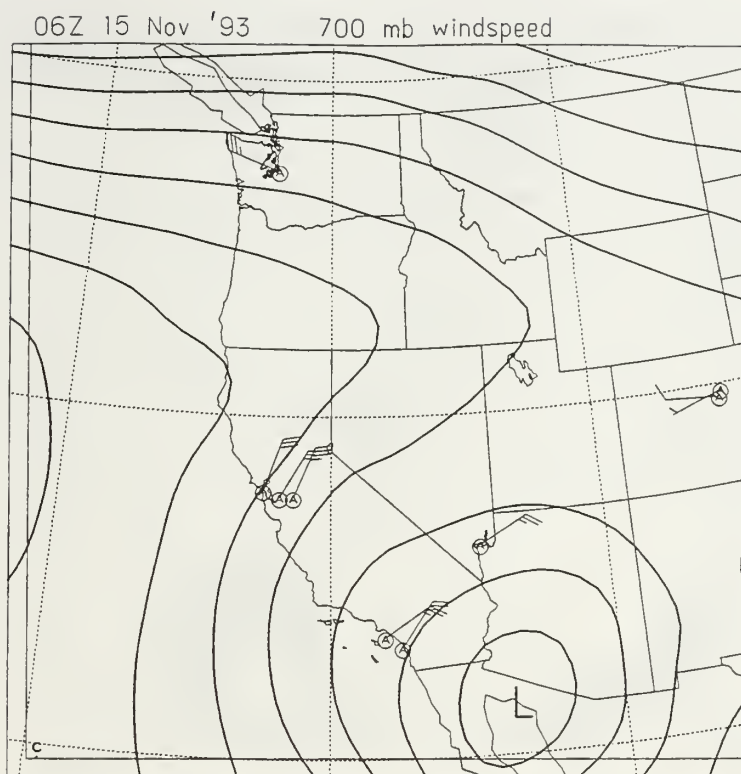


Figure 24. Continued.



Figure 25. Same as Fig. 10 except for 0600 UTC 15 November 1993.

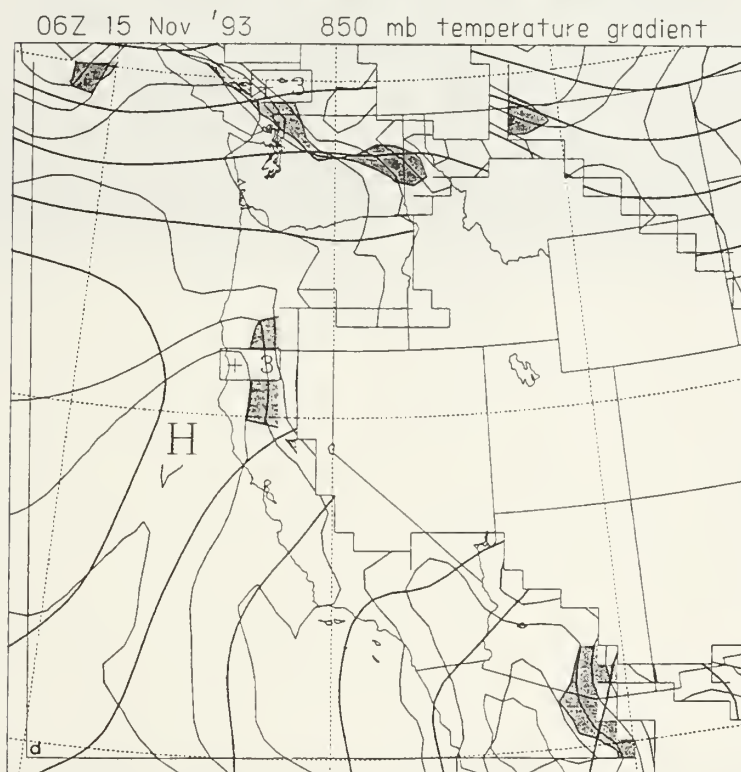
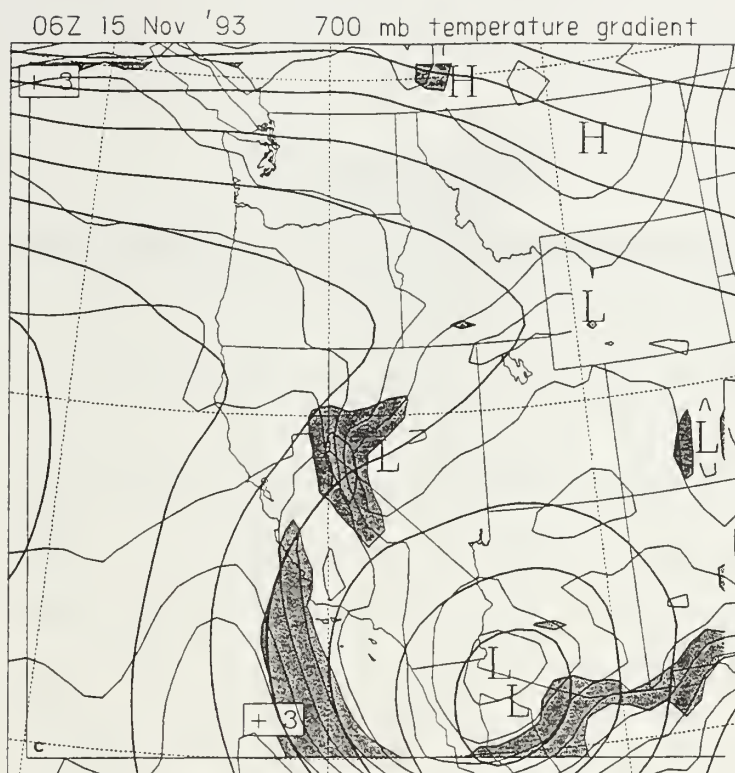


Figure 25. Continued.

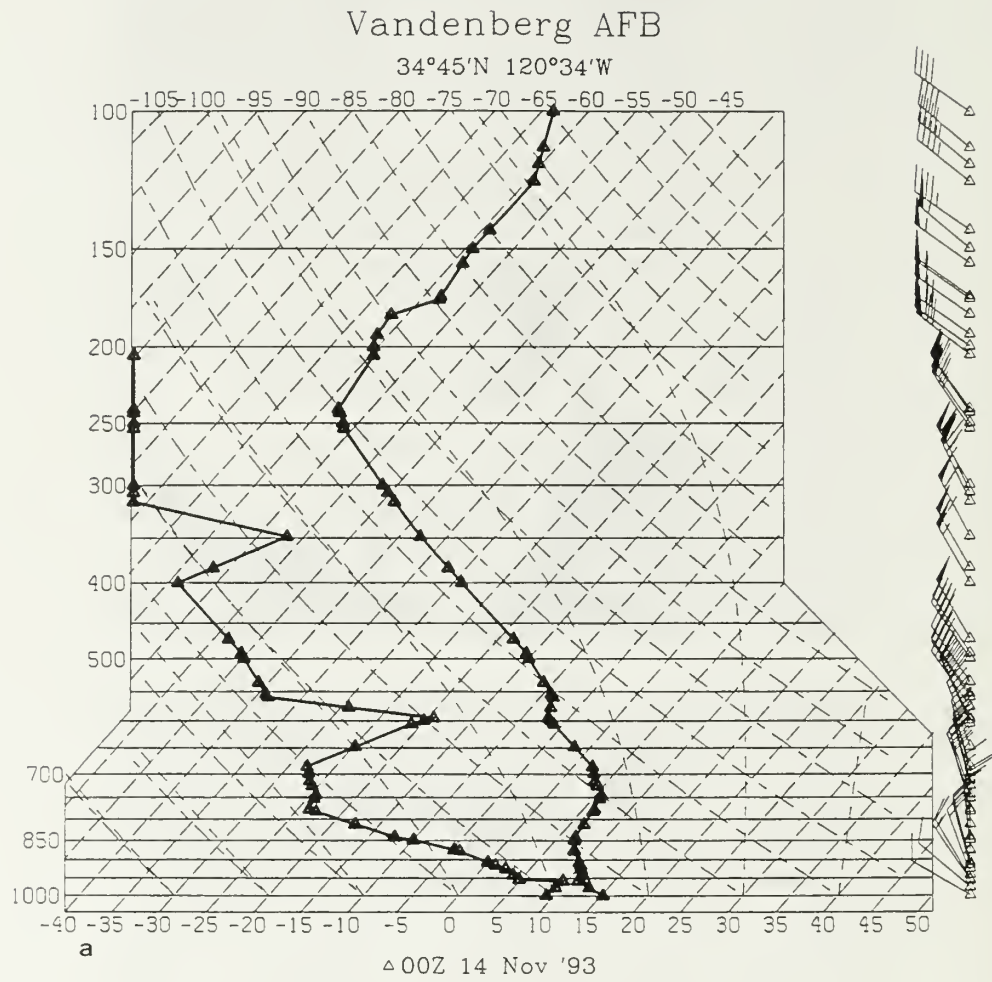


Figure 26. Sounding for Vandenberg Air Force Base taken at (a) 0000 UTC 14 November, (b) 1200 UTC 14 November, (c) 0000 UTC 15 November, (d) 1200 UTC 15 November.

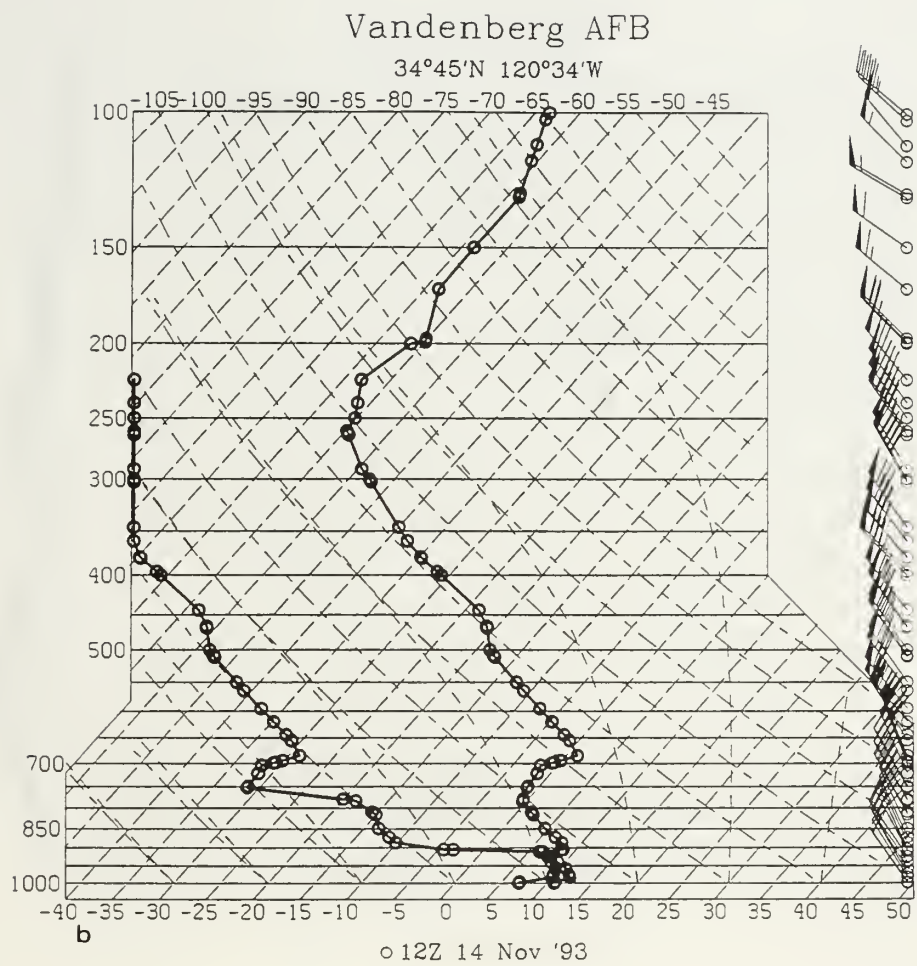


Figure 26. Continued.

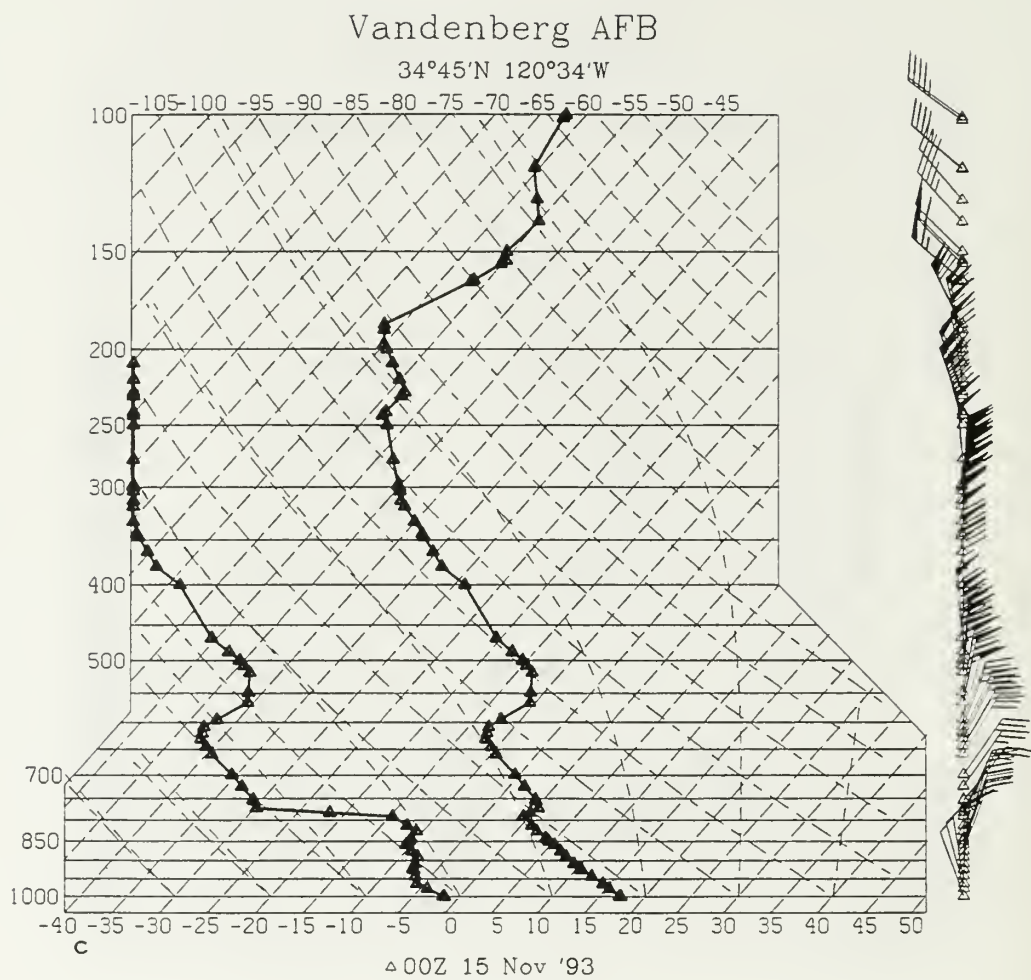


Figure 26. Continued.

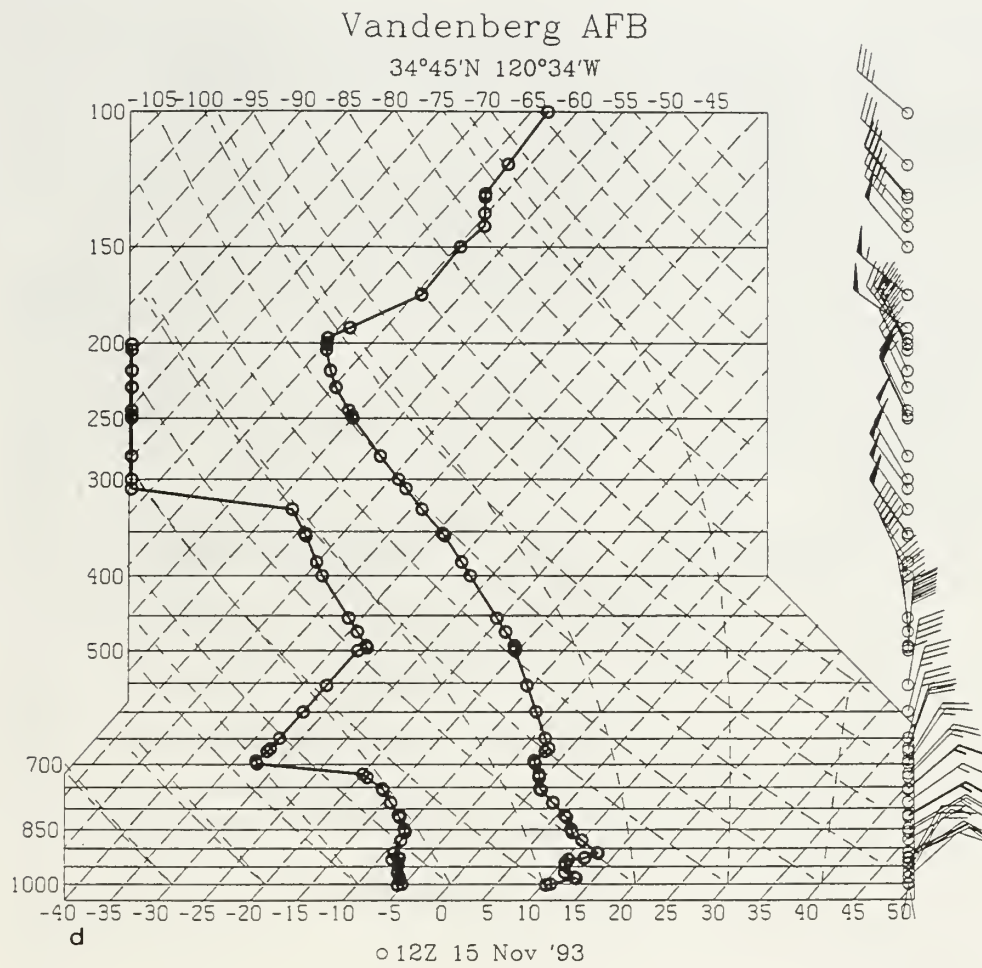


Figure 26. Continued.

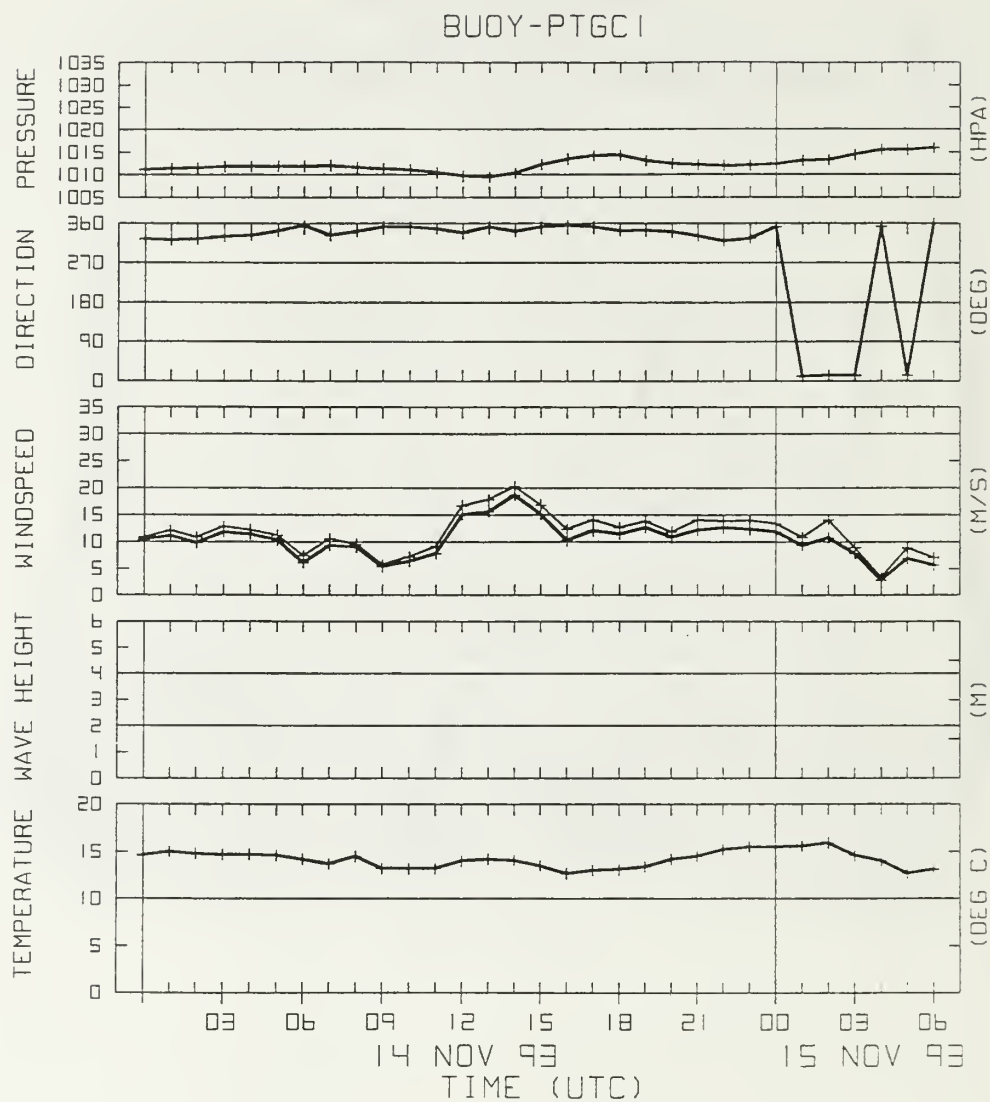


Figure 27. Meteorogram for station PTGC1. Values plotted include sea level pressure (hPa), wind direction (degrees from true north), wind speed (m s^{-1}) (thick line), wind gust (m s^{-1}) (thin line), significant wave height (m), and air temperature ($^{\circ}\text{C}$) (solid line).

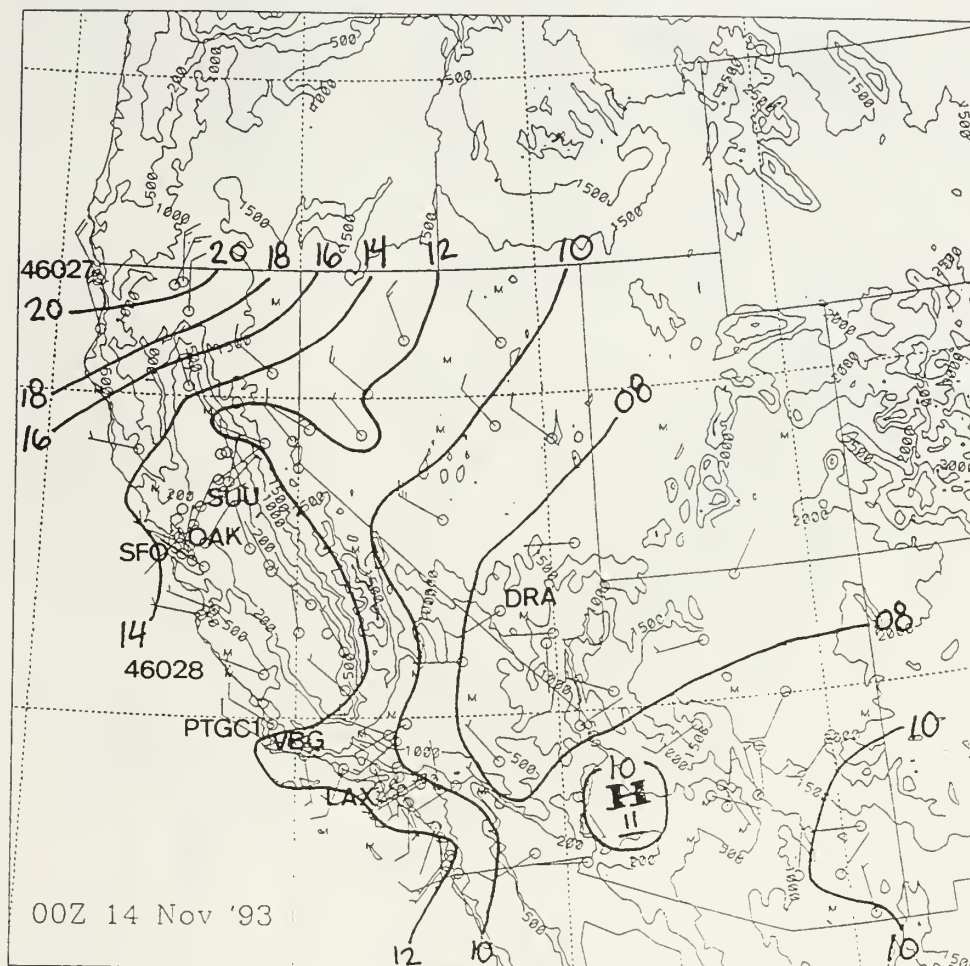


Figure 28. Manual analysis of sea-level pressure valid at 0000 UTC 14 November 1993. Isobars are drawn every 2 hPa and labeled with the last two digits of the value, and winds are plotted as in Fig. 9. An “M” denotes a missing observation and a circle with no barb indicates that winds are calm. SUU is Travis Air Force Base, SFO is San Francisco, LAX is Los Angeles, OAK is Oakland, VBG is Vandenberg, DRA is Mercury. 46027 and 46028 are buoys and PTGC1 is an automated coastal station.

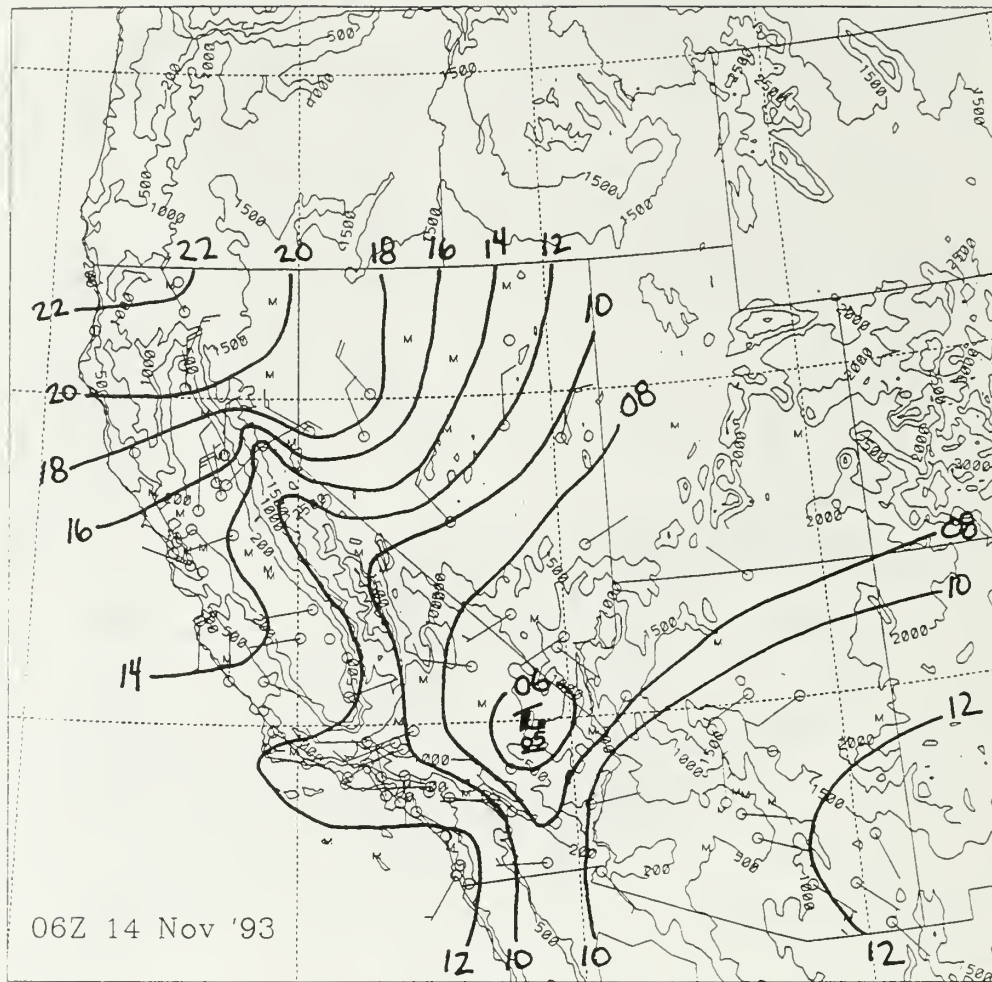


Figure 29. Same as Fig. 28 except for 0600 UTC 14 November 1993.

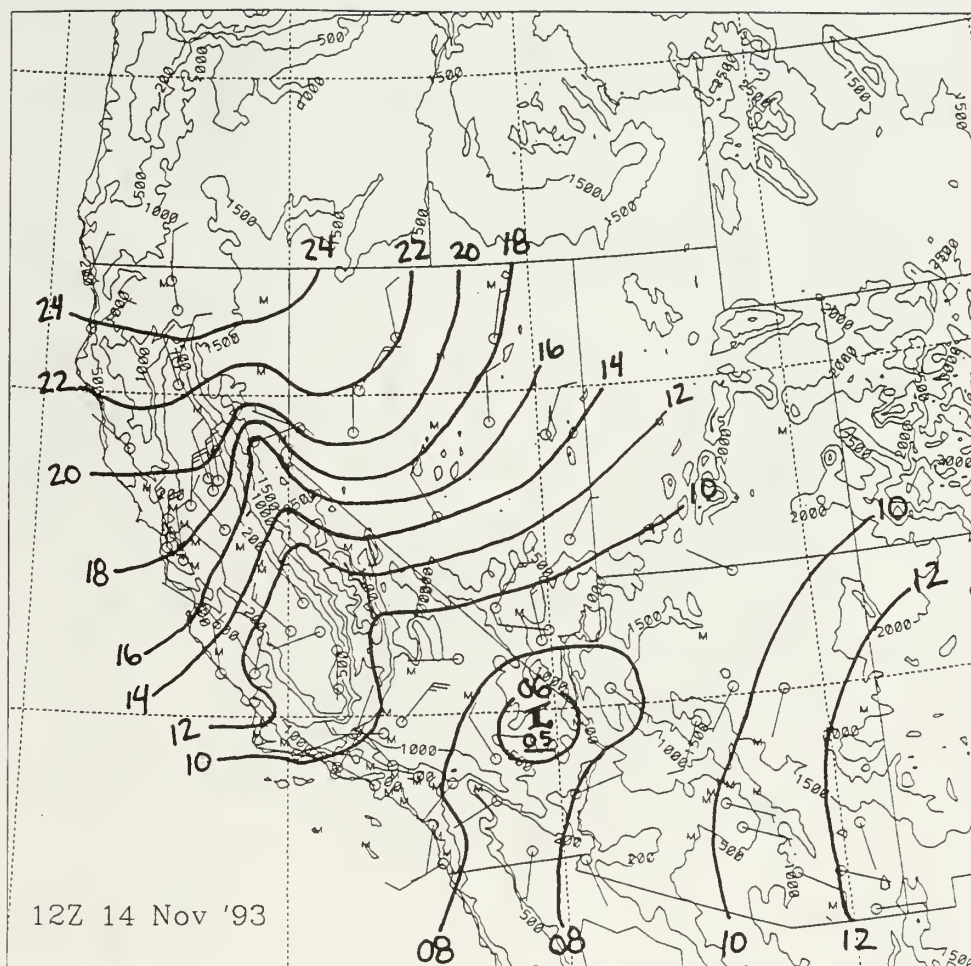


Figure 30. Same as Fig. 28 except for 1200 UTC 14 November 1993.

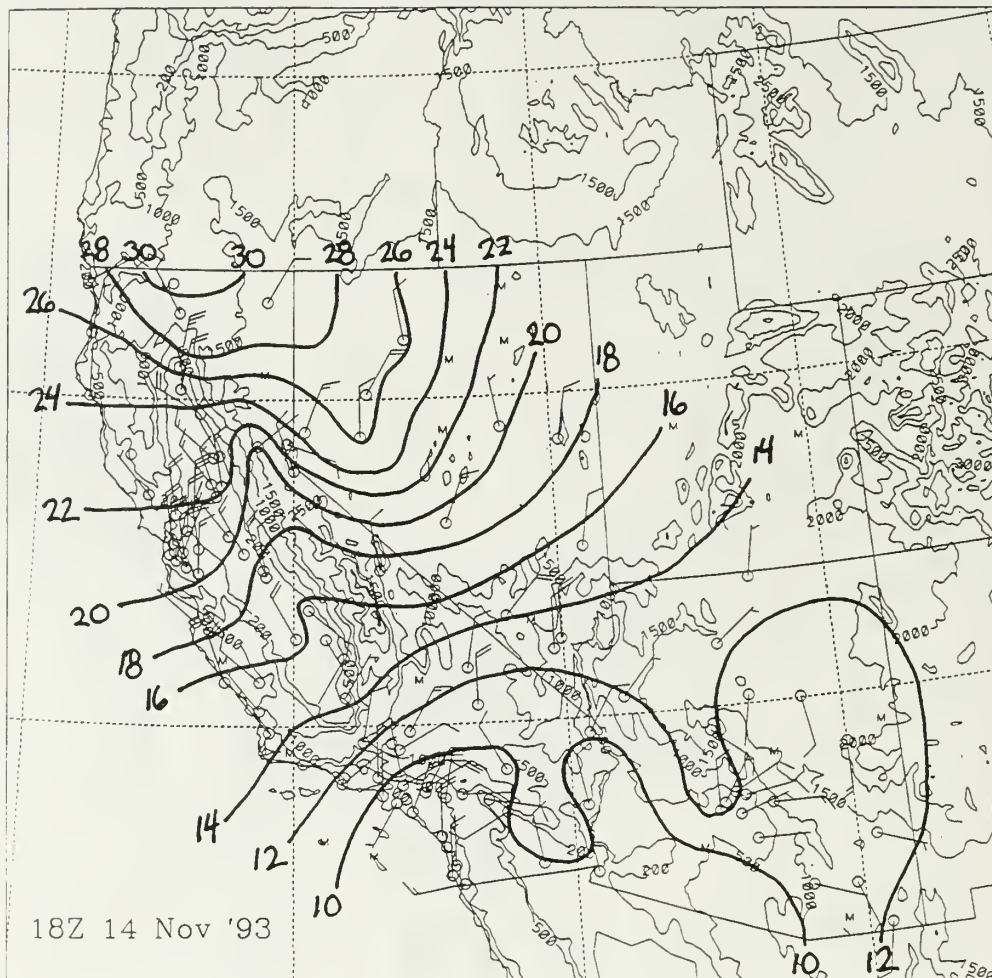


Figure 31. Same as Fig. 28 except for 1800 UTC 14 November 1993.

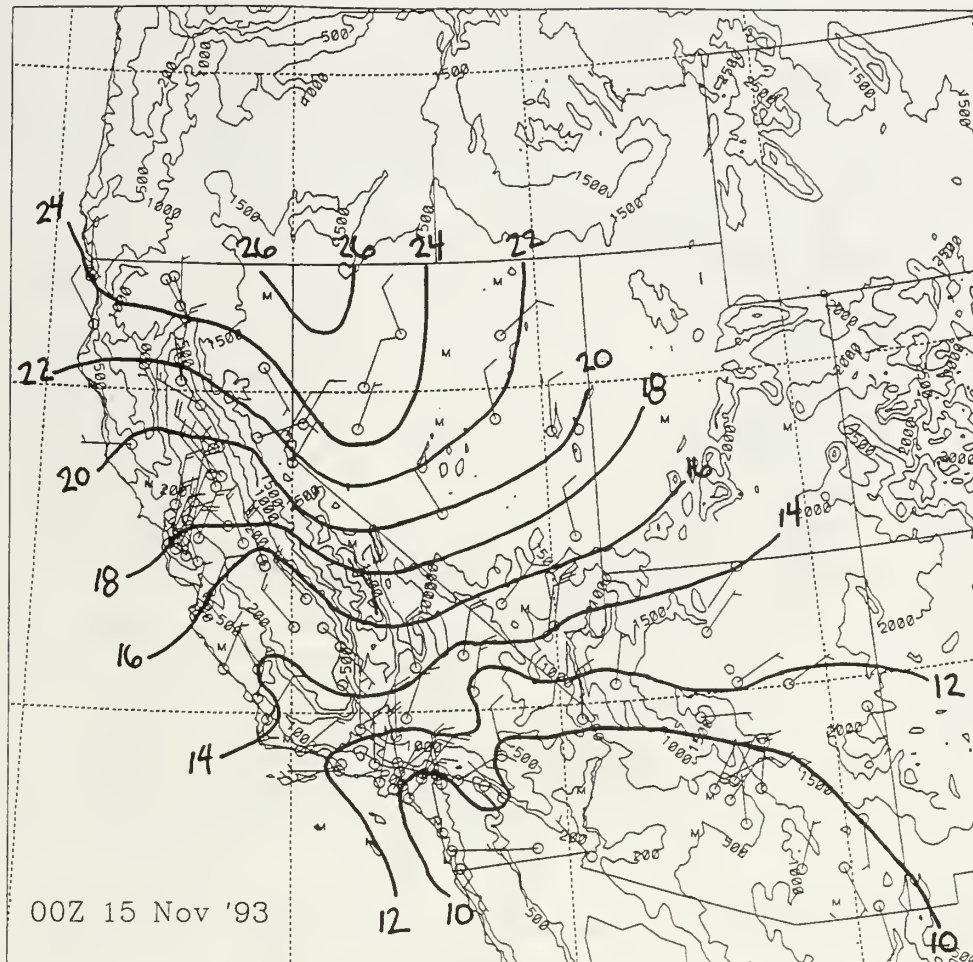


Figure 32. Same as Fig. 28 except for 0000 UTC 15 November 1993.

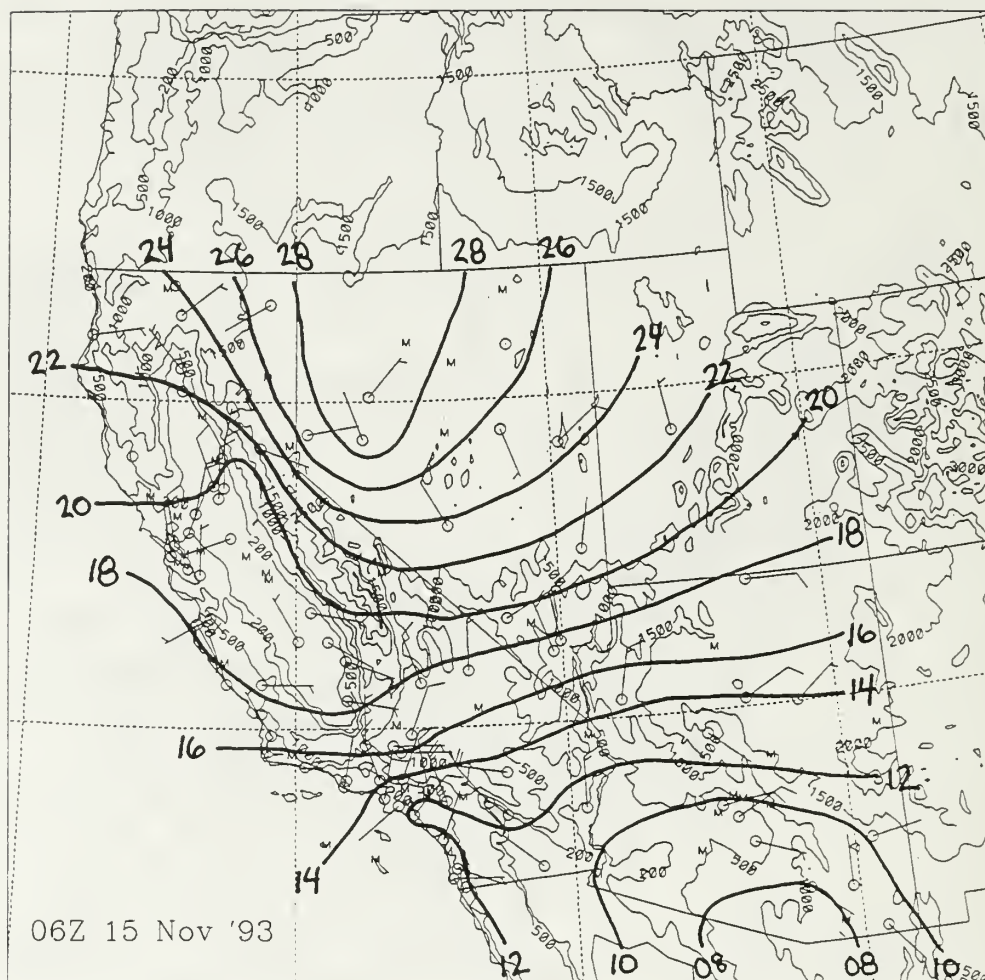


Figure 33. Same as Fig. 28 except for 0600 UTC 15 November 1993.

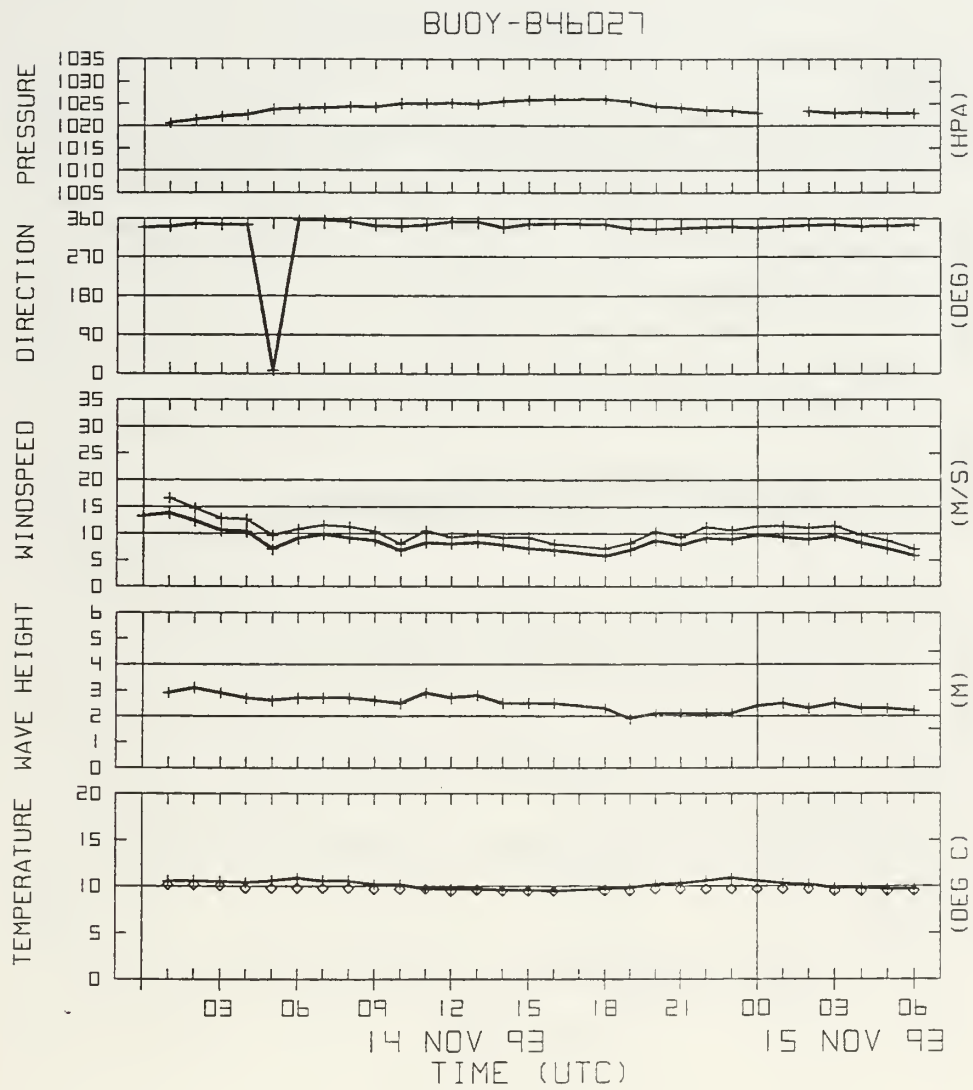


Figure 34. Meteorogram for Buoy 46027. Values plotted are the same as in Fig. 27 except for sea surface temperature ($^{\circ}\text{C}$) (diamonds).

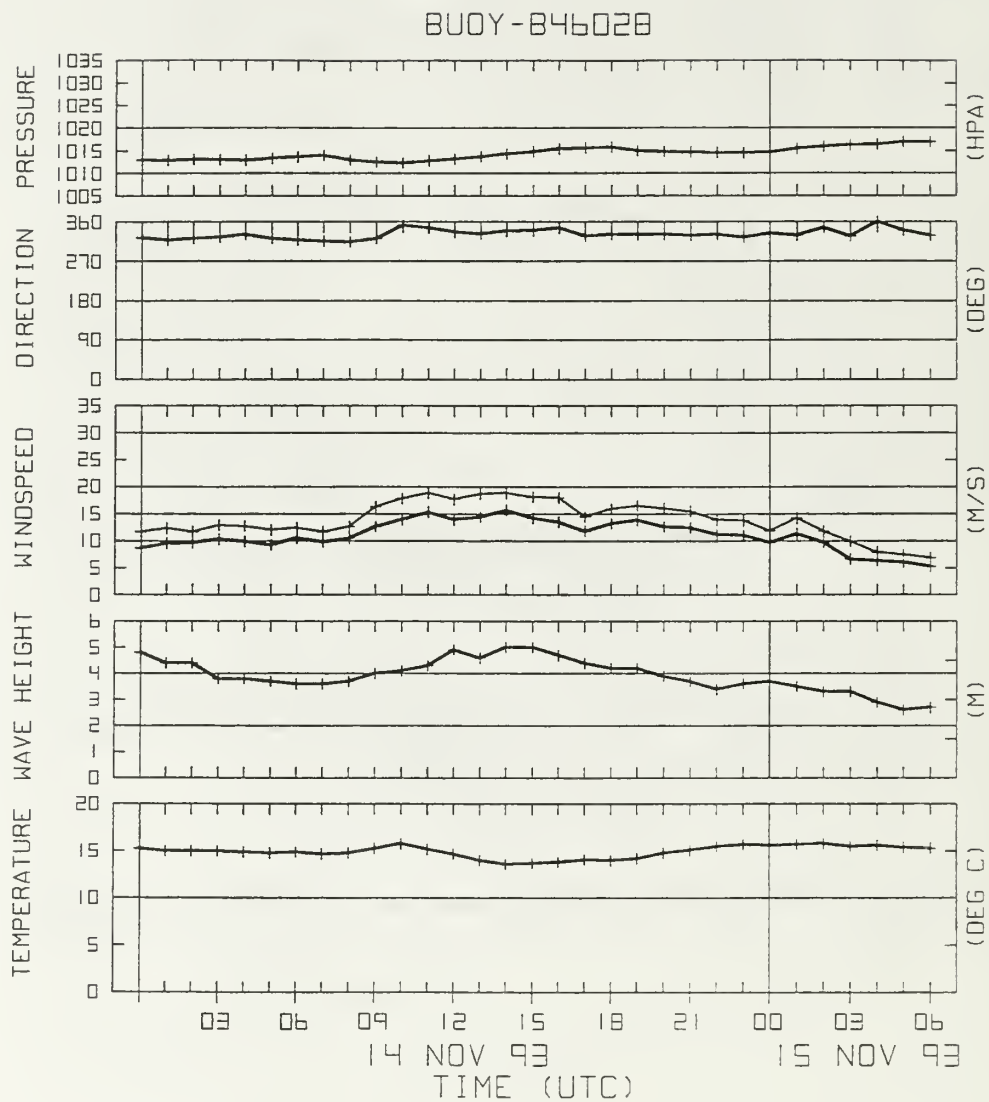


Figure 35. Meteorogram for Buoy 46028. Values plotted are the same as for Fig. 27 except for sea surface temperature ($^{\circ}\text{C}$) (diamonds).

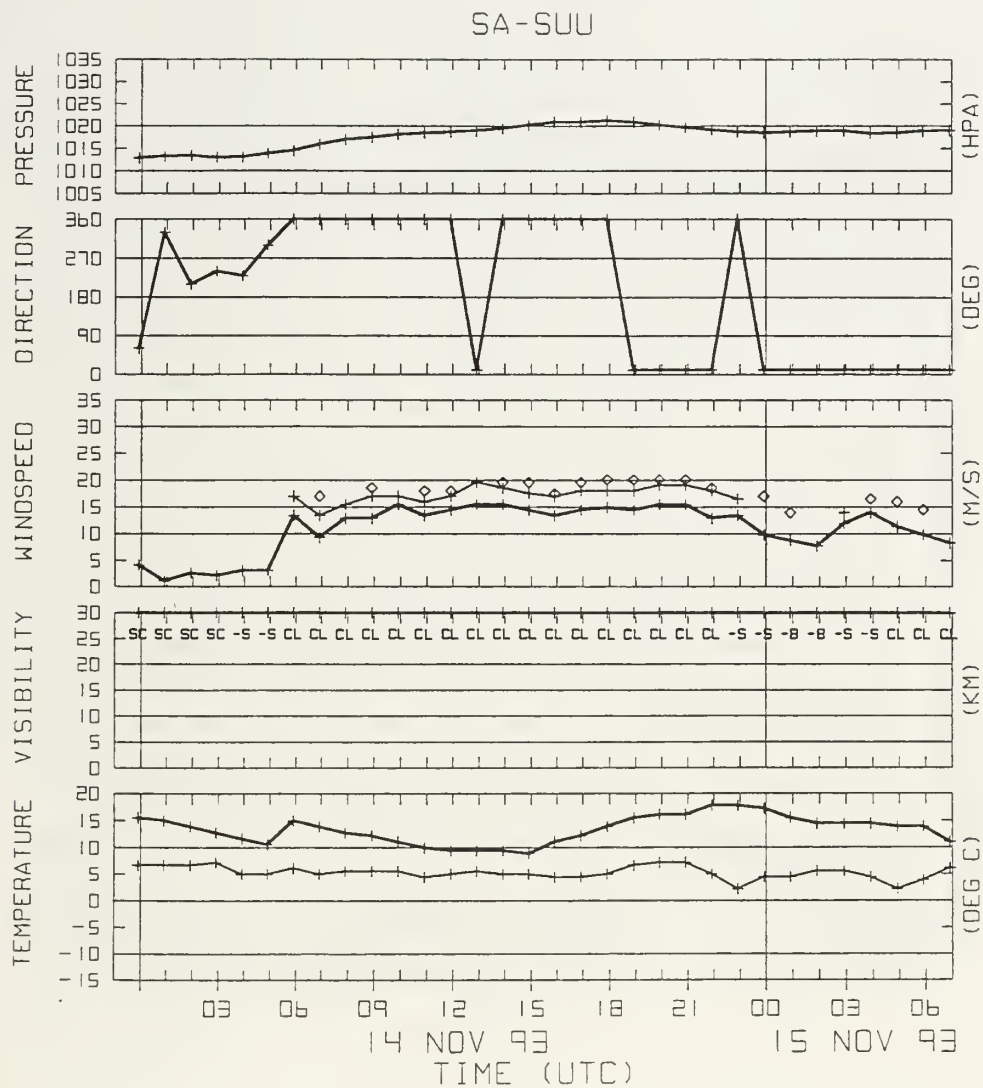


Figure 36. Meteorogram for Travis Air Force Base (SUU). Values plotted are surface pressure (hPa), wind direction (degrees from true north), wind speed (m s^{-1}) (thick line), wind gust (m s^{-1}) (thin line), peak wind (m s^{-1}) (diamonds), visibility (km), sky cover and observed weather (top two lines of visibility plot respectively), surface temperature ($^{\circ}\text{C}$), and dew point temperature ($^{\circ}\text{C}$) (thin line).

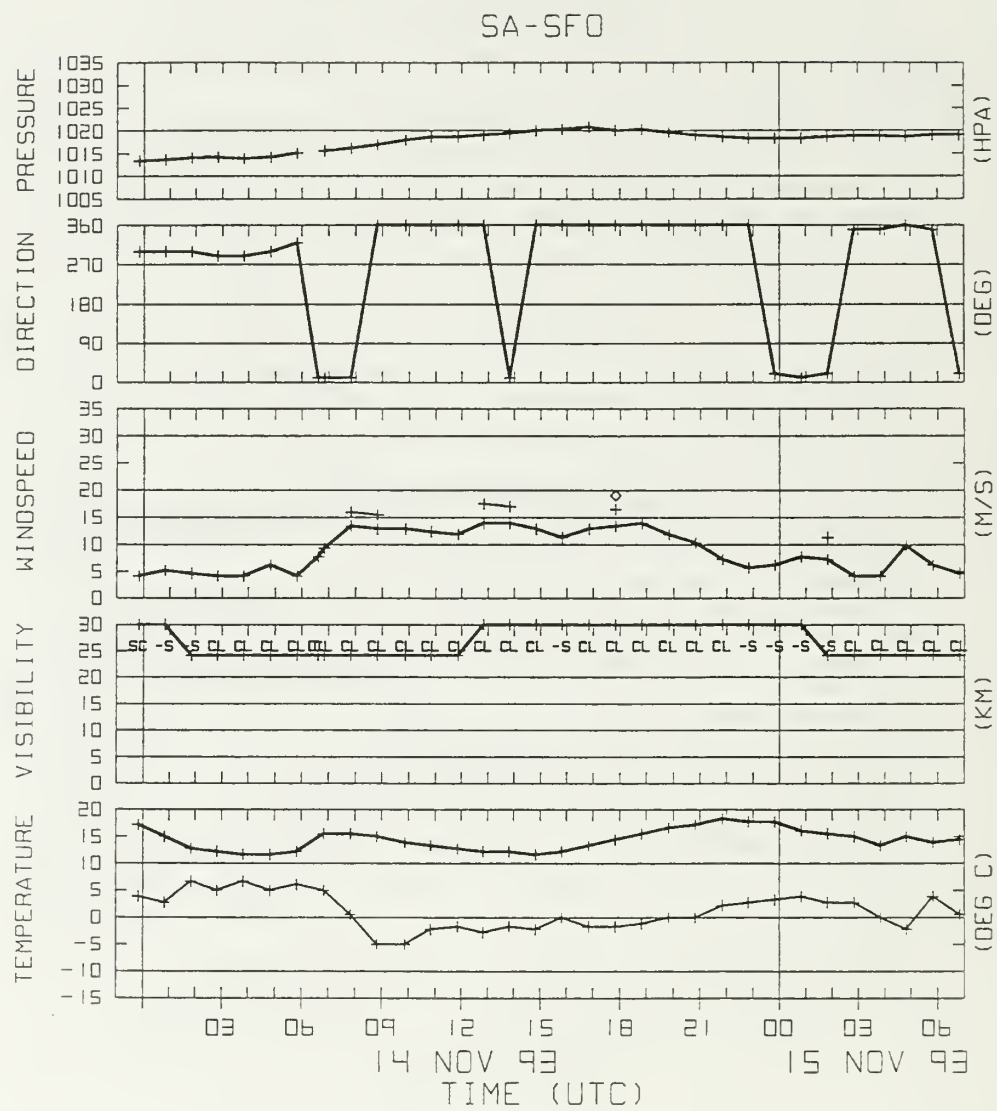


Figure 37. Same as Fig. 36 except for San Francisco (SFO).

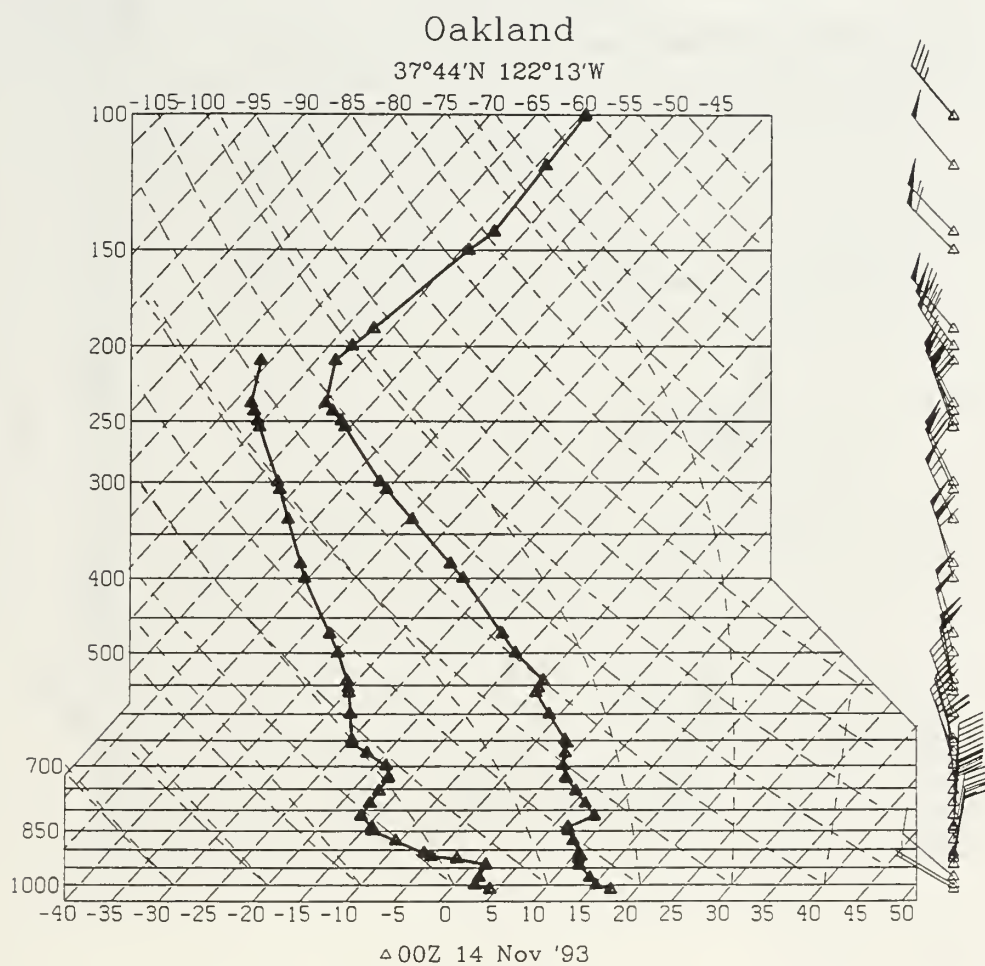


Figure 38. Sounding for Oakland taken at 0000 UTC 14 November.

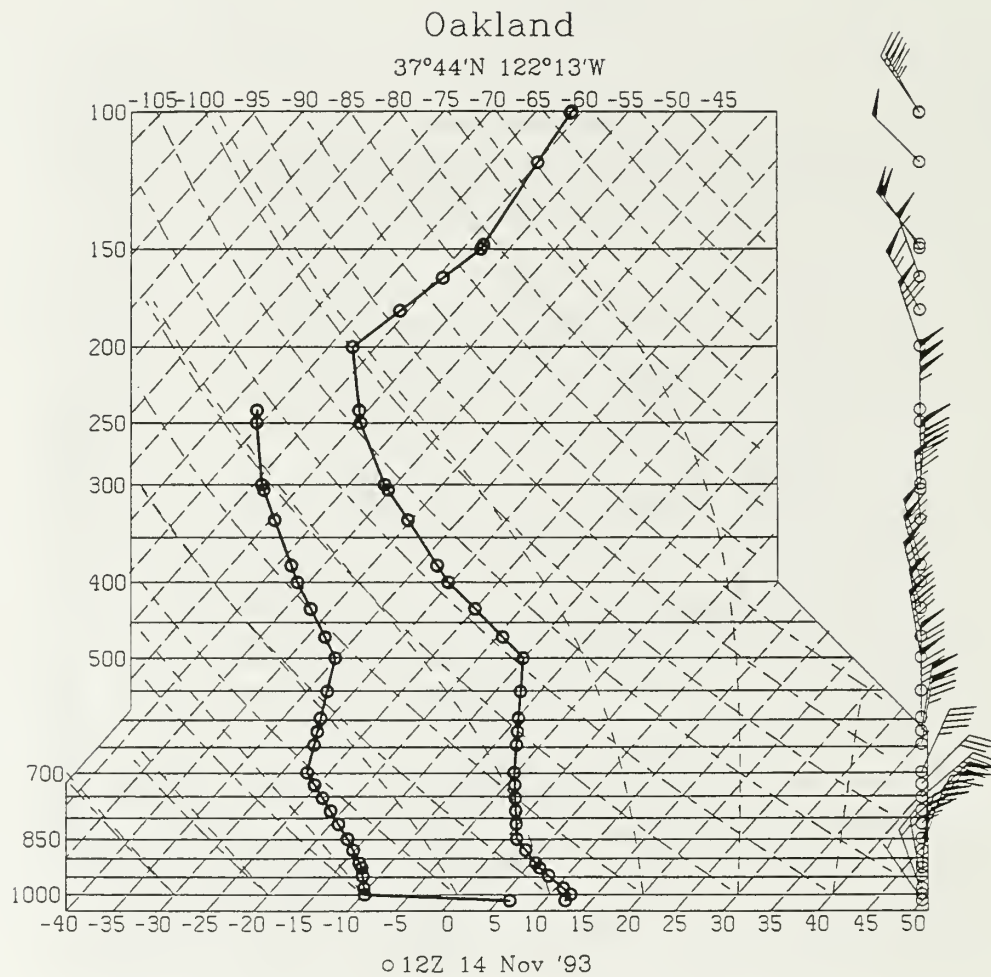


Figure 39. Same as Fig. 38 except for 1200 UTC 14 November.

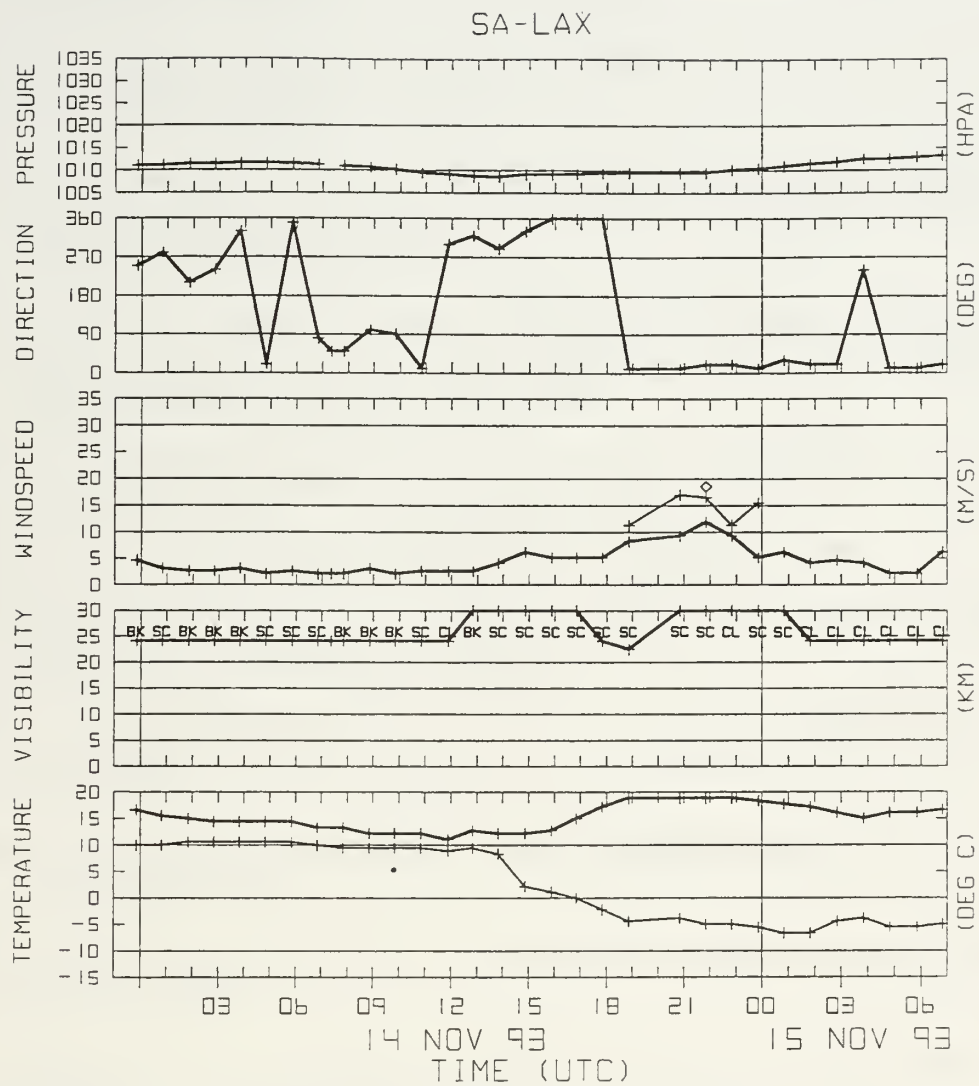


Figure 40. Same as Fig. 36 except for Los Angeles (LAX).

LIST OF REFERENCES

- Baker, N. L., 1992: Quality control for the Navy operational atmospheric database. *Wea. Forecasting*, **7**, 250-261.
- Barker, E. H., 1992: Design of the Navy's multivariate optimum interpolation analysis system. *Wea. Forecasting*, **7**, 220-231.
- Benjamin, S. G., and P. A. Miller, 1990: An alternative sea level pressure reduction and a statistical comparison of geostrophic wind estimates with observed surface winds. *Mon. Wea. Rev.*, **118**, 2099-2116.
- , K. A. Brewster, R. Brümmer, B. F. Jewett, T. W. Schlatter, T. L. Smith, and P. A. Stamus, 1991: An isentropic three-hourly data assimilation system using ACARS aircraft observations. *Mon. Wea. Rev.*, **119**, 888-906.
- Byers, H. R., 1974: *General Meteorology*, 4th ed., McGraw-Hill, 461 pp.
- Carlson, T. N., 1991: *Mid-Latitude Weather Systems*, Routledge, 507 pp.
- Danard, M., 1989: On computing the surface horizontal pressure gradient over elevated terrain. *Mon. Wea. Rev.*, **117**, 1344-1350.
- Fujita, T. T., 1989: The Teton-Yellowstone tornado of 21 July 1987. *Mon. Wea. Rev.*, **117**, 1913-1940.
- Gerber, H., S. Chang, and T. Holt, 1989: Evolution of a marine boundary-layer jet. *J. Atmos. Sci.*, **46**, 1312-1326.
- Hodur, R. M., 1987: Evaluation of a regional model with an update cycle. *Mon. Wea. Rev.*, **115**, 2707-2718.
- Holton, James R., 1992: *An Introduction to Dynamic Meteorology*, 3rd ed., Academic Press, 511pp.
- Jones, R., 15 November 1993: "One dies as boats collide on stormy sea," final ed., *The Monterey County Herald*, pp 1A, 10A.
- Keyser, D., and M. A. Shapiro, 1986: A review of the structure and dynamics of upper-level frontal zones. *Mon. Wea. Rev.*, **114**, 452-499.

- Liou, C. -S., R. M. Hodur, and R. H. Langland, 1994: Navy Operational Regional Atmospheric Prediction System (NORAPS): A triple nest mesoscale model. Preprints, *10th Conf. On Numerical Weather Prediction*, Portland, OR, Amer. Meteor. Soc., 423-435.
- List, R. J., ed., 1951: *Smithsonian Meteorological Tables*. Smithsonian Institution, 527 pp.
- Martin, J. E., J. D. Locatelli and P. V. Hobbs, 1992: Organization and structure of clouds and precipitation on the Mid-Atlantic coast of the United States. Part V: The role of an upper-level front in the generation of a rainband. *J. Atmos. Sci.*, **49**, 1293-1303.
- Mass, C. F., W. J. Steenburgh and D. M. Schultz, 1991: Diurnal surface-pressure variations over the continental United States and the influence of sea level reduction. *Mon. Wea. Rev.*, **119**, 2814-2830.
- Pielke, R. A., and J. M. Cram, 1987: An alternate procedure for analyzing surface geostrophic winds and pressure over elevated terrain. *Wea. Forecasting*, **2**, 229-236.
- Pauley, P. M., N. L. Baker and E. H. Barker, 1996: An observational study of the "Interstate 5" dust storm case. *Bull. Amer. Meteor. Soc.*, **77**, 693-720.
- Reed, R. J., and F. Sanders, 1953: An investigation of the development of a mid-tropospheric frontal zone and its associated vorticity field. *J. Meteor.*, **10**, 338-349.
- , and E. F. Danielsen, 1959: Fronts in the vicinity of the tropopause. *Arch. Meteor. Geophys. Bioklim.*, **A11**, 1-17.
- Sangster, W. E., 1987: An improved technique for computing the horizontal pressure-gradient force at the earth's surface. *Mon. Wea. Rev.*, **115**, 1358-1369.
- Saucier, W. J., 1955: *Principles of Meteorological Analysis*. The University of Chicago Press, 438 pp.
- Shapiro, M. A., 1976: The role of turbulent heat flux in the generation of potential vorticity in the vicinity of upper-level jet stream systems. *Mon. Wea. Rev.*, **104**, 892-906.
- STORM DATA, 1993: Storm data and unusual weather phenomena. National Climatic Data Center, Asheville, NC, Storm Data, **35**, No. 11, 63 pp.
- Stull, R. B., 1988: *An Introduction to Boundary Layer Meteorology*. Kluwer Academic Publishers, 666 pp.
- , 1973: Inversion rise model based on penetrative convection. *J. Atmos. Sci.*, **30**, 1092-1099.

- Spaete, P., D. R. Johnson, and T. K. Schaak, 1994: Stratospheric-tropospheric mass exchange during the President's Day Storm. *Mon. Wea. Rev.*, **122**, 424-439.
- Uccellini, L. W., D. Keyser, K. F. Brill and C. H. Wash, 1985: The Presidents' Day cyclone of 18-19 February 1979: Influence of upstream trough amplification and associated tropopause folding on rapid cyclogenesis. *Mon. Wea. Rev.*, **113**, 962-988.
- , R. A. Petersen, K. F. Brill, P. J. Kocin and J. J. Tuccillo, 1987: Synergistic interactions between an upper-level jet streak and diabatic processes that influence the development of a low-level jet and a secondary coastal cyclone. *Mon. Wea. Rev.*, **115**, 2227-2261.
- U. S. Weather Bureau, 1963: *Manual of Barometry*, Department of Commerce, Vol 1.
- Wallace, J. M., and P. V. Hobbs, 1977: *Atmospheric Science*, Academic Press, 467 pp.
- Weaver, J. F., and J. J. Toth, 1990: The use of satellite imagery and surface pressure-gradient analysis modified for sloping terrain to analyze the mesoscale events preceding the severe hailstorms of 2 August 1986. *Wea. Forecasting*, **5**, 279-298.
- World Meteorological Organization, 1986: Atmospheric ozone 1985: Global ozone research and monitoring report. Rep. 16, WMO, 392 pp.

INITIAL DISTRIBUTION LIST

	No. Copies
1. Defense Technical Information Center 8725 John J. Kingman Rd., STE 0944 Ft. Belvoir, VA 22060-6218	2
2. Dudley Knox Library Naval Postgraduate School 411 Dyer Rd. Monterey, CA 93943-5101	2
3. Chairman, Code MR Meteorology Department Naval Postgraduate School Monterey, CA 93943	1
4. Prof. P. M. Pauley, Code MR/Pa Meteorology Department Naval Postgraduate School Monterey, CA 93943	4
5. Prof. Q. Wang, Code MR/Qg Meteorology Department Naval Postgraduate School Monterey, CA 93943	2
6. LT Sara T. Burke 233 Marsh Island Drive Chesapeake, VA 23320	2
7. Mr. Edward H. Barker 7 Grace Hopper Avenue Monterey, CA 93943	1
8. Mr. William M. Clune Fleet Numerical Meteorology and Oceanography Center 7 Grace Hopper Avenue Monterey, CA 93943	1

JUDLEY KNOX LIBRARY
NAVAL POSTGRADUATE SCHOOL
MONTEREY CA 93943-5101

DUDLEY KNOX LIBRARY



3 2768 00338505 5